SPECTRAL BANDWIDTH EXTENSION:

INVENTION VERSUS HARMONIC EXTRAPOLATION

A Thesis

Presented to

the Faculty of the Department of Earth and Atmospheric Sciences

University of Houston

In Partial Fulfillment

of the Requirements for the Degree

Master of Science

By

Chen Liang

May 2014

SPECTRAL BANDWIDTH EXTENSION:

INVENTION VERSUS HARMONIC EXTRAPOLATION

_____

Chen Liang

APPROVED:

_____

Dr. John P. Castagna, Supervisor
Department of Earth and Atmospheric Sciences

_____

Dr. Evgeny Chesnokov, Committee member
Department of Earth and Atmospheric Sciences

_____

Dr. Fred J. Hilterman, Committee member
Department of Earth and Atmospheric Sciences

_____

Dr. Daniel Ebrom, Committee member
Statoil Corporation

_____

Dean, College of Natural Sciences and Mathematics

ACKNOWLEDGEMENTS

First and foremost, I would like to thank my thesis advisor, Dr. John P. Castagna for his consistent advice and careful guidance throughout my M.S. study and research.
I could never have this thesis completed without his encouragement and positive comments. I also would like to express my gratitude to the rest of my committee members, Dr. Evgeny Chesnokov, Dr. Fred J. Hilterman, and Dr. Daniel Ebrom for their participation and sincere suggestions on my work. Further, I am really grateful to Dr. Robert Stewart for his consent for me to have access to the real datasets at the AGL.

My special thanks should be dedicated to my dear friends who always support and inspire me when I have troubles and difficulties in life. Last but not the least; I give the best regards to my dearest parents who are standing by my side all the time.

SPECTRAL BANDWIDTH EXTENSION:

INVENTION VERSUS HARMONIC EXTRAPOLATION

An Abstract of a Thesis

Presented to

the Faculty of the Department of Earth and Atmospheric Sciences

University of Houston

In Partial Fulfillment

of the Requirements for the Degree

Master of Science

By

Chen Liang

May 2014

ABSTRACT

There are valid and invalid post-processing methods to extend seismic bandwidth for resolution enhancement. Some methods attempt to invent high frequencies without a physical basis, while inversion-based methods extrapolate the spectra in reasonable ways. Frequency invention methods can extend the original seismic spectrum to desired spectral bandwidths. However, those spectral components they invent do not provide new effective information for enhancing resolution. Matching pursuit decomposition has been successfully applied to analyze the available spectrum of seismic data. Consequently, missing spectral components can be directly extrapolated from zero frequency all the way to the Nyquist frequency. Alternatively, the spectral information within the limited band can be modeled as an autoregressive process. Higher and lower frequencies outside the band can thus be predicted by designing a Wiener prediction filter. Spectral decomposition by matching pursuit on the band-limited seismic trace stabilizes the predictions to recover a broad-band reflectivity sequence. Further, continuous wavelet transform can be employed to spectrally decompose the band-limited signal into discrete sub-bands from which missing high and low frequencies could be extrapolated locally using multi-channel operators. Conventional sparse spike deconvolution attempts to retrieve a reflectivity sequence comprising isolated sparse delta functions, which may restore the missing part of the spectrum.

TABLE OF CONTENTS

LIST OF FIGURES

Chapter 1

Introduction

Due to over exploitation of natural oil and gas resources in recent decades, exploration targets have increasingly changed from large structural reservoirs to subtle entities which might not yet be detected. New techniques are thus in demand for seismic volumes of higher resolution with more details. Resolution is the ability to separate two features that are close together. In 3D seismic data, seismic resolution involves both vertical (temporal) and horizontal (spatial) resolution. In this thesis, we investigate various methodologies to vertically enhance the data resolution. The seismic temporal resolution, being a function of frequency content, is determined by effective spectral bandwidth, which is exactly what is studied here.

In seismic exploration, the geological subsurface is generally assumed to be parallel layers with varying rock properties. Impedance contrast between adjacent layers could generate reflections at the interfaces if seismic energy strikes. Ideally, energy waves propagating through subsurface layers and hitting the interfaces will, if there is no energy loss or frequency attenuation, produce impulse responses from the earth. The impulse response can be thought as a broad-band reflectivity series. However, in nature there are absolutely no rocks with perfect quality. The seismic energy will partly be converted into heat while passing through the medium, which will result in amplitude reduction and frequency loss. Therefore, seismograms recorded at surface are typically band-limited with high and low frequencies missing. A basic goal for

seismic interpretation is just to derive reflectivity sequences representing the true subsurface structures from observed seismic data so as to provide better interpretations consistent with the actual geology.

For seismic acquisition and processing stages, many efforts have been made to preserve and restore signal bandwidth. They do work well, but in many cases they do not achieve broad enough bandwidth for interpretation purpose. So my research is focused on the post-processing stage, which is more likely to be worth the effort. A tremendous amount of work has been done for higher resolution results on post-processing sections. Oldenburg et al. (1983) described the basic theory of linear programming method for reflectivity inversion, and also indicated that the spectrum of the structure for a layered earth can be modeled as an autoregressive (AR) process. Russell (1985) outlined various deconvolution methods in theory and also made them easily applied in the real world. Sacchi (1997) examined different regularization criteria leading to an algorithm where the damping term is adapted to retrieve a broad-band reflectivity sequence. Further, spectral inversion yields accurate thickness determinations below tuning, using the inverse relationship between thickness and the constant periodicity of spectral interference patterns (Puryear and Castagna 2008). Extension of bandwidth using harmonics and sub-harmonics predicted and computed with CWT will enhance the seismic resolution, allowing a more refined and detailed interpretation (Smith et al. 2008). Zhang and Castagna (2011) used a wedge dictionary for seismic responses of any thickness to derive an inversion with significantly greater vertical resolution by basis pursuit algorithm. The purpose of this paper is just to evaluate and compare various spectral extension methods based on

summary and analysis for the previous achievements.

The convolutional model is widely employed in seismic processing and interpretation which indicates that a post-processing seismogram $s(t)$ can be represented by convolution of an embedded wavelet $w(t)$ with a reflectivity series $r(t)$ plus random noise $n(t)$. Reflections are thus assumed to be generated at normal incidence. This process is shown in Figure 1.1. In this thesis, I also assume the wavelet is constant with time and space; hence, the convolution model is represented as:

$$s(t) = w(t) * r(t) + n(t) \tag{1.1}$$

Mathematically, the convolutional operation is essentially an integral process:

$$s(t) = \int w(\tau)\, r(t-\tau) d\tau + n(t) \tag{1.2}$$

which implies that the convolution formula can be described as a weighted average of the wavelet function $w(\tau)$ at the moment t, where the weighting is given by the reflectivity $r(-\tau)$ simply shifted by amount t. Further according to the convolution theorem, Fourier transform of the convolution between two functions is the product of the transforms for those two functions. Consequently, seismic bandwidth should be limited within the wavelet band (Figure 1.2) given that high and low frequencies in the recorded seismograms have to be filtered out due to earth filtering effect.

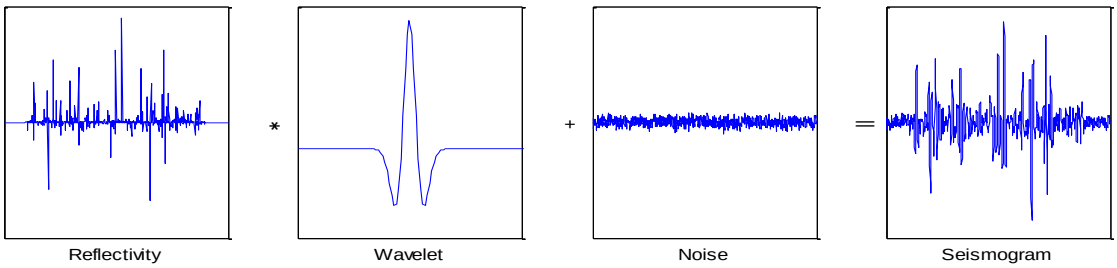

Figure 1.1: Convolutional model in time domain.

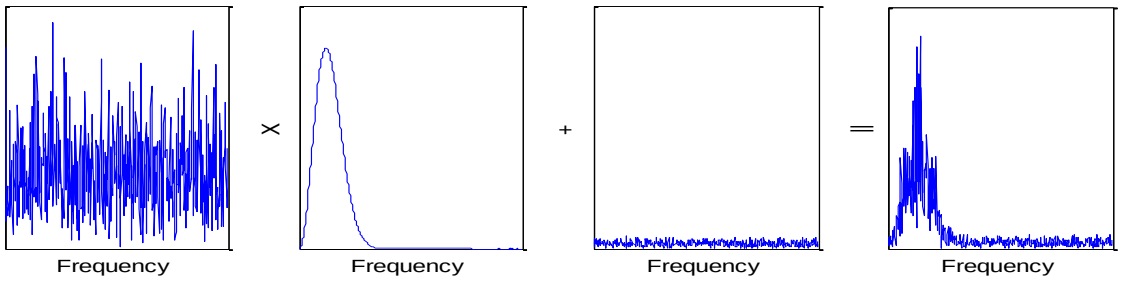

Figure 1.2: Convolutional model in frequency domain.

There are many different methods to extend seismic spectral bandwidth. Some invent higher frequencies, making the spectrum apparently extended. However, these frequency invention methods are performed without a physical base, thus whether they can actually increase resolution should be questioned. On the other hand, based on the convolutional model, the fact that there is actually a strong relationship between the frequencies inside and outside the limited band provides opportunities that the missing spectral components can be recovered in logical and verifiable ways.

In this thesis, Chapter 2 first introduces three frequency invention methods for extending spectral bandwidth: frequency-modulating method, frequency-sliding method, and frequency-doubling method. Spectrally broadened seismic traces generated by these three methods are compared with new higher frequency synthetics with comparable bandwidths. Whether they are valid or not will be demonstrated by wedge model tests. In Chapter 3, matching pursuit decomposition (MPD) is applied to analyze the available data band using sine waves as the bases. Chakraborty and Okaya (1995) refer to matching pursuit algorithm in time domain discussed by Mallat and Zhang (1993). An improved version of MPD, fractional matching pursuit decomposition (FMPD), is proposed by Chen and Castagna (2012), which is supposed to solve an instability problem due to bases nonorthogonality. The Wiener filter is the

keystone of many current seismic digital processing systems, and Treitel (1970) generalizes the multichannel Wiener theory as a natural extension of the more familiar single-channel case. Therefore, Chapter 4 presents the idea that the attenuated frequency components could be calculated and predicted from the available spectrum in a least-squares error sense. This is performed on both matching pursuit (MP) and continuous wavelet transform (CWT) frequency gathers. In Chapter 5, we discuss the conventional sparse spike deconvolution approach. Sparse spike inversion has been widely used in industry for many years. It gives solutions for the earth model as simple as possible, while an acceptable data misfit is honored. Chen and Donoho (2001) derive the sparse spike algorithm by linear programming. For this section, we prefer a reweighted strategy which iteratively retrieves the broad-band reflectivity sequence. To sum up, Chapter 3, Chapter 4, and Chapter 5 demonstrate those theoretically valid methods from totally different perspectives. Their effectiveness will be illustrated by using synthetic cases as well as real data examples. Furthermore, comparisons for all methods are presented, and a final discussion is given in Chapter 6.

A 3C-3D seismic survey was acquired in 1995, proposed by Boyd Exploration Consultants Ltd and the CREWES Project. The survey was over the Blackfoot field near Strathmore Alberta (Township 23, Range 23 W4M), as determined by suggestions from industry. This Blackfoot 3C-3D survey was recorded in two overlapping patches (Figure 1.3). One was designed to target the clastic Glauconitic channel and the other one was for a deeper, reef-prone Beaverhill Lake carbonate prospect. Recorded logs for 12 wells in the Glauconite patch are available with this

real dataset. However, only the 01-08-23-23 well has been selected to do the inversions for this paper. All algorithms require information about the seismic wavelet to perform the spectral extension.

The wavelet which is assumed to be zero-phase (Figure 1.5) is extracted statistically with the seismic traces from Cross-line 88 to 168 at Inline 49. The picked time window ranges from 800ms to 1200ms. A relatively good synthetic tie (Figure 1.4) is achieved between the well log-derived seismic trace and the averaged trace around that well where the maximum correlation coefficient is large than 0.8. The corresponding surface seismic line, which is a migrated 2D section, will be ready for testing all those spectral extension algorithms.

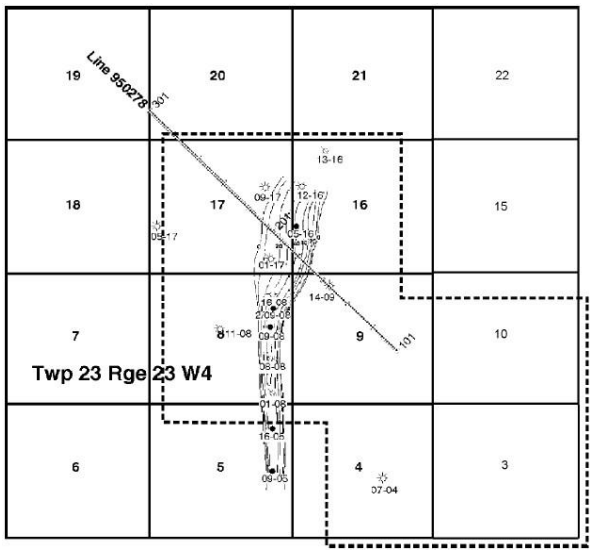

Figure 1.3: Base map of Blackfoot field. The survey area is shown within the dash line.

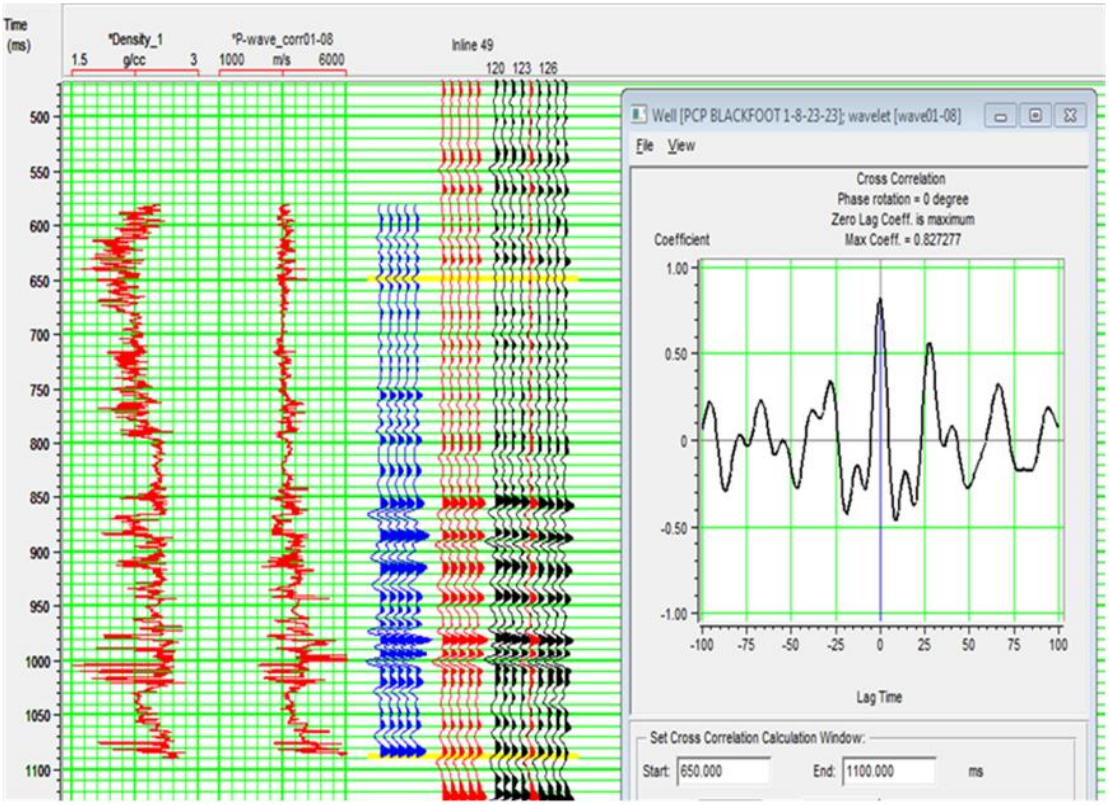

Figure 1.4: Well log data, including density and sonic logs along with synthetic seismogram (blue), composite trace at the well (red) and seismic traces surrounding the well (black). The maximum correlation coefficient is 0.83.

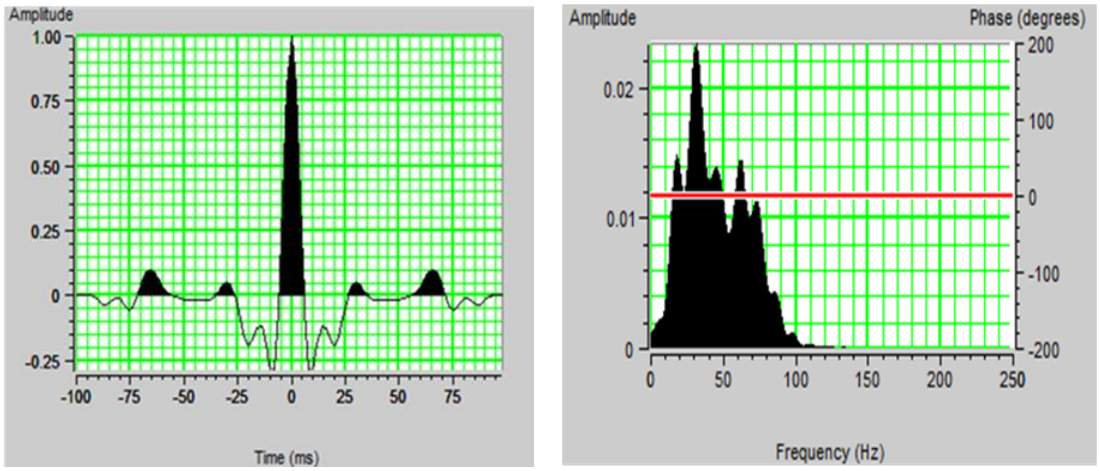

Figure 1.5: Statistically extracted wavelet in time domain (left) and its amplitude spectrum (right). The peak frequency is around 30Hz and the wavelet is zero-phase.

Chapter 2

Spectral Extension by Frequency Invention Methods

Fourier transform (FT), named after French scientist Joseph Fourier, describes a kind of mathematical transform utilized to transform signals between time or spatial domain and frequency domain which can be operated reversibly. The Fourier transform and its mathematically derived variants have many applications in physics and engineering. Its mathematical properties can be used to manipulate spectral information in frequency domain whereby the signal bandwidth could be extended. However, apparently broader bandwidth does not necessarily mean better resolution for the signal in time domain. In this chapter, frequency invention methods of extending seismic spectral bandwidth without physical bases are investigated.

2.1 Frequency-sliding Method

To start with, band-limited seismic spectrum will be easily extended where the higher frequencies are invented by directly rescaling the original spectrum. Visually, the data spectrum will be slid along the frequency axis. Intuitively, signal resolution should be better if low frequency components are replaced by higher frequencies. However, this is a common mistake which all beginners might commit. To clarify this issue, three diverse waveforms of varying spectral bands in time domain are displayed in Figure 2.1.

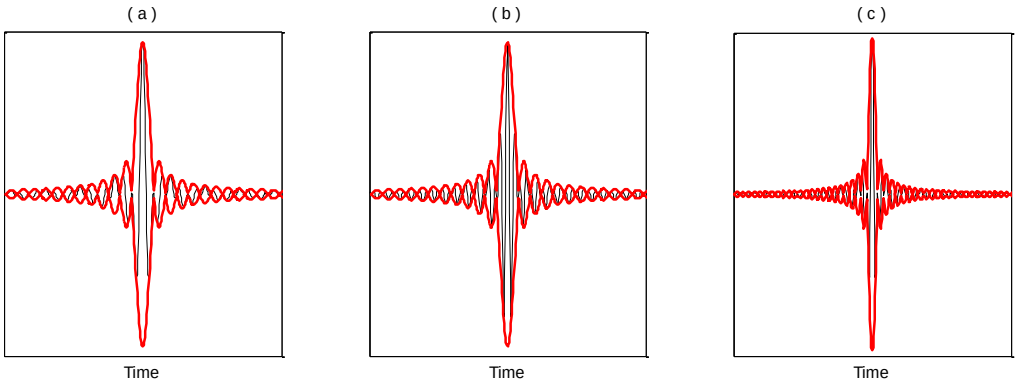

Figure 2.1: (a) Band-pass filter of 10-40Hz; (b) Band-pass filter of 30-60Hz; (c) Band-pass filter of 20-80Hz.

The waveform with a spectral band of 10-40Hz (Figure 2.1a) has a bandwidth of 30Hz, and another waveform with a band of 30-60Hz (Figure 2.1b) also has the same bandwidth but with a higher central frequency. Obviously, the waveform in Figure 2.1b oscillates with a higher rate than that in Figure 2.1a. However, their envelopes are exactly the same because of the identical bandwidths in frequency domain. Therefore, the envelopes would stay the same if the bandwidths are the same and just slid. A third waveform with a band of 20-80Hz is shown in Figure 2.1c whose bandwidth of 60Hz is broader than the previous two. As a result, the corresponding envelope becomes much narrower, which implies its resolution should be better. Consequently, seismic data resolution is determined by the absolute bandwidth rather than the central frequency. So the idea for this method is just to slide original seismic spectrum to any desired frequency and add those duplicated spectra back to the original one in order to obtain a spectrally broadened seismic trace.

A synthetic trace generated by a 25Hz Ricker wavelet is given in Figure 2.2a, thus the dominate frequency is around 25Hz (Figure 2.3a). Then the original spectrum is rescaled to higher frequencies by a shift interval of 30Hz (Figure 2.3b and Figure

2.3c). Their corresponding traces (Figure 2.2b and Figure 2.2c) in time domain have the identical envelopes as expected.

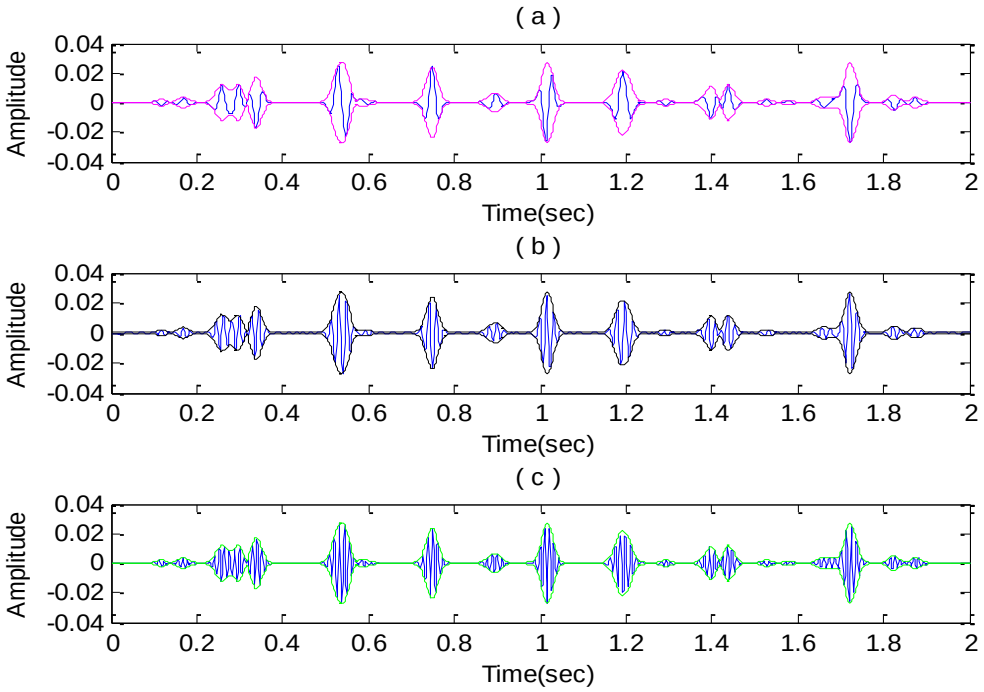

Figure 2.2: (a) Original synthetic trace (25Hz); (b) Frequency-sliding trace (55Hz); (c) Frequency-sliding trace (85Hz).

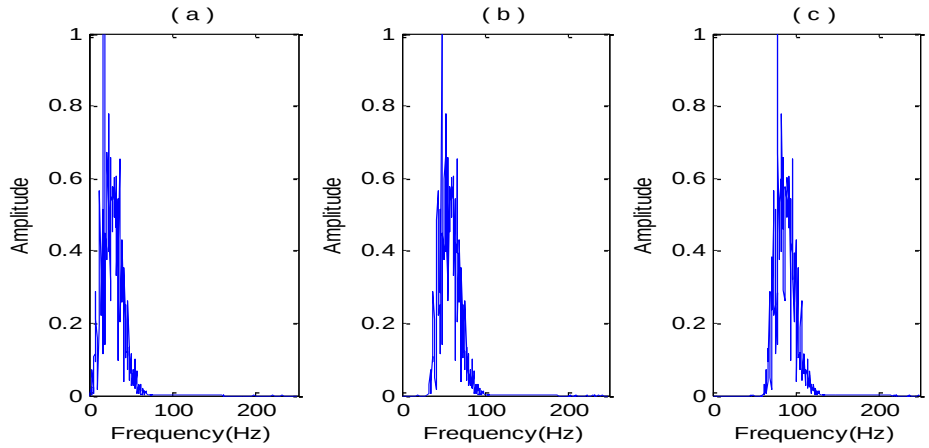

Figure 2.3: (a) Spectrum of the original trace (25Hz); (b) Spectrum of the Frequency-sliding trace (55Hz); (c) Spectrum of the Frequency-sliding trace (85Hz).

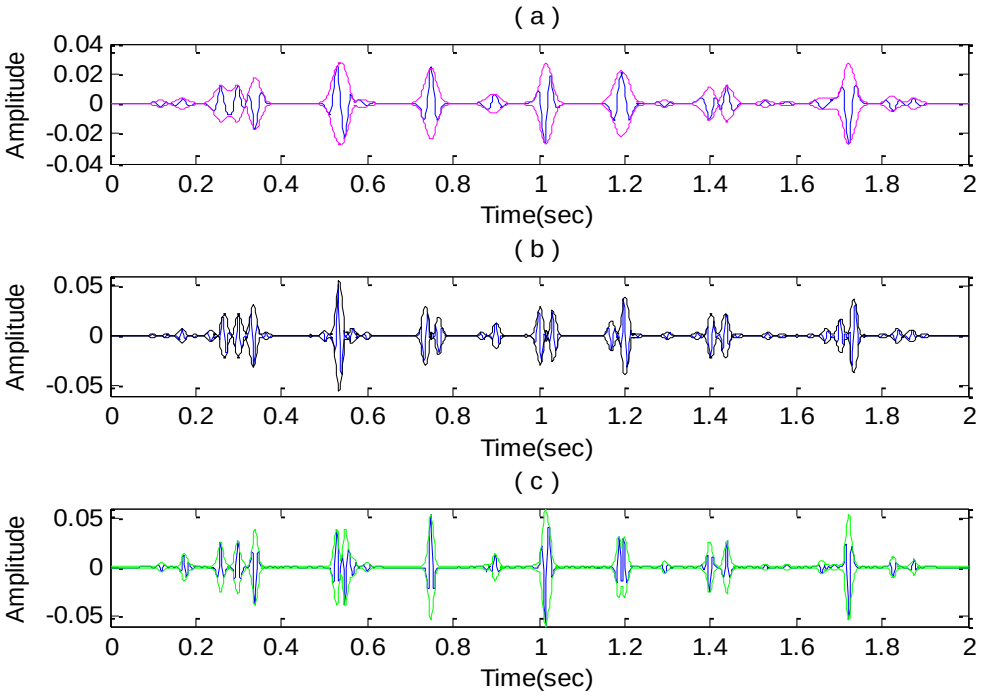

Figure 2.4: Frequency-sliding method. (a) Original synthetic trace (25Hz) with its envelope; (b) Spectrally broadened trace with its envelope; (c) High frequency synthetic trace (55Hz) with its envelope.

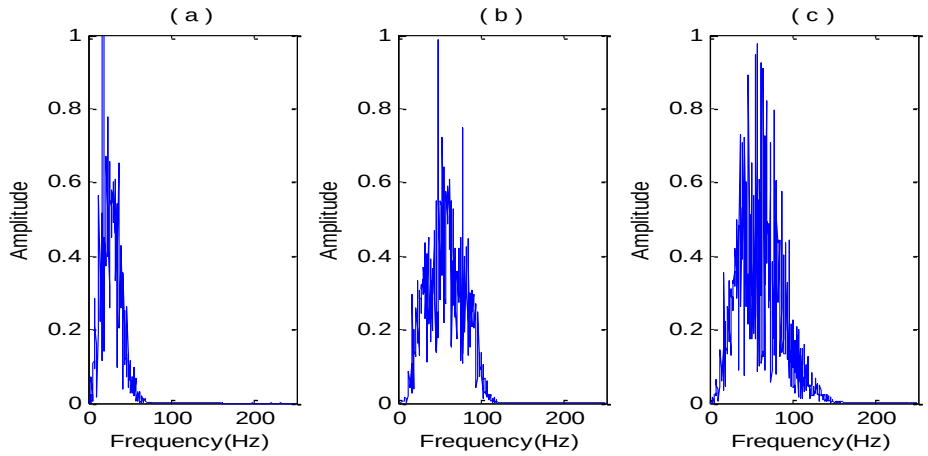

Figure 2.5: Frequency-sliding method. (a) Spectrum of the original synthetic (25Hz); (b) Spectrum of the spectrally broadened synthetic; (c) Spectrum of the high frequency synthetic (55Hz).

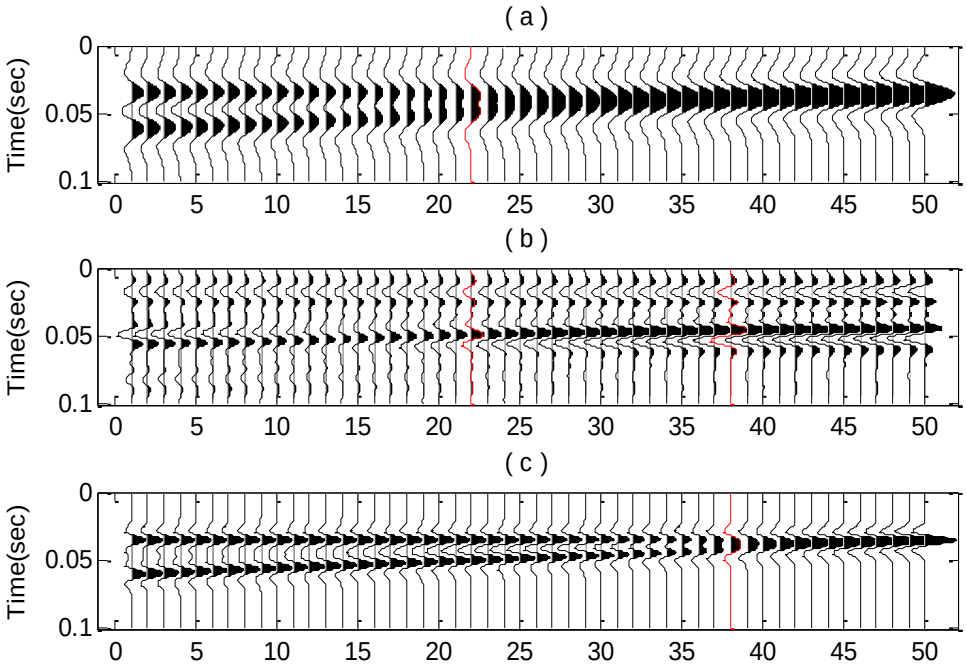

Figure 2.6: Frequency-sliding method. (a) Seismic responses for the wedge model (25Hz); (b) Spectrally extended seismic responses for the wedge model; (c) Seismic responses for the wedge model (55Hz).

Then the three frequency sliding traces are summed to produce a spectrally broadened trace (Figure 2.4b) which has a higher central frequency (Figure 2.5b). For comparison, a new synthetic trace (Figure 2.4c) is also generated by a higher frequency Ricker wavelet with a comparable bandwidth to that spectrally broadened trace. With the spectra (Figure 2.5b and Figure 2.5c) of similar bandwidths, we might expect that they also should have about the same resolution according to previous discussions. However, envelopes on the spectrally broadened trace are not even close to those on the new synthetic trace. Although some envelopes are seemingly narrowed, most of them are distorted and biased instead. The two closely spaced events around 1.2s that can be resolved in the higher frequency synthetic could not be separated in the spectrally broadened trace. Therefore, the ability for this method in enhancing

resolution should be considered doubtful. To further demonstrate the invalidity of this frequency-sliding method, a wedge model comprising even spike pairs is employed. Low frequency seismic responses (Figure 2.6a) are generated by convolving a 25Hz Ricker wavelet. In this case the thin beds can be resolved at Trace 22. Applying this spectral extension method on this seismic section, spectrally extended seismic responses are obtained (Figure 2.6b). And higher frequency wedge model responses are also plotted with the same band-pass for comparison (Figure 2.6c) in which the spike pairs are resolved down to Trace 38. Unfortunately, we could not observe any resolution enhancement indication in the spectrally extended section. The original events in the wedge model are even destroyed that those reflection horizons could no longer be recognized. Conclusively, the frequency-sliding method is invalid because those extended spectra are just sliding in a relatively random fashion which makes it impossible for the spectral components to form periodical ties.

2.2 Frequency-modulating Method

If any function $f(t)$ has the Fourier transform $F(f)$, then $f(t)\cos 2\pi f_0 t$ will have the Fourier transform $\frac{1}{2}F(f-f_0)+\frac{1}{2}F(f+f_0)$. The derivation is given below:

$$\begin{aligned}\int_{-\infty}^{\infty} f(t)\cos 2\pi f_0 t\cdot e^{-i2\pi ft}dt &= \int_{-\infty}^{\infty} f(t)\left[\frac{1}{2}\left(e^{i2\pi f_0 t}+e^{-i2\pi f_0 t}\right)\right]\cdot e^{-i2\pi ft}dt \\ &= \frac{1}{2}\int_{-\infty}^{\infty} f(t)\cdot e^{-i2\pi(f-f_0)t}dt+\frac{1}{2}\int_{-\infty}^{\infty} f(t)\cdot e^{-i2\pi(f+f_0)t}dt \quad (2.1)\\ &= \frac{1}{2}F(f-f_0)+\frac{1}{2}F(f+f_0)\end{aligned}$$

Observed from Eq. 2.1, when a function is multiplied by a sinusoid, the original spectrum of this function will be shifted to the frequency of that sinusoid. Consider a

simple case of multiplying a 25Hz Ricker wavelet by a 75Hz sine wave where their spectra can be analytically computed. The spectrum of the wavelet (Figure 2.7a) is two-sided, with positive and negative frequencies centered at the zero frequency at which there is a notch. The resulting spectrum (Figure 2.7c) shows that the notch in the original spectrum has been shifted to both 75Hz and -75Hz. Consequently, Fourier transform of the multiplied wavelet in this case could be considered as the convolution of the wavelet spectrum with the spectrum (Figure 2.7b) of that sinusoid.

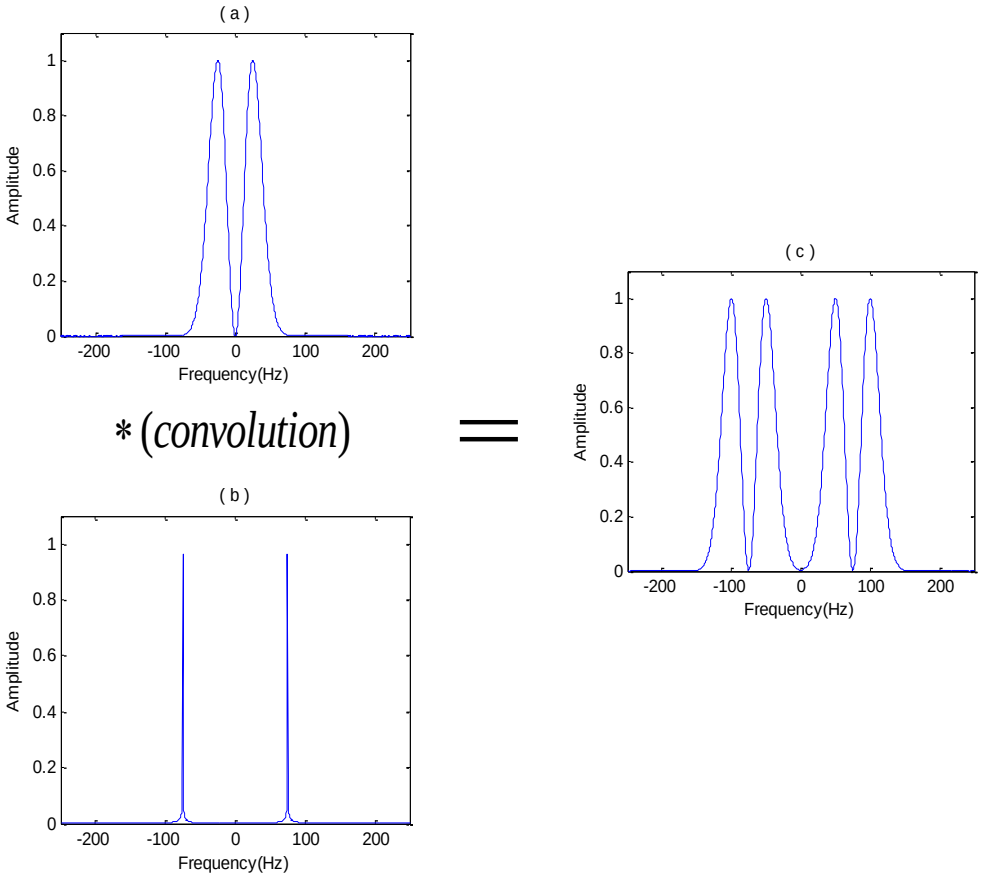

Figure 2.7: (a) Spectrum of 25Hz Ricker wavelet; (b) Spectrum of 75Hz sinusoid; (c) Spectrum of the signal generated by multiplying the wavelet by the sinusoid.

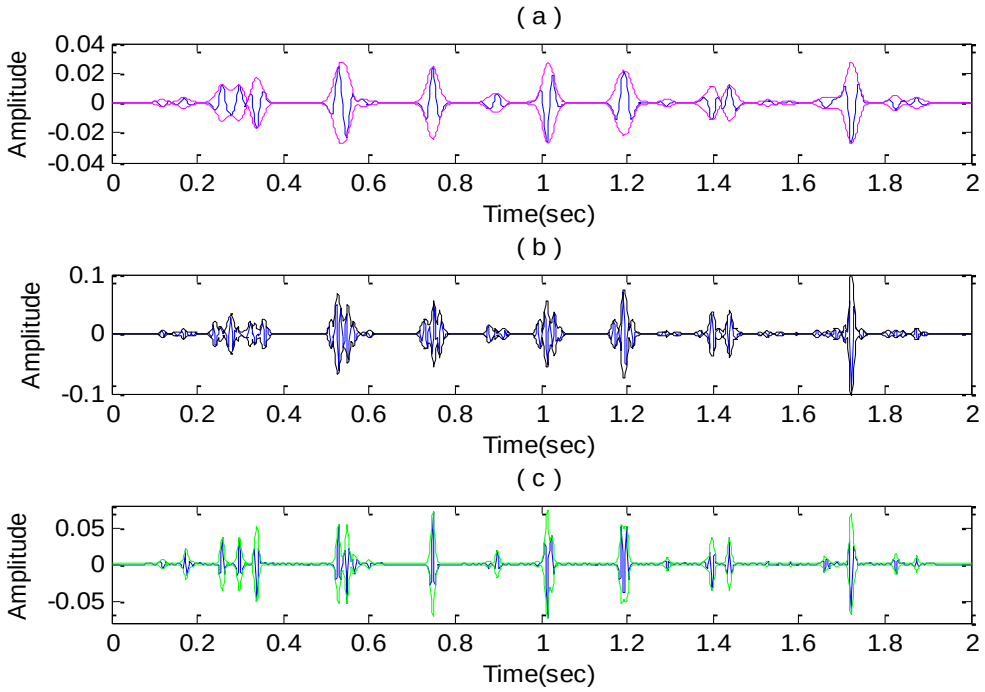

Figure 2.8: Frequency-modulating method. (a) Original synthetic trace (25Hz) with its envelope; (b) Spectrally broadened trace with its envelope; (c) High frequency synthetic trace (75Hz) with its envelope.

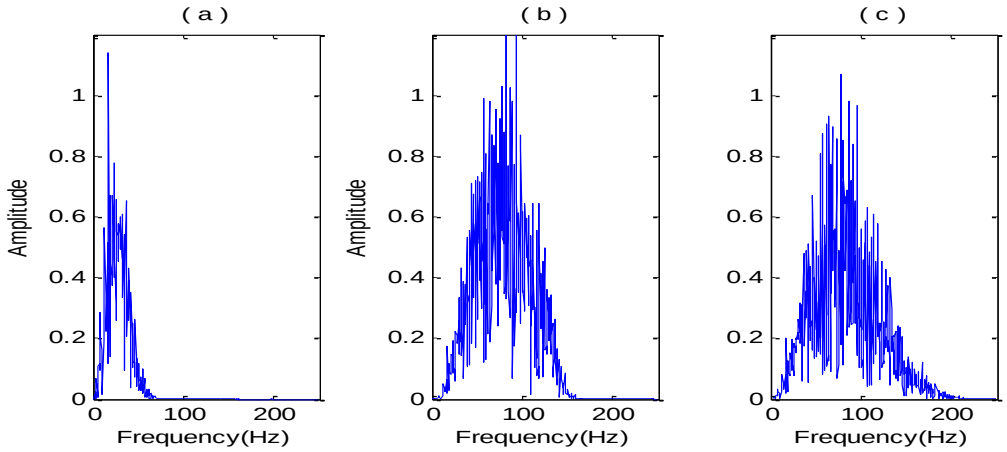

Figure 2.9: Frequency-modulating method. (a) Spectrum of the original synthetic (25Hz); (b) Spectrum of the spectrally broadened synthetic; (c) Spectrum of the high frequency synthetic (75Hz).

In this way, the original spectrum of the seismic trace can be shifted to any desired frequency by multiplying corresponding sinusoids. Consequently, seismic spectral bandwidth could be broadened significantly by adding those frequency-modulating traces back to the original one. Figure 2.8a is the original synthetic trace generated by a 25Hz Ricker wavelet. Its spectrum thus becomes band-limited and the dominant frequency is around 25Hz (Figure 2.9a). After the frequency-modulating method is implemented, the spectrally broadened trace has been produced (Figure 2.8b). Obviously the spectrum (Figure 2.9b) has been extended significantly. Similarly, the new synthetic trace (Figure 2.8c) with a higher frequency wavelet is presented for comparison. Its spectrum (Figure 2.9c) has a similar bandwidth to the spectrally extended one. Seemingly, they also should have comparable resolution. However, the spike pair around 1.2s resolved by the high frequency wavelet still cannot be separated in the spectrally broadened trace. The waveforms and event locations are once again distorted and biased. Polarities of some reflections are even reversed such as the events near 1.4s. Observed from the corresponding envelopes for each trace, for some isolated events, their envelopes are truly narrowed but compressing a single wavelet simply amounts to changing the wavelet. It only refers to interfering events that resolution is relevant. Envelopes for those interfering events on the spectrally broadened trace do not indicate the resolution has been enhanced. They just have become disordered with this spectral extension method.

Similarly, the validity of this method can be further disproved by the wedge model test (Figure 2.10). The time seismic responses generated by a higher frequency Ricker wavelet of 75Hz for the wedge model are shown in Figure 2.10c.

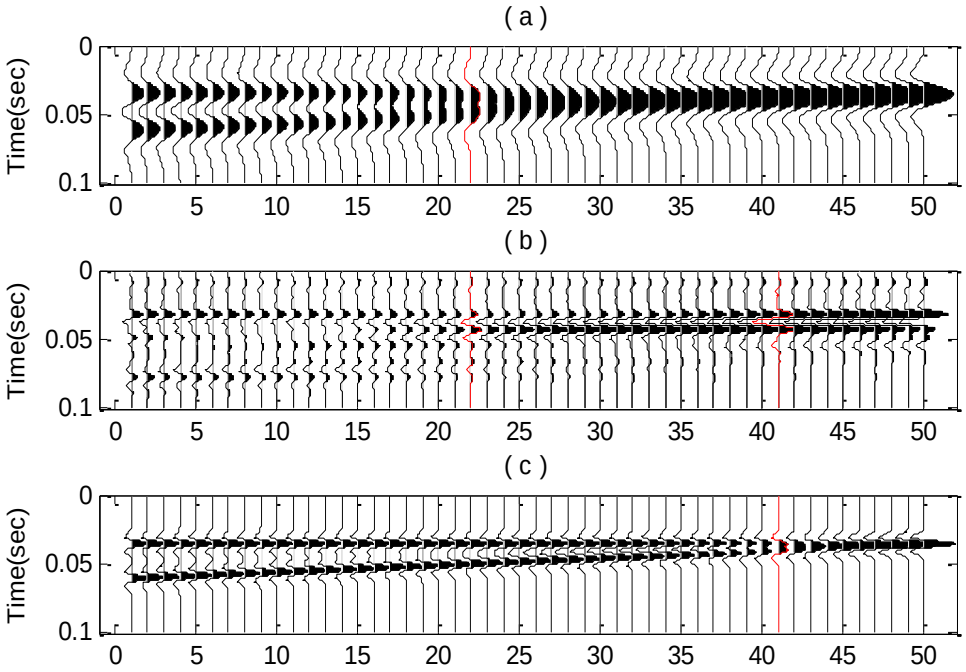

Figure 2.10: Frequency-modulating method. (a) Seismic responses for the wedge model (25Hz); (b) Spectrally extended seismic responses for the wedge model; (c) Seismic responses for the wedge model (75Hz).

In this case, those thin layers can be resolved down to Trace 41, which is much thinner than that in the original section. However, for the spectrally extended wedge model responses (Figure 2.10b), no resolution improvement is achieved. Worse still, the true locations of those spike pairs in the original wedge model are lost in the spectrally extended section. Consequently, the bandwidth is not really broadened by this frequency-modulating method. The extended spectrum is just smeared from the original band by the windowing effect with sine waves being the ugly windows. It really makes sense that an event can never be resolution enhanced if it is just truncated by a window whereby the bandwidth is broadened. Therefore, those resulting high frequency components are not new useful information.

2.3 Frequency-doubling Method

Considering a sinusoid of single frequency (Figure 2.11a) in time domain, its spectrum should be an isolated spike at that frequency (Figure 2.11c). When rectifying all negative values of this sinusoid to be positive (Figure 2.11b), its spectrum will become a series of spikes with a constant interval of doubled frequency at specific components ranging from zero frequency all the way to the Nyquist frequency with a downward trend for the amplitude (Figure 2.11d). After rectifying, the average level of this sinusoid, which is originally oscillated up and down around zeros, has been raised to a positive value, which is the reason why there is a spectral component at the zero frequency.

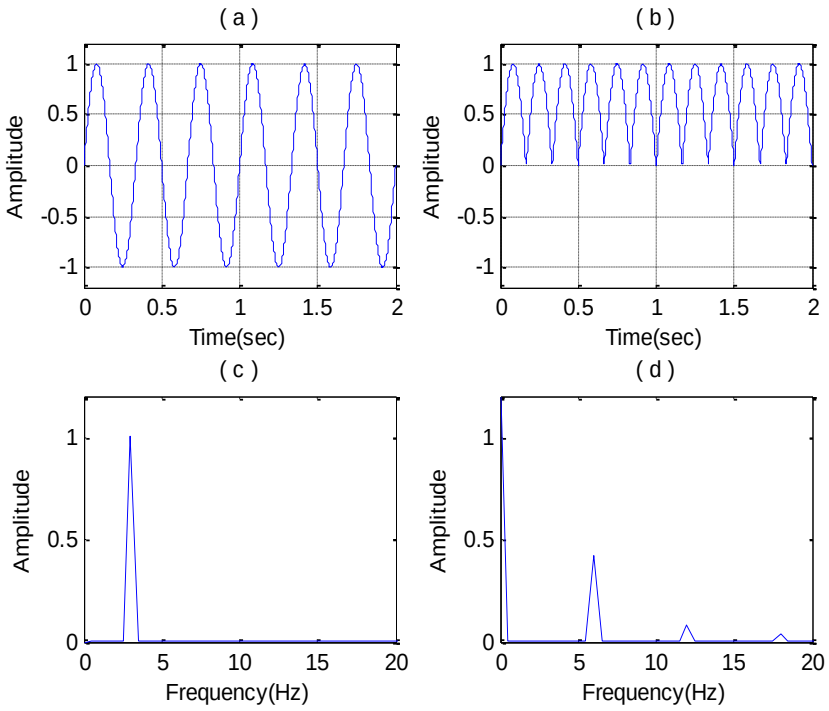

Figure 2.11: (a) 3Hz sinusoid; (b) Rectified 3Hz sinusoid; (c) Spectrum of the 3Hz sinusoid; (d) Spectrum of the rectified 3Hz sinusoid.

Also, troughs in the original sinusoid become all positive at the same time points; the same values thus have turned to repeat twice the frequence of the original signal. Consequently, there is a spectral component at the frequency doubling the original one. Further, smooth curves at zero crossings have become spiky. Those spiky parts in the rectified sinusoid result in those higher frequencies. The above statement is just the case for a single sinusoid. In fact, this would be the same situation for any seismic trace, since according to Fourier theory, any function can be considered as a superposition of a series of sine waves with various frequencies such that each spectral component will be processed the same way as the single sinusoid.

Figure 2.12 shows a zero-phase band-pass filter in both time and frequency domain which will be used to filter out the very low and very high frequencies in the rectified trace. Cutting out the high frequencies makes the sharp troughs smooth, while cutting out the low frequencies restores some envelopes. What are needed are just the spectral components doubling those of the original trace.

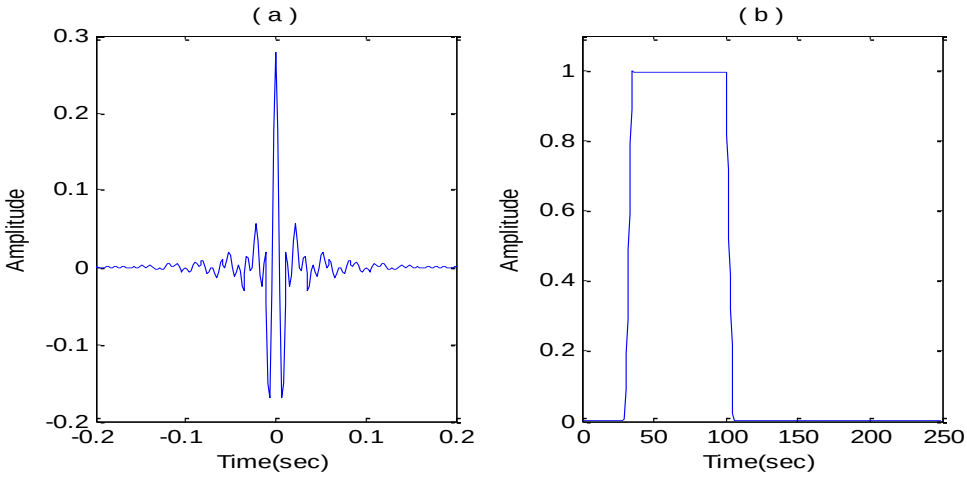

Figure 2.12: (a) A band-pass filter in time domain; (b) Frequency response of the band-pass filter (30Hz-35Hz-100Hz-105Hz).

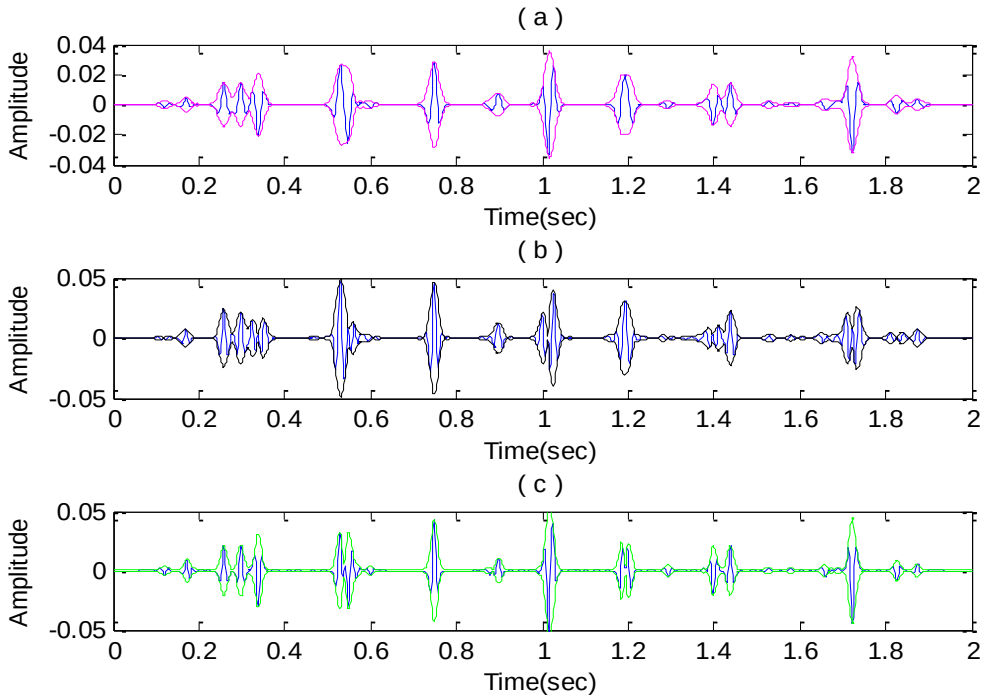

Figure 2.13: Frequency-doubling method. (a) Original synthetic trace (30Hz) with its envelope; (b) Spectrally broadened trace with its envelope; (c) High frequency synthetic trace (45Hz) with its envelope.

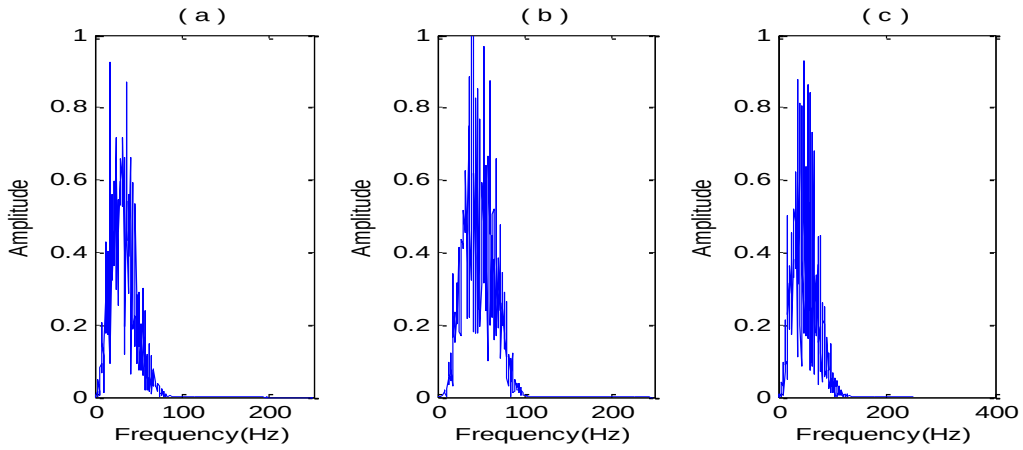

Figure 2.14: Frequency-doubling method. (a) Spectrum of the original synthetic (30Hz); (b) Spectrum of the spectrally broadened synthetic; (c) Spectrum of the high frequency synthetic (45Hz).

The synthetic trace used in this method (Figure 2.13a) is generated by convolving a 30Hz Ricker wavelet. The dominant frequency is thus limited around 30Hz in this case (Figure 2.14a). Rectifying all negative values to be positive, the band-pass filter is employed to reserve the spectral components required to make the spectrally broadened trace. Since the filter is zero-phase, phase information for each frequency component would be invariable, and what is modified will be the amplitude spectrum. Subsequently, adding the filtered trace back to the original trace would result in the frequency-doubling trace (Figure 2.13b). Once again, the reference synthetic (Figure 2.13c) is made by a higher frequency wavelet which, for this method, the central frequency is 45Hz.

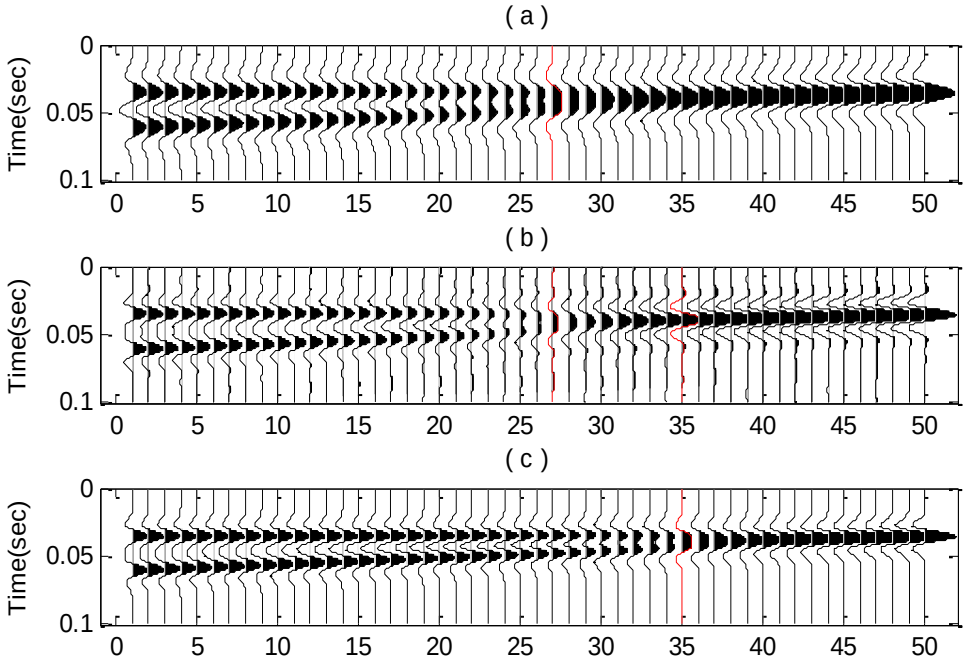

Figure 2.15: Frequency-doubling method. (a) Seismic responses for the wedge model (30Hz); (b) Spectrally extended seismic responses for the wedge model; (c) Seismic responses for the wedge model (45Hz).

Observing the traces which are expected to have similar resolution (Figure 2.13b and Figure 2.13c), the thin layer around 1.2s that can be resolved in the 45Hz synthetic trace, unfortunately still stays as a one single event on the frequency-doubling trace. The corresponding envelope for this reflection has almost no change. In fact, a more serious problem for this so-called frequency-doubling method is that polarities of those negative reflections might be destroyed. Positive reflections added to negative reflections could split one single event into two separated parts, which can be observed at the event around 1.4s (Figure 2.13b). So this method will probably not make the seismic trace look natural, let alone achieve resolution enhancement.

Again, the wedge model has been tested to demonstrate that the frequency-doubling method does not work for enhancing seismic resolution. Thin layers can be resolved at Trace 27 (Figure 2.15a) in the low frequency synthetics (30Hz). For the high frequency synthetics (45Hz), those spike pairs can be separated at Trace 35 (Figure 2.15c). However, we could not observe any indication of enhanced resolution in the spectrally extended section (Figure 2.15b). As a matter of fact, if we continuously rectify the spectrally doubled signals the same way, the resulting spectrum can be further extended to frequencies tripling the original. Based on the previous cases, however, we might foretell that this should be not worth the effort even with apparently much broader bandwidth. Therefore, to make a conclusion, the so-called frequency-doubling method is also invalid. The fact that spectral bandwidth has been broadened should be ascribed to the trace rectification which makes the original signal oscillate more rapidly than before, causing those higher frequencies to come about. However, this is not new effective information for enhancing resolution.

Chapter 3

Frequency Extrapolation by Matching Pursuit Decomposition

3.1 Shift Theorem of Fourier Transform

If the Fourier transform of function $f(t)$ is $F(f)$, then $f(t-t_0)$ has the Fourier transform $e^{-2\pi ft_0}F(f)$. Derivation is presented in Eq.3.1:

$$\begin{aligned}\int_{-\infty}^{\infty} f(t-t_0)e^{-2\pi ft}dt &= \int_{-\infty}^{\infty} f(t-t_0)e^{-i2\pi f(t-t_0)}e^{-i2\pi ft_0}d(t-t_0) \\ &= e^{-i2\pi ft_0}F(f)\end{aligned} \tag{3.1}$$

If there is a time shift for a given function, the amplitude for each spectral component will have no changes. The changes in its Fourier transform are in the phase information. Inferred from Eq.3.1, the phase shift for each frequency should be directly correlated with the frequency f itself: higher frequencies will have more rapid phase changes.

3.2 Convolution Theorem of Fourier Transform

If Fourier transform of function $f(t)$ is $F(f)$ and Fourier transform of function $g(t)$ is $G(f)$, then convolution of the two functions will have the Fourier transform $F(f)G(f)$. The derivation is given in Eq. 3.2:

$$\begin{aligned}\int_{-\infty}^{\infty}\left[\int_{-\infty}^{\infty} f(\tau)g(t-\tau)d\tau\right]e^{-i2\pi ft}dt &= \int_{-\infty}^{\infty} f(\tau)\left[\int_{-\infty}^{\infty} g(t-\tau)e^{-2\pi ft}dt\right]d\tau \\ &= \int_{-\infty}^{\infty} f(\tau)G(f)e^{-i2\pi f\tau}d\tau \\ &= F(f)G(f)\end{aligned} \tag{3.2}$$

Thus, the Fourier transform of convolution between two functions is equivalent to product between transforms of those two functions. Consequently, the resulting amplitude spectrum will be multiplications of amplitudes for all frequency components, while the resulting phase spectrum will be summations of their phases.

3.3 Basic Principles

3.3.1 Discrete Fourier Transform for an Isolated Event

Theoretically, any continuous periodic function can be represented as an infinite Fourier series. However, continuous signals have to be discretized by sampling in practice and length of signal for transform should be limited. Performing Fourier transform on a real signal in time domain, the resulting spectrum will be a complex number of which the modulus is the amplitude spectrum representing energy distribution of each spectral component composing that signal. The inverse tangent function of the imaginary part over the real part in the complex number will give the phase information for each frequency.

Obviously, for a single sinusoid in time domain, the spectral component will be represented by an isolated spike in frequency domain. Since Fourier transform has characteristic of symmetry, it can be expected that an isolated spike in time domain (Figure 3.1a) will correspond to sinusoidal spectra in frequency domain for both its real and imaginary part (Figure 3.1c and Figure 3.1d).

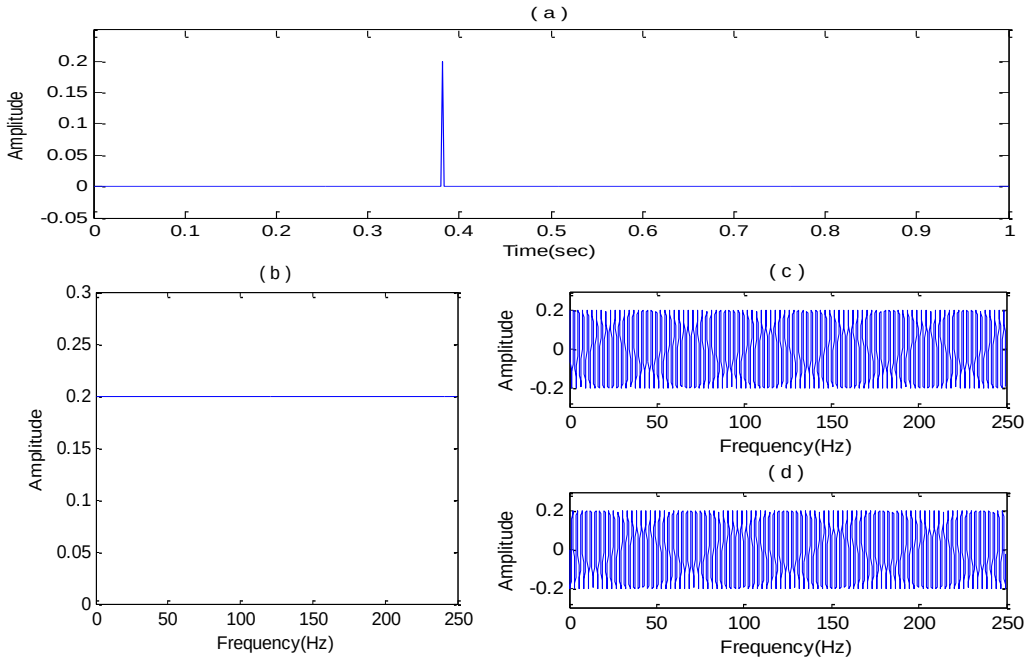

Figure 3.1: (a) An isolated spike in time domain; (b) Amplitude spectrum of the spike; (c) Real part of the spectrum; (d) Imaginary part of the spectrum.

The spectrum of an isolated spike is full band and white; that is, each spectral component has the identical amplitude. According to convolution theorem, if convolving with a band-limited wavelet, the spectrum of the spike will be multiplied by the spectrum of that wavelet, resulting in frequencies outside the band to be absent (Figure 3.2c and Figure 3.2d). The isolated wavelet can be considered as the simplest case for a synthetic seismogram, since there is only one single event on the trace. The wavelet is accurate and no random noise is involved. Although those frequencies outside the wavelet band are missing, there is a strong inherent relationship between the available spectrum inside the band and the missing part outside the band. Mathematically, after dividing the data spectrum by amplitude spectrum of that wavelet, the resulting spectrum within the limited band can actually be connected with the missing part to form a complete sinusoid (Figure 3.3a). Consequently, once

specific information such as frequency period, phase shift, and amplitude of the sine wave over the usable band are known, the missing sinusoid outside the data band will be directly extrapolated.

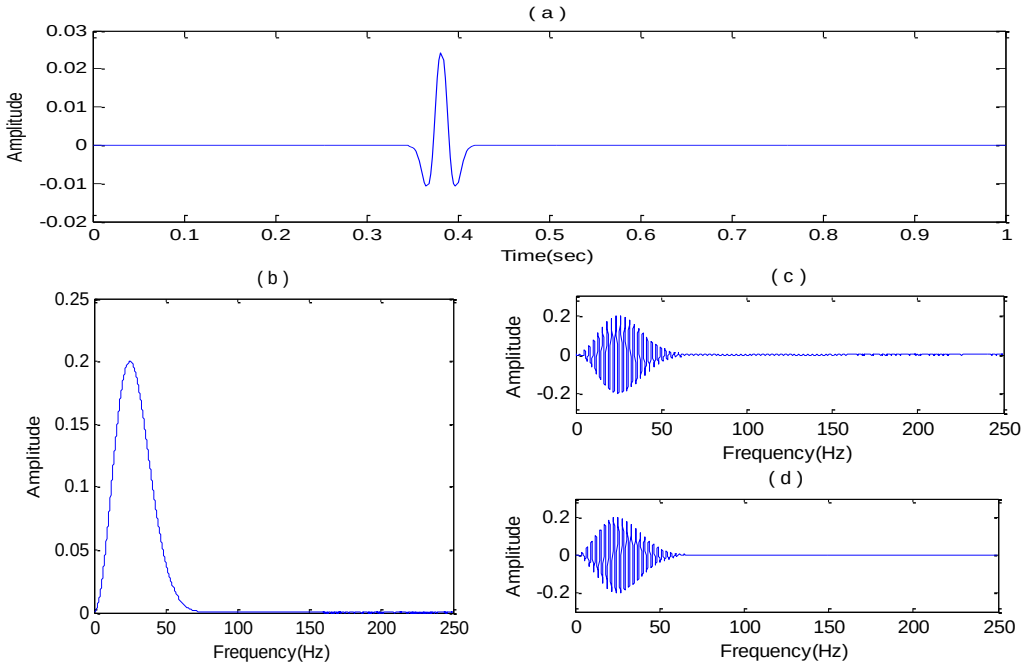

Figure 3.2: (a) An isolated wavelet in time domain; (b) Amplitude spectrum of the wavelet; (c) Real part of the spectrum; (d) Imaginary part of the spectrum.

3.3.2 Spectrum of Composite Events

Seismic traces are typically composed of interfering reflections. However, there are chances to decompose the data into a series of single isolated events at different time points. Correspondingly, spectrum of the composite events should be a superposition of a series of wavelet overprinted sinusoids with various frequency periods, phase shifts, and amplitudes (Figure 3.3b). Furthermore, as the available data bandwidth depends on the band of the wavelet, there would be an unpredictable phase delay for each sinusoid over the usable band. However, once the available composite spectrum becomes decomposed, the original full spectrum could be recovered based on those

parameters for all single events. In fact, there are many ways to achieve this. For the case of this thesis, matching pursuit decomposition (MPD) will be applied to analyze the available data spectrum and make it decomposed.

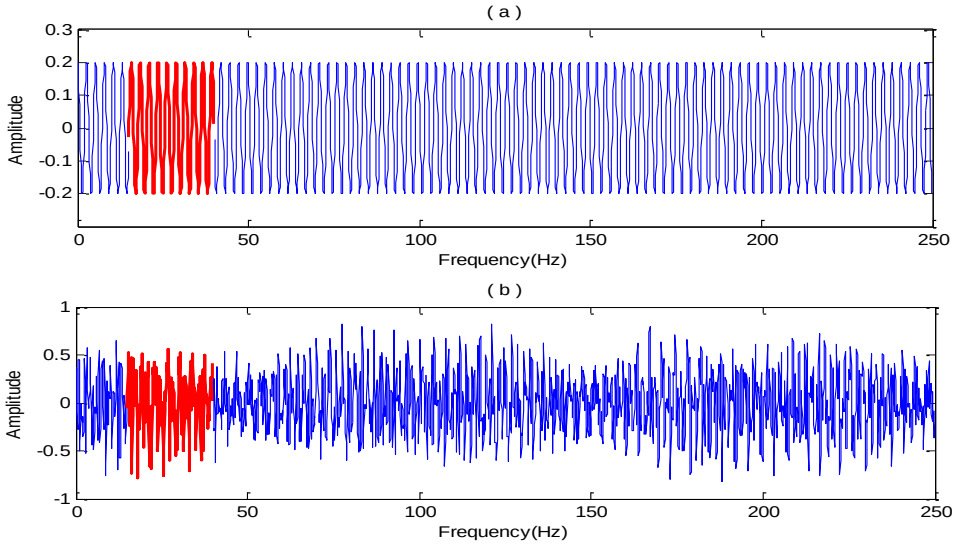

Figure 3.3: (a) Spectrum (real or imaginary) of an isolated spike; (b) Spectrum (real or imaginary) of a reflectivity series.

3.3.3 Matching Pursuit Decomposition

Matching pursuit is a type of numerical technique which involves finding the best matching projections of data onto an over-complete dictionary. Mallat and Zhang (1993) presented a thorough analysis on matching pursuit using time-frequency dictionaries. The basic idea is to reconstruct a signal by atom signals chosen from the dictionaries:

$$S(t) = \sum_{n=0}^{\infty} a_n g_{\gamma_n}(t) \tag{3.3}$$

where g_{γ_n} are the matched atoms and a_n are the cross-correlation coefficients for each matched atom.

So in this method, matching pursuit decomposition will be performed with a series of

sine waves within the limited data bandwidth as the atoms comprising that dictionary; hence, the procedure is listed below:

(1) Prepare a series of normalized sine waves of various frequency periods and phase shifts over the data band for the atom dictionary.

(2) Cross-correlate the spectrum with all the elements in the dictionary to find the best fit sinusoid and then subtract it from the original spectrum.

(3) Repeat this process on the residual spectrum until the residual spectrum falls below some energy threshold.

(4) Make a list of all matched sinusoids with the corresponding frequency periods, phase shifts and amplitudes.

(5) Extrapolate those sinusoids from zero frequency all the way to the Nyquist frequency in order to get the full spectral band recovered.

The above process can also be represented mathematically by Eq. 3.4:

$$F(f) = \sum_{n=1}^{k-1} C_n S_{a_n}(f) + r^k(f) \tag{3.4}$$

where $F(f)$ is the original band-limited spectrum (either real or imaginary), C_n is the cross-correlation coefficient at n^{th} iteration, $S_{a_n}(f)$ is the matched sinusoidal base at each iteration, and $r^k(f)$ is the residual spectrum at the beginning of k^{th} iteration. An ideal situation is that all the sinusoids representing their corresponding reflections are decomposed independently. If this would happen, interfering events can be accurately and perfectly resolved.

3.3.4 Principle of Orthogonality

The concept that two lines are perpendicular to one another has been extended into

higher dimensional spaces. In mathematics, two vectors are considered orthogonal if and only if their dot product is zero. Physically, orthogonality describes relation between objects as non-overlapping, uncorrelated, or independent.

Two nonzero real functions $\phi_1(t)$ and $\phi_2(t)$ defined in the interval $[t_1, t_2]$ are considered mutually orthogonal if the equation below is true:

$$\int_{t_2}^{t_1} \phi_1(t)\phi_2(t)dt = 0 \tag{3.5}$$

Further, a sequence of functions $\phi_1(t)$, $\phi_2(t)$, …, $\phi_n(t)$ are defined in the interval $[t_1, t_2]$. If any two of those functions satisfy the following equations:

$$\int_{t_1}^{t_2} \phi_i(t)\phi_j(t)dt = \begin{cases} 0 & i = j \\ k_i & i \neq j \end{cases} \tag{3.6}$$

Then this series of functions can be classified as an orthogonal set.

For instance, the sequence of trigonometric functions $\{1, \cos(\omega_1 t + \varphi_1), \cos(2\omega_1 t + \varphi_2), ..., \cos(n\omega_1 t + \varphi_n)\}$ just can be regarded as an orthogonal set of functions in the interval $[0, 2\pi / \omega]$.

However, for the case in this chapter, those sinusoidal bases used by MPD are not completely orthogonal over the available spectral band. Mathematically, sinusoidal signals are only considered mutually orthogonal in certain specific intervals such as integral multiple periods. However, the seismic usable band is determined by bandwidth of the wavelet which is relatively arbitrary. In other words, those atoms have to be cross-correlated with non-orthogonal composite spectrum. Consequently, the coefficients could never purely describe the correlations between those matched atoms and their desired corresponding sinusoids occurring in the spectrum. Moreover, narrower the data bandwidth, more likely those sinusoids will become non-orthogonal.

3.4 Synthetic Data Examples

3.4.1 Synthetics with Varying Signal-to-Noise Ratio (SNR)

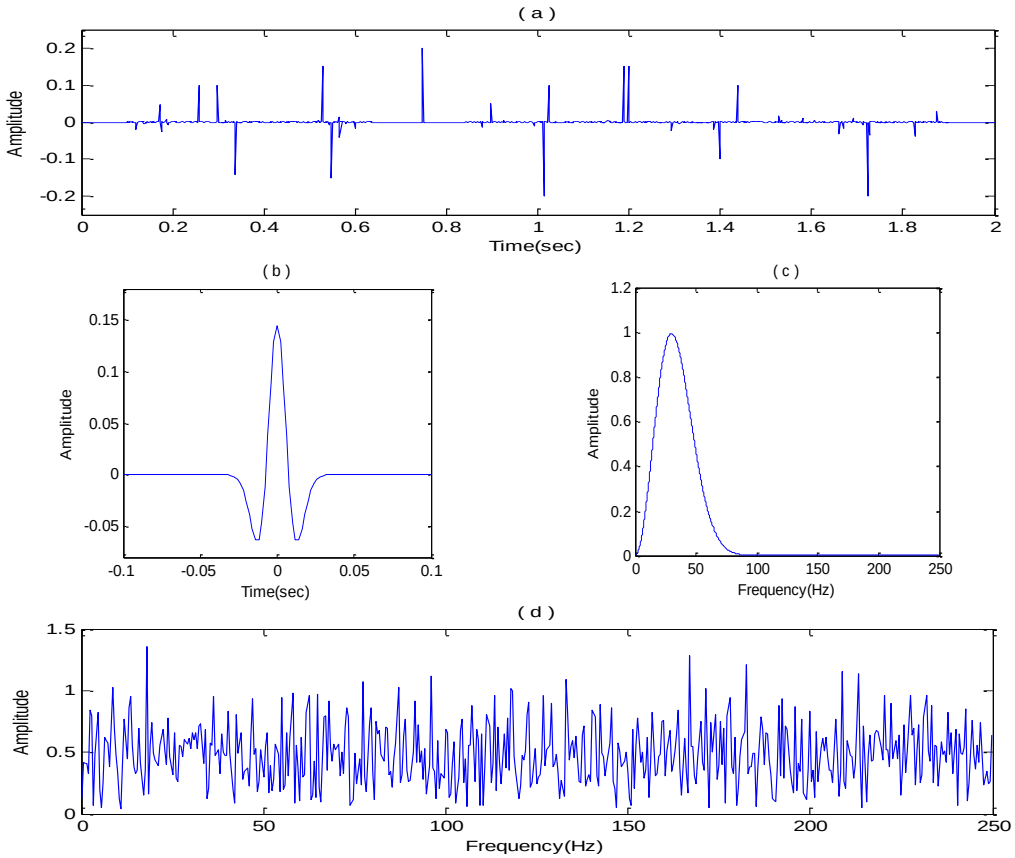

Figure 3.4: (a) Original reflectivity series; (b) 30Hz Ricker wavelet; (c) Amplitude spectrum of the wavelet; (d) Amplitude spectrum of the original reflectivity.

An original reflectivity series (Figure 3.4a) is given in which there are two closely spaced events around 1.2s. Original bandwidth of this reflectivity series ranges fully from zero frequency to the Nyquist frequency (Figure 3.4d). A 30 Hz Ricker wavelet (Figure 3.4b) is convolved with the original reflectivity to generate a synthetic seismic trace (Figure 3.5a). This band-limited trace is contaminated by random noise of varying signal-to-noise ratio of 10:1 (Figure 3.5b), 5:1 (Figure 3.5c) and 2:1 (Figure 3.5d), respectively. Correspondingly, spectrum (Figure 3.6a) of the clean synthetic is

limited within the wavelet band. Figure 3.6b, Figure 3.6c, and Figure 3.6d are the spectra of those noisy synthetics with different SNRs, in which increasing noise levels can be observed at high frequency end. Applying the frequency extrapolation program to these four traces, inversion results are obtained. The inverted reflectivity series (Figure 3.7a) for the clean synthetic is pretty good. All primary events have been revealed, and the two closed spaced events around 1.2s which cannot be resolved on the original trace have been successfully separated. Actually, the corresponding extended spectrum (Figure 3.8a) is almost the same as the original one (Figure 3.4d). The other three inverted reflectivity series are increasingly contaminated by noise as those cross-correlation coefficients are increasingly biased. The problem might be very serious when the signal-to-noise ratio is too low (Figure 3.7d). Some events have been distorted and even destroyed. In the frequency domain, extrapolated spectra would stay stable when the signal-to-noise ratio is good enough, but will deviate from true spectrum as too much noise is added. Observed from extended spectrum of the inverted reflectivity with SNR of 2:1 (Figure 3.8d), a large number of spectral components have been exaggerated, among which an extreme component has occurred around 75Hz. Nevertheless, as long as those major reflections are strong enough, they still can be successfully revealed.

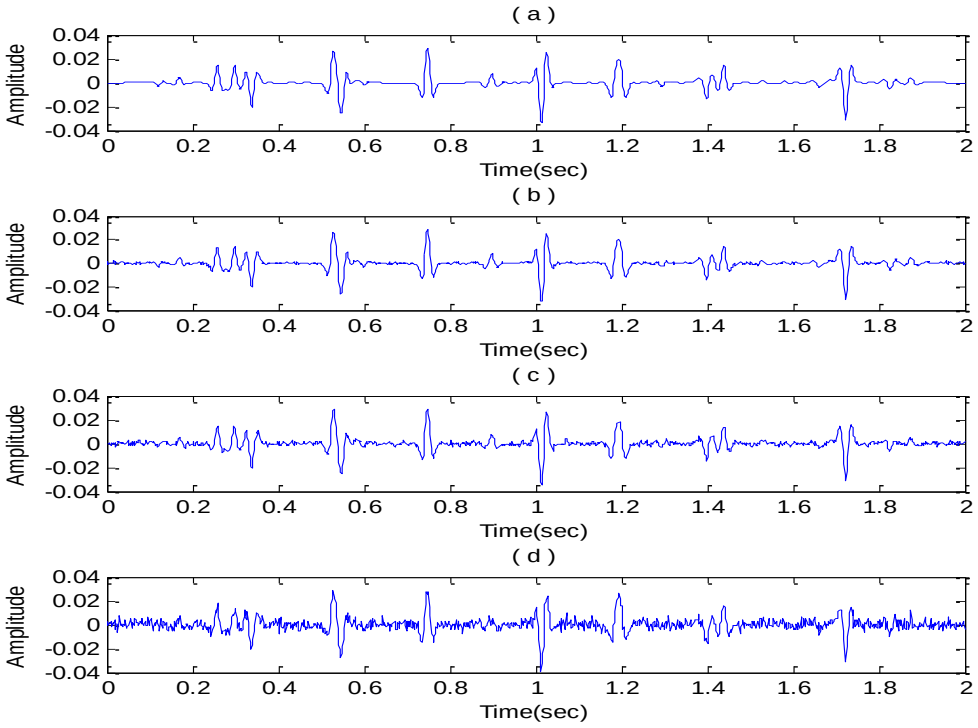

Figure 3.5: Synthetic traces with varying signal-to-noise ratio: (a) no noise; (b) SNR of 10:1; (c) SNR of 5:1; (d) SNR of 2:1.

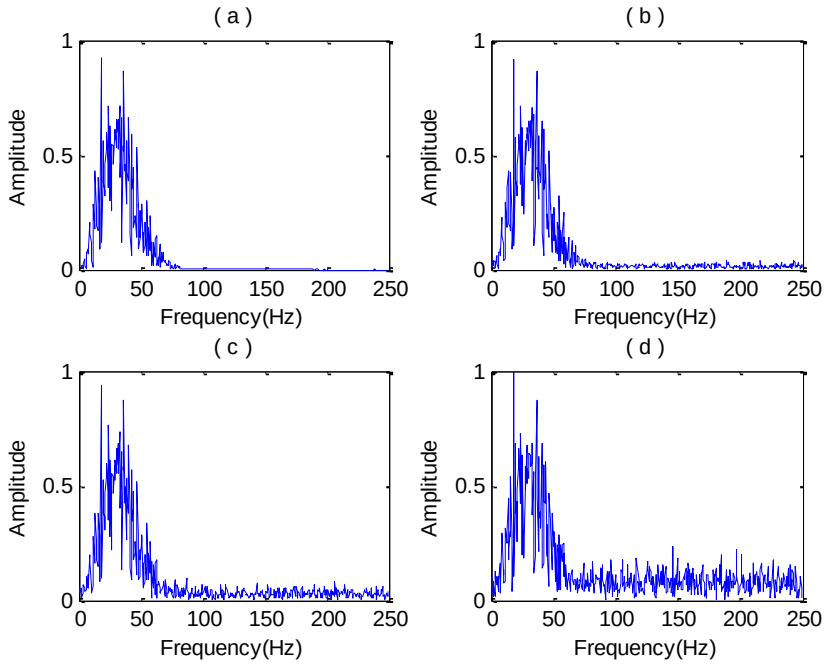

Figure 3.6: Spectra of synthetic traces with varying signal-to-noise ratio: (a) no noise; (b) SNR of 10:1; (c) SNR of 5:1; (d) SNR of 2:1.

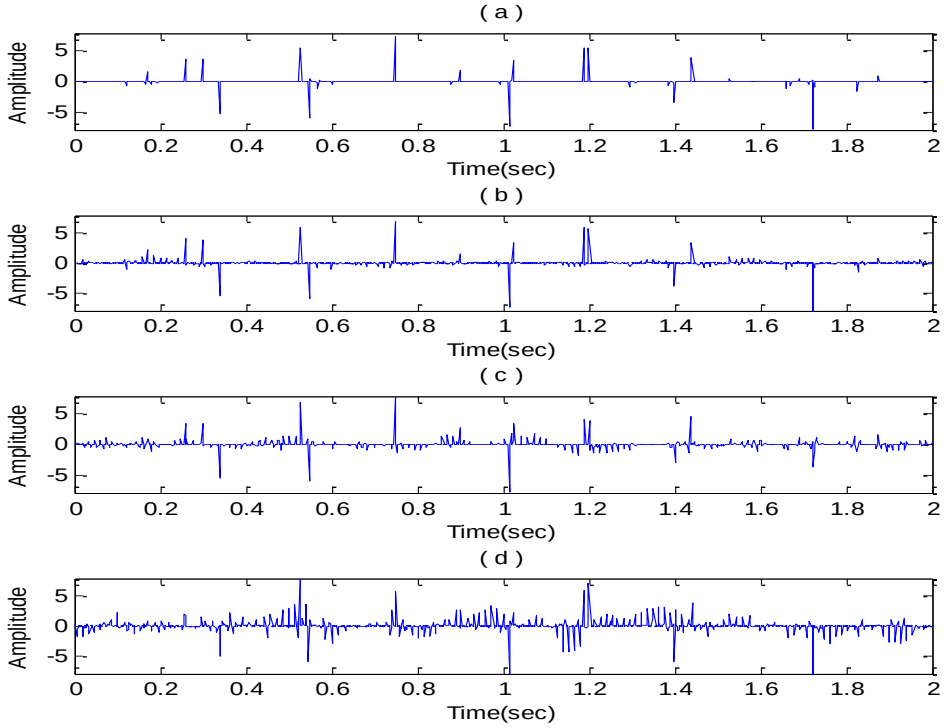

Figure 3.7: Inverted reflectivity for varying signal-to-noise ratio (DFT method): (a) no noise; (b) SNR of 10:1; (c) SNR of 5:1; (d) SNR of 2:1.

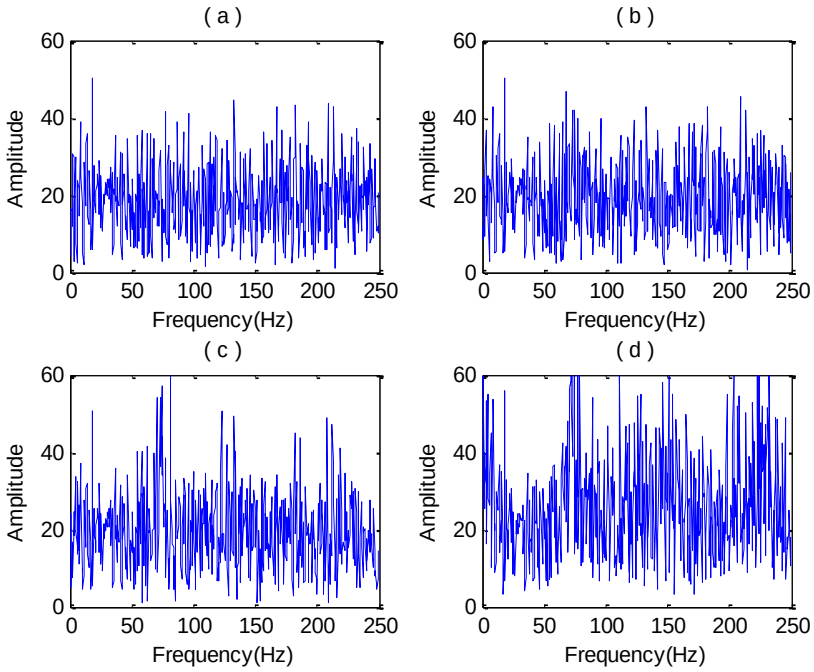

Figure 3.8: Spectra of inverted reflectivity for varying signal-to-noise ratio (DFT method): (a) no noise; (b) SNR of 10:1; (c) SNR of 5:1; (d) SNR of 2:1.

3.4.2 Synthetics with Different Wavelet Bandwidths

The available and usable data bandwidth for extrapolation will be narrowed if the wavelet bandwidth narrows. It is thus necessary to fit sinusoids over increasingly narrow bands and check how this method will work. The original reflectivity series is convolved with 30Hz Ricker wavelet (Figure 3.9a), 25Hz Ricker wavelet (Figure 3.9b), and 20Hz Ricker wavelet (Figure3.9c). Corresponding spectra are shown in Figure 3.10.

In Figure 3.9, an increasingly serious wavelet interference effect can be found on the traces of lower dominant frequencies, which would obviously lead to worse inversion results. Figure 3.11 presents the inverted reflectivity series and corresponding extrapolated spectra are shown in Figure 3.12.

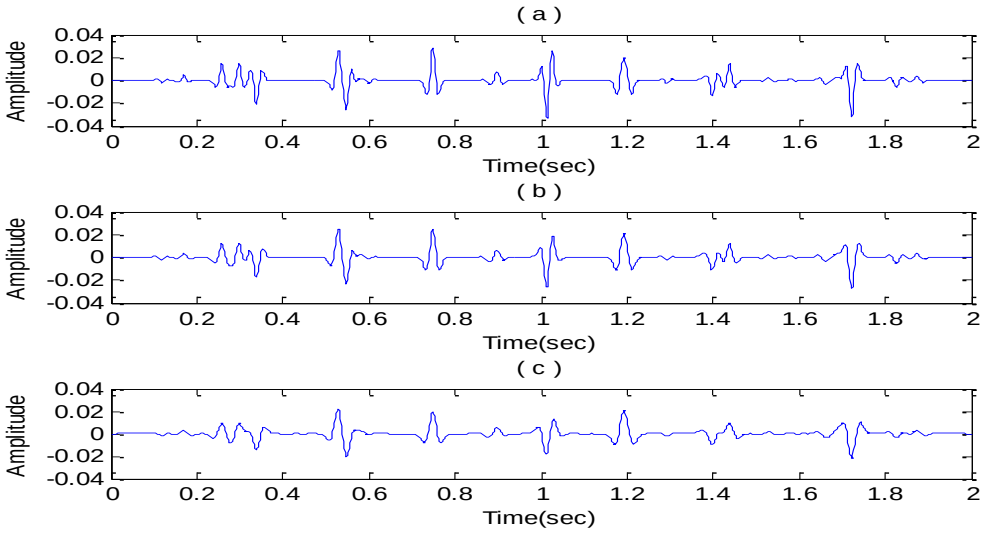

Figure 3.9: (a) Synthetic trace generated by 30Hz Ricker wavelet; (b) Synthetic trace generated by 25Hz Ricker wavelet; (c) Synthetic trace generated by 20Hz Ricker wavelet.

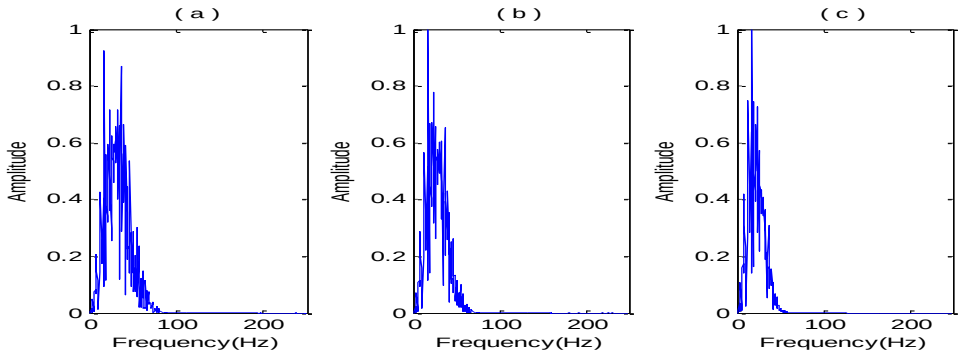

Figure 3.10: (a) Spectrum of the synthetic (30Hz); (b) Spectrum of the synthetic (25Hz); (c) Spectrum of the synthetic (20Hz).

The inversion result (Figure 3.11a) is fairly good for the case of 30Hz wavelet. The thin layer around 1.2s has been clearly resolved and most spiky events are recovered. For the case of 20Hz wavelet (Figure3.11c), however, the thin layer is inverted as one single event by the program instead of two separated ones. Also, the events between 0.5s and 0.6s have an apparent deviation from the true reflectivity. For two closely spaced events, their spectra will be two sinusoids with close frequency periods. This slight difference requires a broad enough bandwidth to be distinguished by MPD. Therefore, the program has not been able to separate the very closely spaced spikes within a narrow band as 20Hz wavelet. Interestingly, in the corresponding frequency domain, the extended spectrum for the narrower band case exhibits a lower energy level than the broader band case.

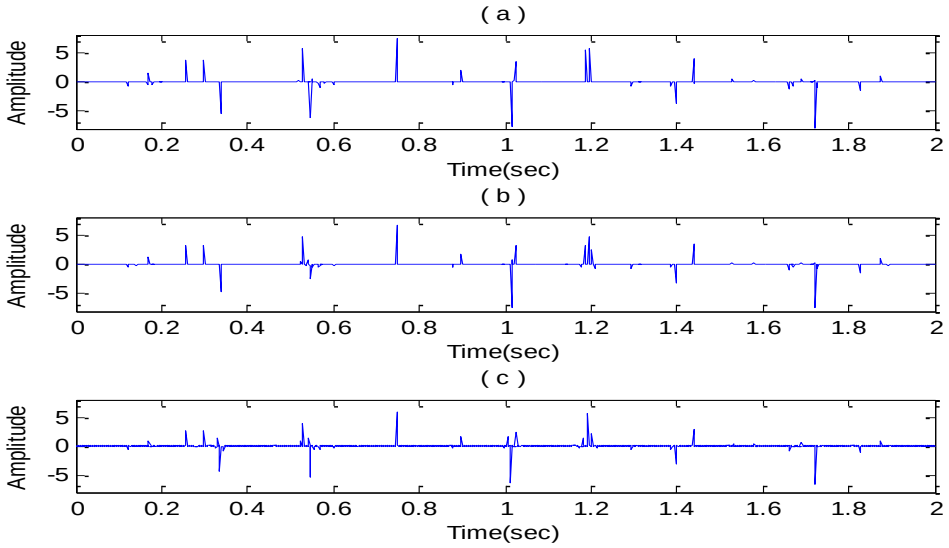

Figure 3.11: DFT method. (a) Inverted reflectivity (30Hz); (b) Inverted reflectivity (25Hz); (c) Inverted reflectivity (20Hz).

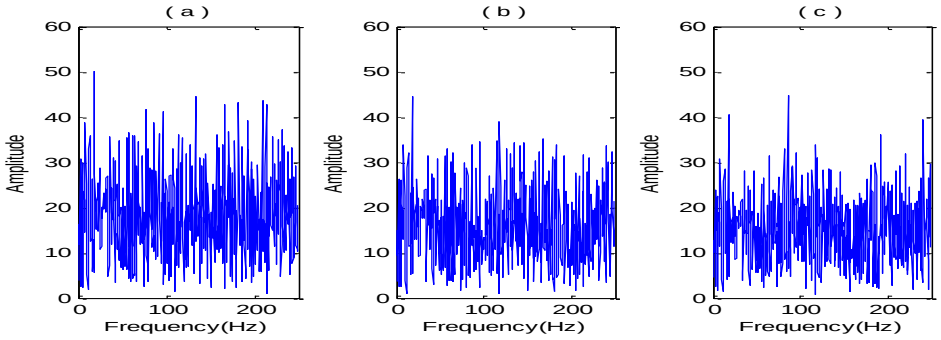

Figure 3.12: DFT method. (a) Spectrum of the inverted reflectivity (30Hz); (b) Spectrum of the inverted reflectivity (25Hz); (c) Spectrum of the inverted reflectivity (20Hz).

3.4.3 Well Log-derived Synthetics with High Complexity

A harder case for this frequency extrapolation method to invert should be seismograms with very high complexity. A well log-derived reflectivity series (Figure 3.13a) has reflection coefficients for almost every single time point ranging from 0.15s to 1.10s. The inversion result is shown in Figure 3.13c. Since the interference

effect is extremely serious on this seismogram, it will be difficult for matching pursuit decomposition to analyze the spectrum correctly. Consequently, true reflections might be suppressed while some false events might be created. Only the strongest events could be revealed.

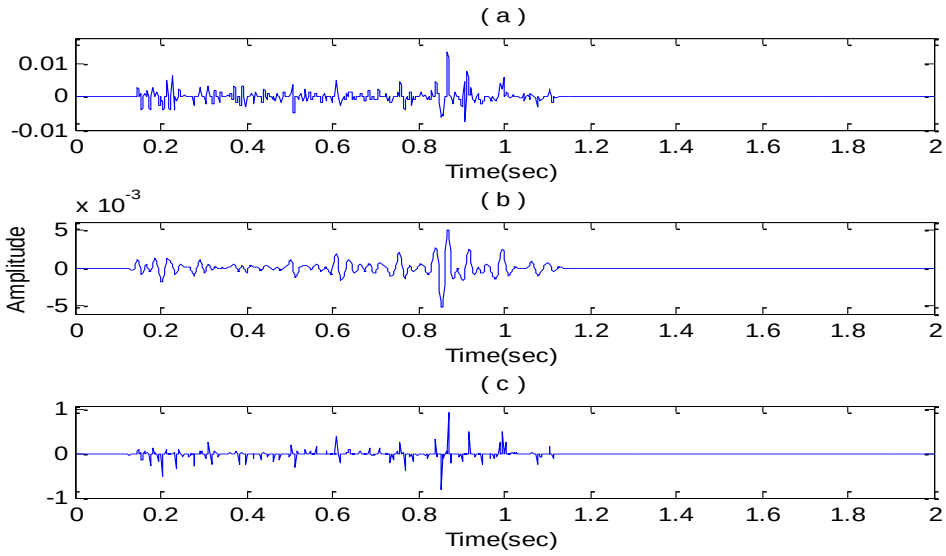

Figure 3.13: (a) Well log-derived reflectivity sequence; (b) Well log-derived synthetic seismogram (30Hz); (c) Inverted reflectivity for the synthetic seismogram (DFT).

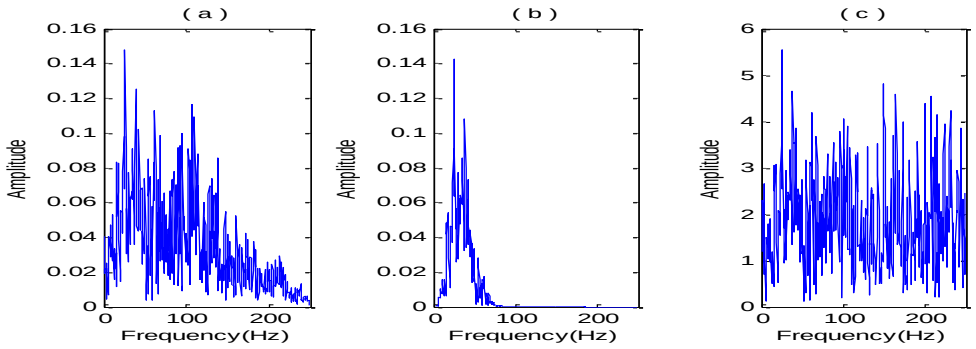

Figure 3.14: DFT method. (a) Spectrum of the well log-derived reflectivity; (b) Spectrum of the well log-derived synthetic seismogram; (c) Spectrum of the inverted reflectivity.

3.4.4 Wedge Model Tests

Band-limited seismic responses (Figure 3.15a and Figure 3.17a) for both even and odd spike pairs of varying thickness (Figure 3.16b and Figure 3.18b) are generated by convolving a 30Hz Ricker wavelet. For the even part, in the spectrally extended section (Figure 3.15b), Trace 36 has been resolved, which is a significant improvement in resolution when compared with Trace 26 in the low frequency synthetis (Figure 3.15a). This spectrally extended section is generated by convolving the corresponding inverted spiky output (Figure 3.16a) with a 60Hz Ricker wavelet. Another high frequency synthetic is provided by convolving the true wedge model (Figure 3.16b) with the same high frequency wavelet for comparison, where those thin beds can be resolved down to Trace 38. It has slightly better resolution than the spectrally extended result, even with the same broad band-pass (60Hz). After all, the spectral extension method can never perfectly make the band-limited data inverted. Observing the inversion result (Figure 3.16a), spike pairs are well resolved when the wavelets are still far enough apart. When it comes to the traces ranging from number 35 to 40, the program fails to recognize the true reflections and some false spikes are produced. Furthermore, for very thin layers, the spike pairs can not be resolved any more. For the odd part, similarly, the spectrally extended section (Figure 3.17b) has exhibited much more improved resolution than the original (Figure 3.17a), and its tuning thickness has been made close to the high frequency target (Figure 3.17c). For the corresponding inverted stick output (Figure 3.18a), those thin beds far below tuning thickness have not been correctly inverted, because time thickness of those seismic responses below tuning is almost constant. However, the inversion results

above tuning thickness are still well recovered and reasonable.

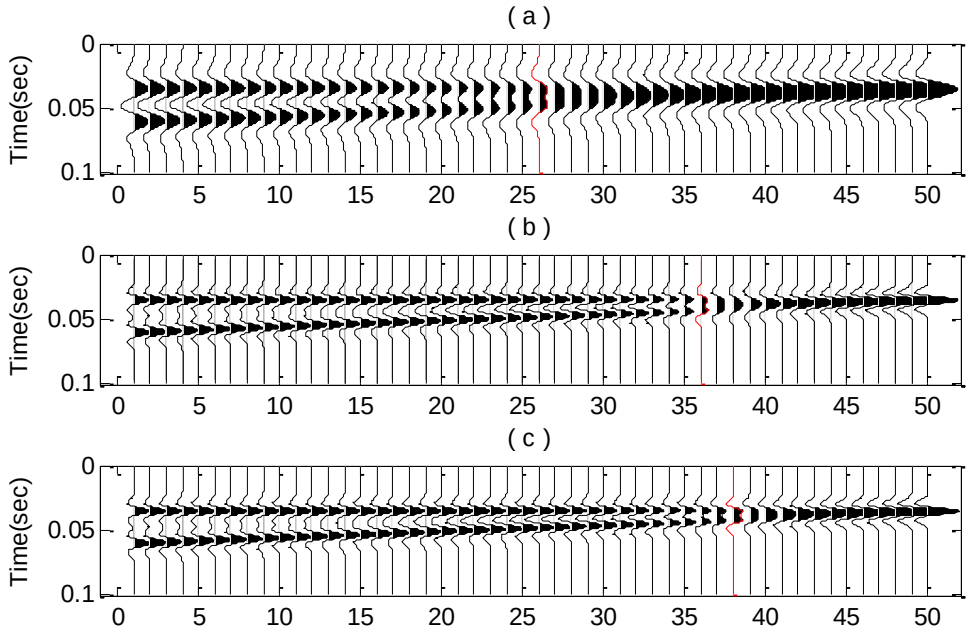

Figure 3.15: DFT method. (a) Seismic responses for even wedge model (30Hz); (b) Spectrally extended responses for the even wedge model (60Hz); (c) Seismic responses for even wedge model (60Hz).

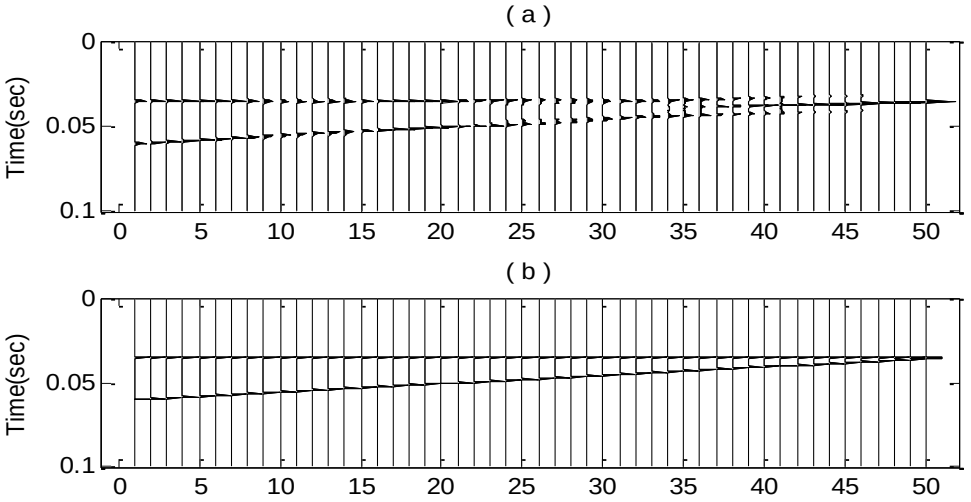

Figure 3.16: DFT method. (a) Inverted even wedge model; (b) True even spike pairs.

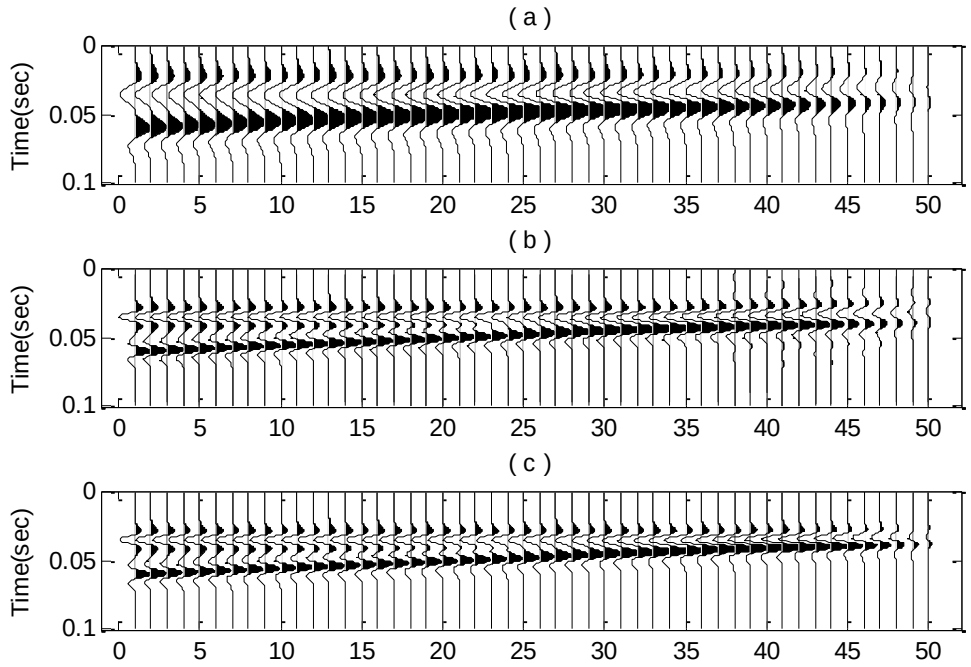

Figure 3.17: DFT method. (a) Seismic responses for odd wedge model (30Hz); (b) Spectrally extended responses for the odd wedge model (60Hz); (c) Seismic responses for odd wedge model (60Hz).

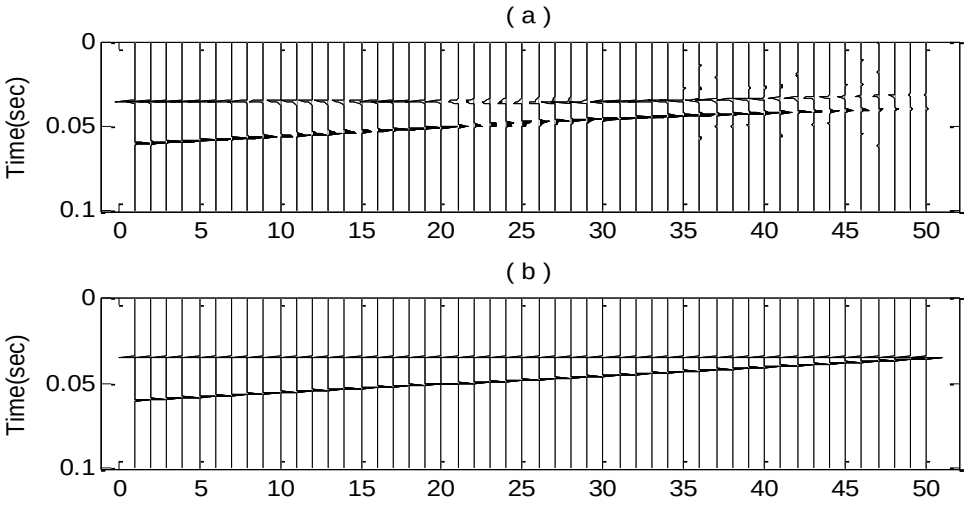

Figure 3.18: DFT method. (a) Inverted odd wedge model; (b) True odd spike pairs.

3.5 Real Data Examples

This frequency extrapolation approach will be tested on a real seismic section from the Blackfoot dataset. The original seismic image data (Figure 3.19) is a band-limited 2D section going across that 01-08-23-23 well. The seismic trace near the well location is denoted by red color. The spectral extension method is applied to the original section using the estimated wavelet extracted from corresponding surface seismic data. The section for inverted reflectivity series is displayed in Figure 3.21, in which some horizons could be clearly recognized. Furthermore, a higher frequency Ricker wavelet is used to make it band-limited in order to produce a high resolution section (Figure 3.20). Resolution of the original band-limited section has been significantly enhanced.

Viewing a comparison of the resolution enhanced section with the original section, it is clear that some indistinct boundaries between layers have become clearer with the spectral extension. Also, some thin beds that are totally unresolved in the original section have been separated in the high resolution section. Although the validity of the spectrally extended results is doubtful, the outputs produced by this method should be reasonable and the corresponding spectrum (Figure 3.22) does have been extended significantly.

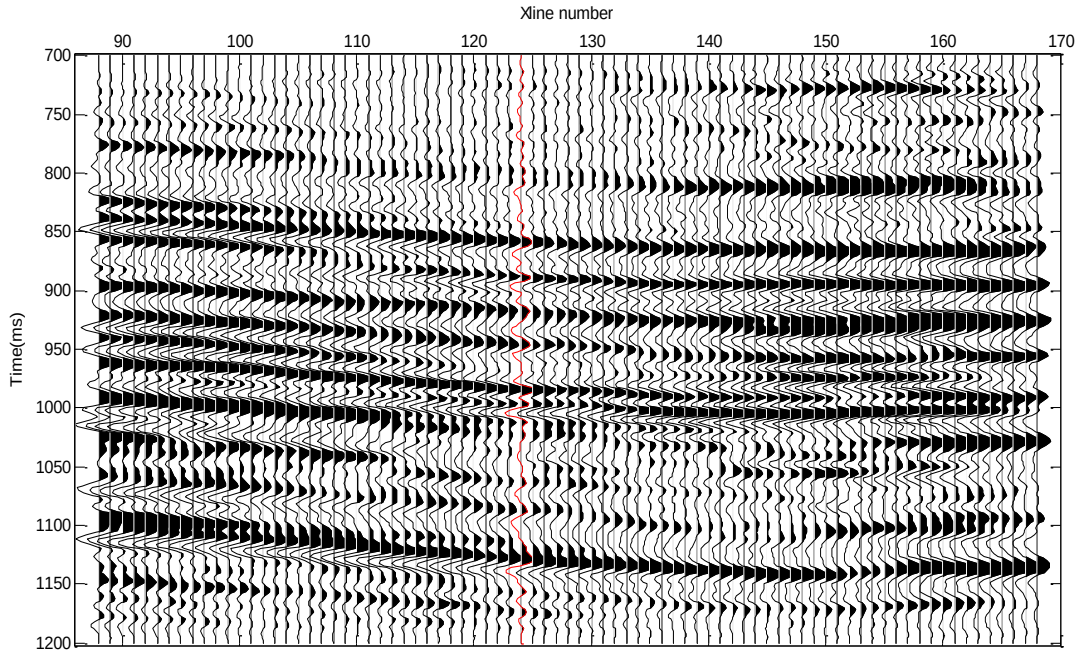

Figure 3.19: Original band-limited seismic section. The well location is near the trace denoted by red color.

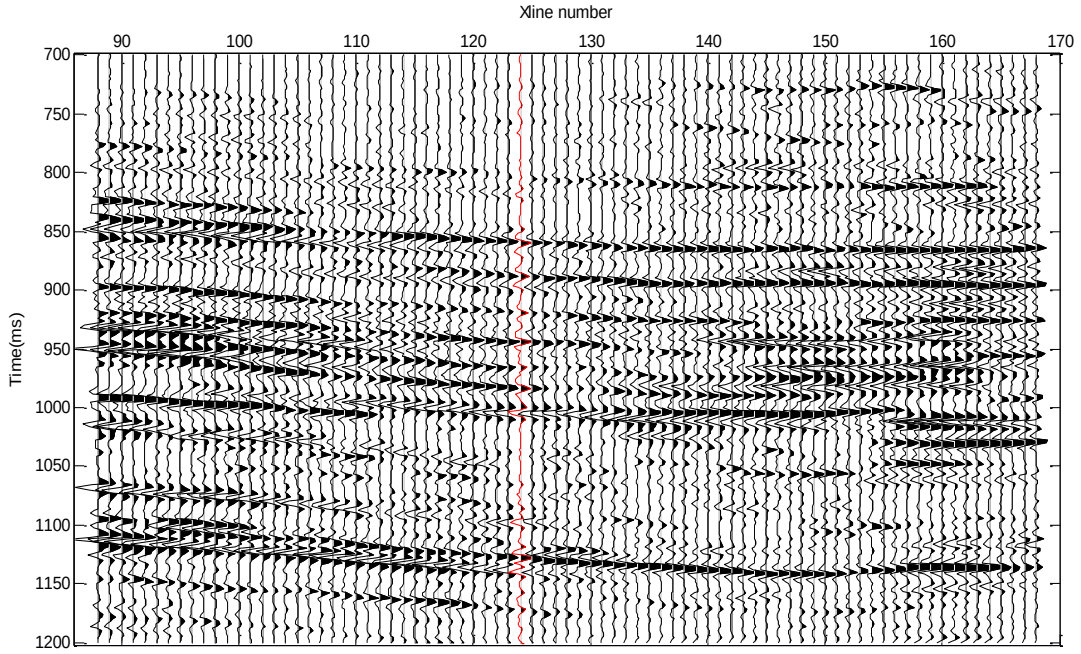

Figure 3.20: Resolution enhanced seismic section (bandwidth-extended) for DFT method.

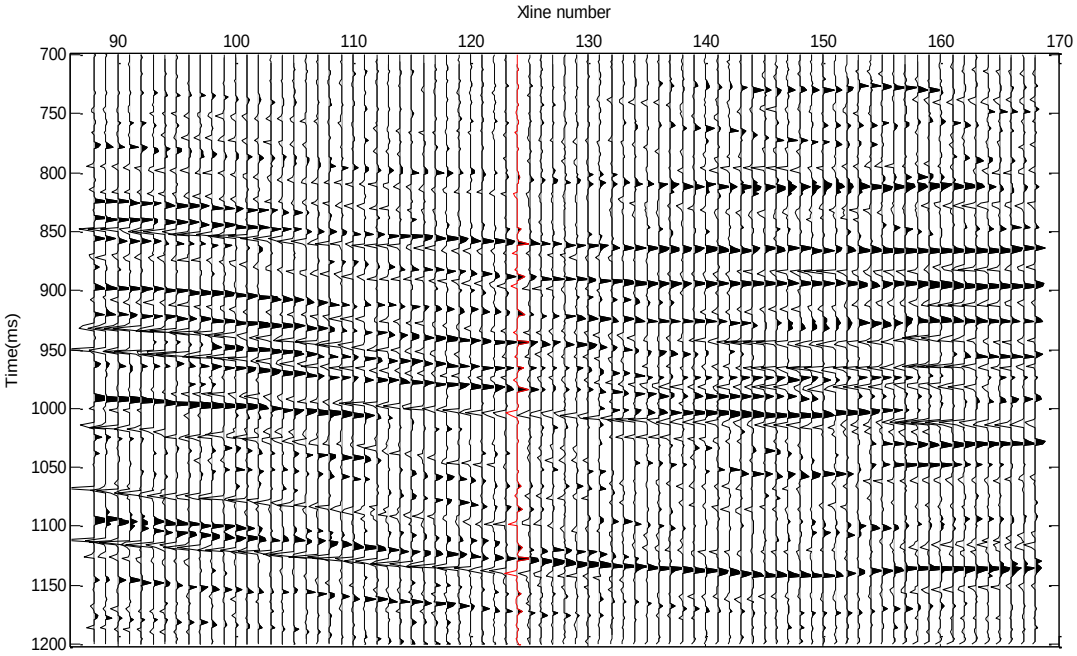

Figure 3.21: Inverted reflectivity section for DFT method.

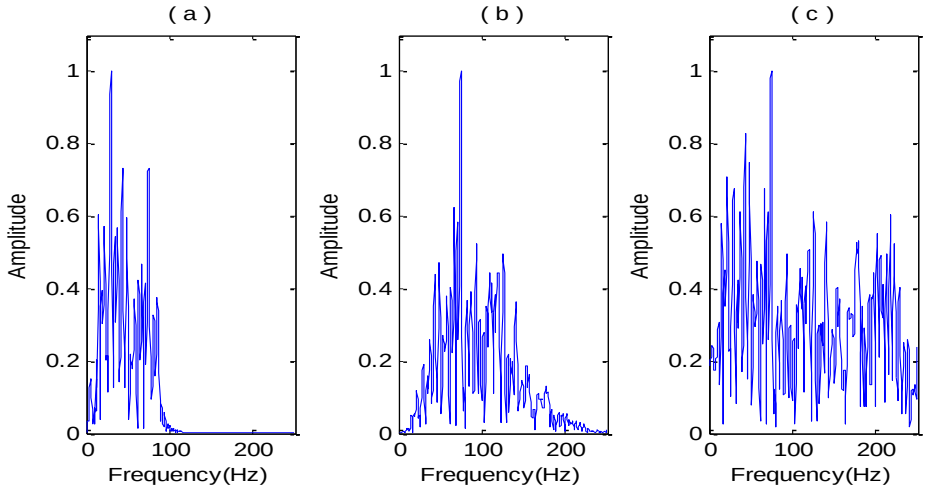

Figure 3.22: DFT method. (a) Spectrum of the original trace at well location; (b) Spectrum of the bandwidth-extended trace at well location; (c) Spectrum of the inverted reflectivity at well location.

3.6 Chapter Conclusion

Beginning with an illustration of the relationship between spectral information within the limited data bandwidth and the missing part outside, we proposed using the matching pursuit decomposition to unravel the superposition of a series of sinusoids within the usable band. This method resolves composite reflections by recognizing the amplitude, frequency period, and phase shift for each sinusoid within the available band corresponding to spikes in time domain. Extrapolating those matched sinusoids from zero frequency all the way to the Nyquist frequency could recover the original reflectivity, and thus have a chance to resolve thin beds below tuning thickness. The recovered reflectivity sequence can be filtered back to any desired bandwidth, which significantly improves the vertical resolution of original seismic data. However, it would be impossible for the program to resolve thin layers with extremely small thickness, as those sinusoidal bases are not completely uncorrelated over the limited spectral bandwidth. This is because matching pursuit decomposition requires orthogonal bases. Nevertheless, as shown in the real data examples, the method discussed in this chapter could successfully enhance seismic data resolution and has shown great potential as a practical tool for high resolution seismic interpretation.

Chapter 4

Spectral Extrapolation by Wiener Predictive Filters

Seismic wave propagation is subject to energy loss and frequency attenuation in the earth. Low frequencies filtered out during acquisition stage and high frequencies absorbed during seismic transmission may never be restored. However, according to the theory of Fourier analysis, general functions may be represented or approximated by sums of simpler trigonometric functions. There should be some necessary relationships between surviving spectral components and those that are missed. The missing high and low frequencies can thus be calculated from available spectral band by standard prediction techniques. In this chapter, two time-frequency analysis techniques: Matching Pursuit Decomposition (MPD) and Continuous Wavelet Transform (CWT), are employed to spectrally analyze the band-limited seismic data whereby spectra will be broadened on frequency gathers for resolution enhancement.

Section I: Wiener Prediction on MPD Frequency Gathers

The previous chapter has indicated that the spectrum of a reflectivity function for a layered earth can be represented as a superposition of a series of sinusoids with various frequency periods and amplitudes. As a matter of fact, the spectrum can also be modeled as an autoregressive (AR) process. Consequently, the prediction of the missing high and low frequencies from the available band heavily depends on the assumption that the reflectivity series is impulsive. However, if the reflectivity

function contains too many impulses, the ability of the AR modeling to pick up many sinusoids from a short portion within the band will be limited. Thus, in this section, band-limited seismic data will be spectrally decomposed by matching pursuit algorithm so that spectral extension could be performed locally instead of globally.

4.1 Autoregressive (AR) Model

In signal processing, an autoregressive model is a representation of a type of random process which specifies that output variables depend linearly on the previous values. Mathematically, it is defined as:

$$X_t = \sum_{i=1}^{p} \varphi_i X_{t-i} + c + \varepsilon_t \tag{4.1}$$

where φ_i are parameters of the model, c is a generalized constant, and ε_t is the random noise.

For the layered earth with an assumed sparse structure, the reflectivity function will be zero everywhere except at some specific times. Therefore, it must have the mathematical form:

$$r(t) = \sum_{k=1}^{N} r_k \delta(t - \tau_k) \tag{4.2}$$

where N is total number of those interfaces and τ_k indicates two-way travel time for the k^{th} layer. Consequently, the corresponding spectrum for the reflectivity function is constrained to have a form as following:

$$R(f) = \sum_{k=1}^{N} r_k e^{-i2\pi f \tau_k} \tag{4.3}$$

Separating the complex spectrum into real and imaginary parts:

$$\mathrm{Re}(R_f) = \sum_{k=1}^{N} r_k \cos(2\pi f \tau_k) \tag{4.4}$$

$$\mathrm{Im}(R_f) = \sum_{k=1}^{N} r_k \sin(2\pi f \tau_k) \tag{4.5}$$

Hence, both the real and imaginary part of the spectrum are the sum of N sinusoids with frequency periods of $2\pi\tau_k$. Each single sinusoid can be modeled as a simple autoregressive process. So in the case of many layers, the spectrum could be modeled as a superposition of many autoregressive processes:

$$R_j = \sum_{k=1}^{p} \alpha_k R_{j-k} \tag{4.6}$$

where α_k are model parameters (filter coefficients) and p is number of model parameters which is also the filter length. As a matter of fact, Eq.4.6 is the special form for Eq.4.1 where the constant term and random noise are not taken into account.

4.2 Calculation of Predictive Coefficients

To predict missing spectral components outside the band of the wavelet, a set of equations has to be established in order to solve for those predictive coefficients. A linear equation of p unknowns will be given, assuming a current output is calculated based on its own previous p points. The current output will be subsequently utilized as one of the inputs for later calculations. Consequently, the set of equations can be represented in a matrix form (Eq. 4.7) by using up all spectral components within the available data bandwidth.

$$\begin{bmatrix} R_1 \\ R_2 \\ R_3 \\ \bullet \\ \bullet \\ \bullet \\ R_q \end{bmatrix} = \begin{bmatrix} R_0 & R_{-1} & R_{-2} & \bullet & \bullet & \bullet \\ R_1 & R_0 & R_{-1} & \bullet & \bullet & \bullet \\ R_2 & R_1 & R_0 & \bullet & \bullet & \bullet \\ \bullet & \bullet & \bullet & \bullet & & \bullet \\ \bullet & \bullet & \bullet & & \bullet & \bullet \\ \bullet & \bullet & \bullet & & & \bullet \\ R_{q-1} & R_{q-2} & R_{q-3} & \bullet & \bullet & \bullet \end{bmatrix} \begin{bmatrix} \alpha_1 \\ \alpha_2 \\ \alpha_3 \\ \bullet \\ \bullet \\ \bullet \\ \alpha_p \end{bmatrix} \tag{4.7}$$

The rectangular matrix has q rows and p columns. Practically, the number of the linear equations should be larger than that of unknowns so that the problem of solving the equation system (Eq.4.7) is overdetermined. As a result, the extended spectrum will be predicted in a least-squares error sense. The autoregressive model parameters solved in this way could also be considered as coefficients of so-called Wiener predictive filter. The idea of Wiener (1942) is just to transform an input into a desired output as nearly as possible, which implies that the sum of the squares of differences between the filter output and the desired result is minimized. Therefore, those spectral components within the usable band are trained with Wiener's theory to generate predictive filters for spectral extension.

4.3 Time-Frequency Analysis by Matching Pursuit

The spectrum (Eq.4.3) obtained from traditional Fourier transform reflects global spectral information representing composite events along the whole seismic trace. Superposition of various sinusoids in frequency domain may lead to serious instability problem in the extended frequencies, or even totally fail the algorithm. Therefore,

time-frequency spectral decomposition by matching pursuit is performed in this section to spectrally analyze the seismic data locally. Generally in signal processing, time-frequency analysis techniques study a signal in both the time and frequency domain simultaneously using various time-frequency representations. In the case of this section, the atom dictionary for matching pursuit decomposition would just be composed of zero-phase Ricker wavelets with various dominant frequencies. The algorithm is similar to that discussed in Chapter 3. The differences lie in the bases and the corresponding domains used. Therefore, seismic data are cross-correlated with all the elements in the dictionary and the best matched atom is regarded as the best representation for the signal at current iteration. So the matched wavelet is subtracted from the original signal and this process is repeated until the signal energy falls below some threshold. Then, all the matched atoms will constitute a two-dimensional time-frequency plane for further analysis. For each matched wavelet, a Wiener predictive filter will be specially designed to extrapolate the frequencies outside the limited band for enhancing data resolution locally.

However, Ricker wavelets are non-orthogonal and can never correlate events in seismic data without disturbance. Inaccurate cross-correlation coefficients may lead to biased decomposed results or bring about additional noise. For instance, two closely-spaced interfering events with identical amplitudes will have asymmetry problem in the spectral information by matching pursuit.

Chen and Castagna (2012) proposed an improved version of MPD, which is called Fractional matching pursuit decomposition (FMPD). This is achieved by subtracting a fractional portion of the cross-correlation coefficient which is supposed to crudely

handle the nonorthogonality issue for those bases. Figure 4.1c just displays the FMPD spectra for the synthetic seismic trace (Figure 4.1b) whose central frequency is around 30Hz. Two spectra around 1.4s for the odd spike pair have demonstrated symmetrical characteristic which might probably be seriously biased if conventional MPD is applied instead.

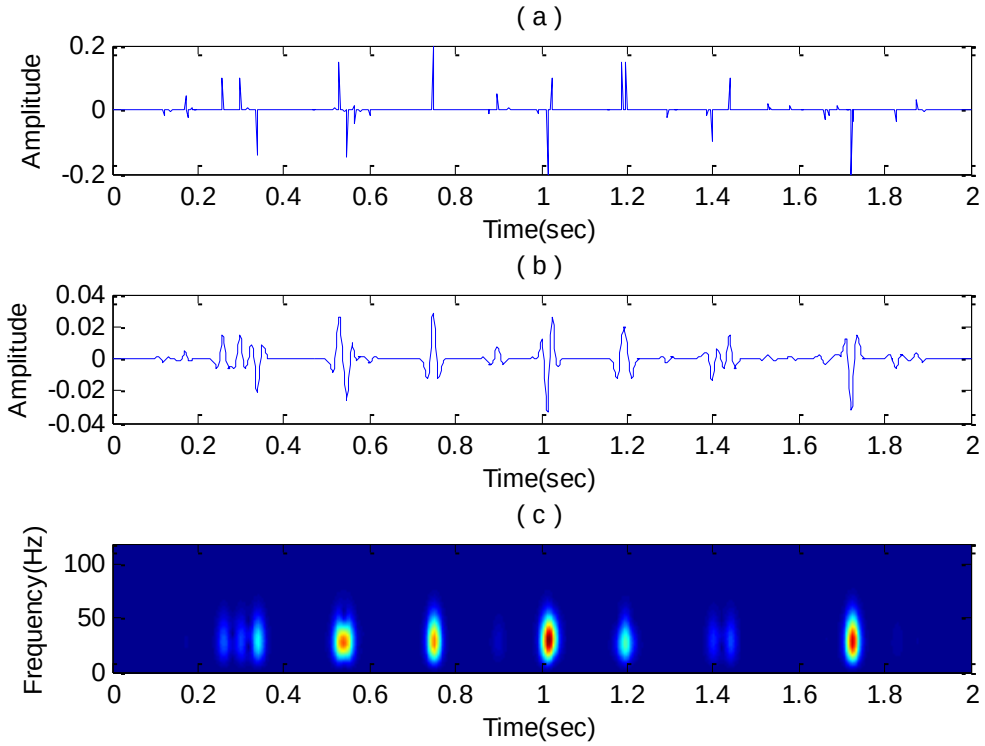

Figure 4.1: (a) Original reflectivity series; (b) Synthetic trace generated by 30Hz Ricker wavelet; (c) Time-frequency analysis of the trace by FMPD.

4.4 Synthetic Data Examples

4.4.1 Synthetics with Varying Signal-to-Noise Ratio (SNR)

To test this prediction technique by matching pursuit algorithm, the original reflectivity series is again convolved with a 30Hz Ricker wavelet for preparing synthetic traces with varying signal-to-noise ratios (Figure 4.2). Their corresponding inversion results are listed in Figure 4.4. For the clean synthetic (Figure 4.2a), almost all events are recovered in accordance with the true reflectivity sequence. A slight difference consists in the closely spaced spike pair around 1.2s which has not been completely restored due to nonorthogonality occurring in matching pursuit with Ricker wavelets. Nevertheless, the two events that cannot be resolved in the original data have been separated to an acceptable degree. When noise is added in, closely spaced spikes might not be well resolved, since noise disturbance is uncontrollable, so that the separated events might be inverted as one single event (Figure 4.4b and Figure 4.4c). Furthermore, when noise is serious (Figure 4.2d), along with those primary events, many false spikes are produced, which would probably undermine further interpretation. In this case, inversion results would be considered unreasonable.

Original spectra for those synthetic traces are displayed in Figure 4.3 and the corresponding extended results are shown in Figure 4.5. It is evident that with noise level increased, more unwanted spectral components would become dominant in the broadened spectrum (Figure 4.5d).

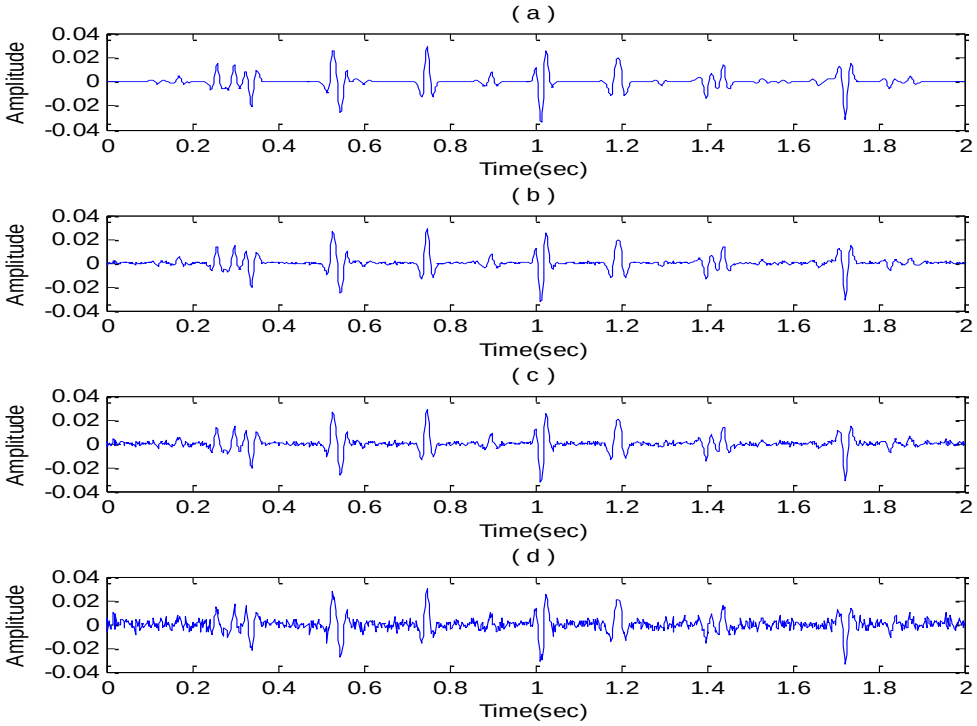

Figure 4.2: Synthetic traces with varying signal-to-noise ratio: (a) no noise; (b) SNR of 10:1; (c) SNR of 5:1; (d) SNR of 2:1.

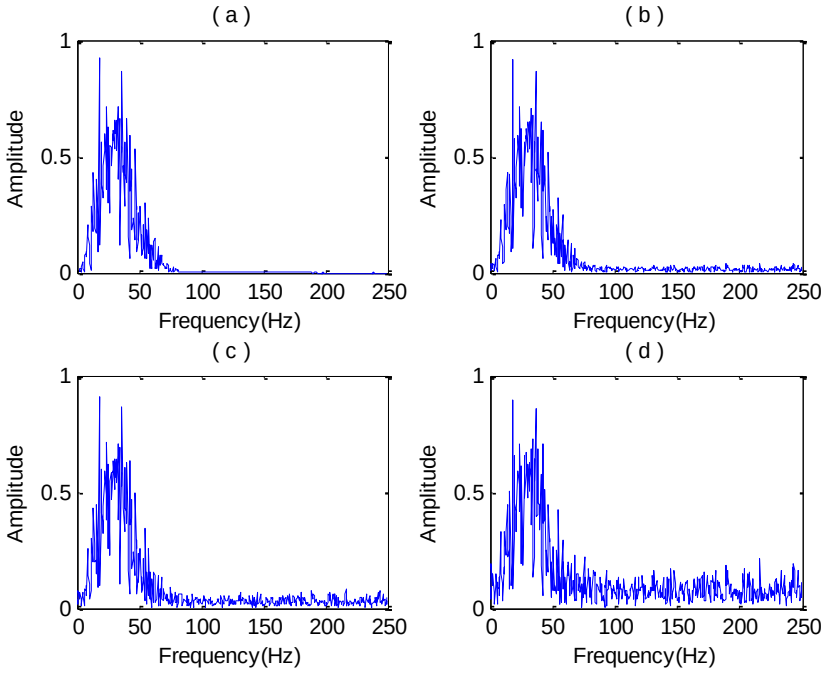

Figure 4.3: Spectra of synthetic traces with varying signal-to-noise ratio: (a) no noise; (b) SNR of 10:1; (c) SNR of 5:1; (d) SNR of 2:1.

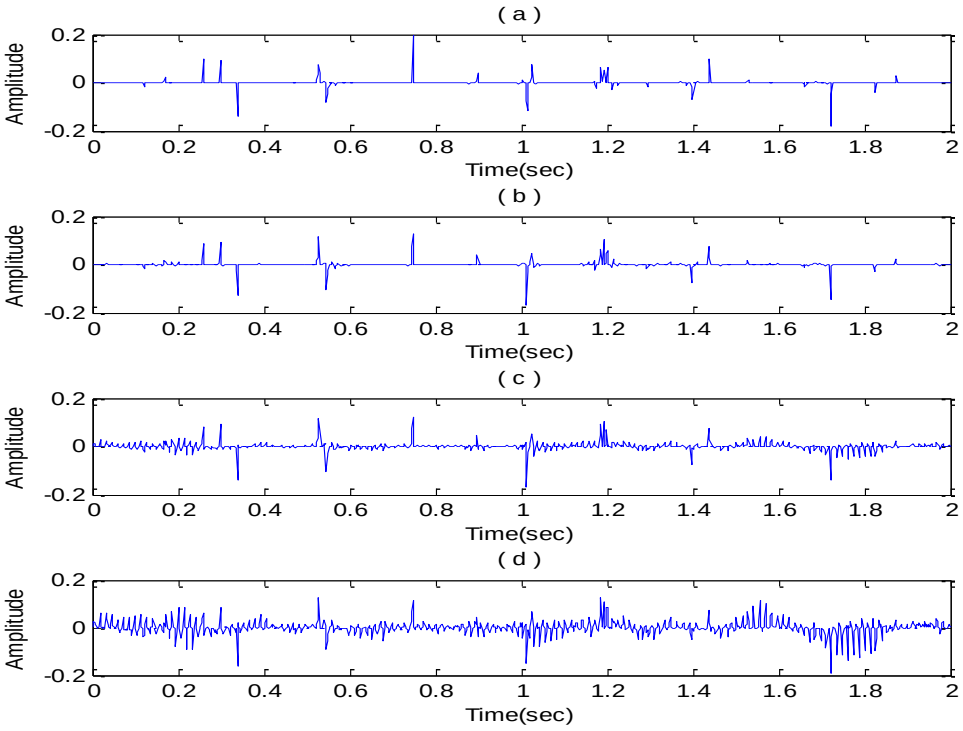

Figure 4.4: Inverted reflectivity for varying signal-to-noise ratio (MPD method): (a) no noise; (b) SNR of 10:1; (c) SNR of 5:1; (d) SNR of 2:1.

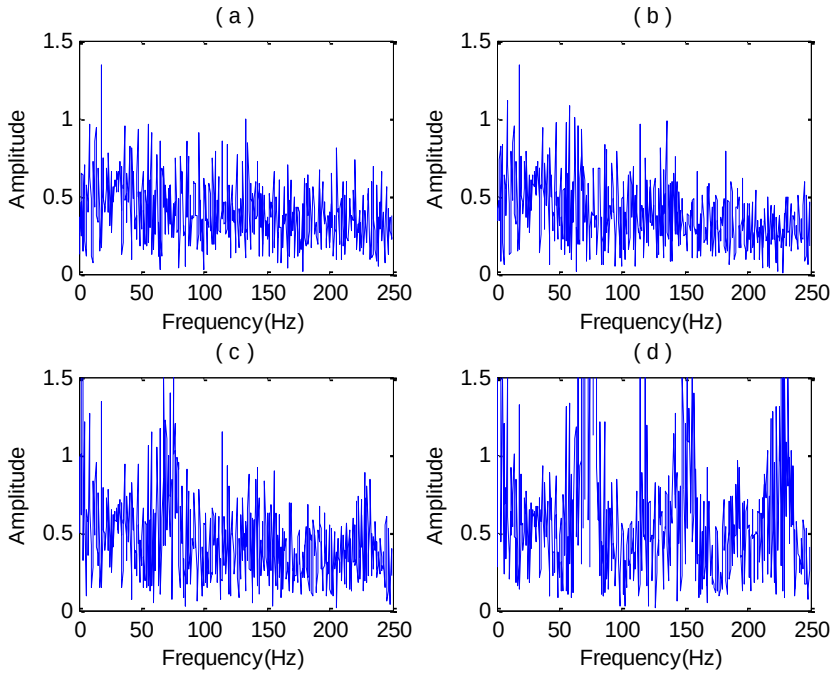

Figure 4.5: Spectra of inverted reflectivity for varying signal-to-noise ratio (MPD method): (a) no noise; (b) SNR of 10:1; (c) SNR of 5:1; (d) SNR of 2:1.

4.4.2 Synthetics with Different Wavelet Bandwidths

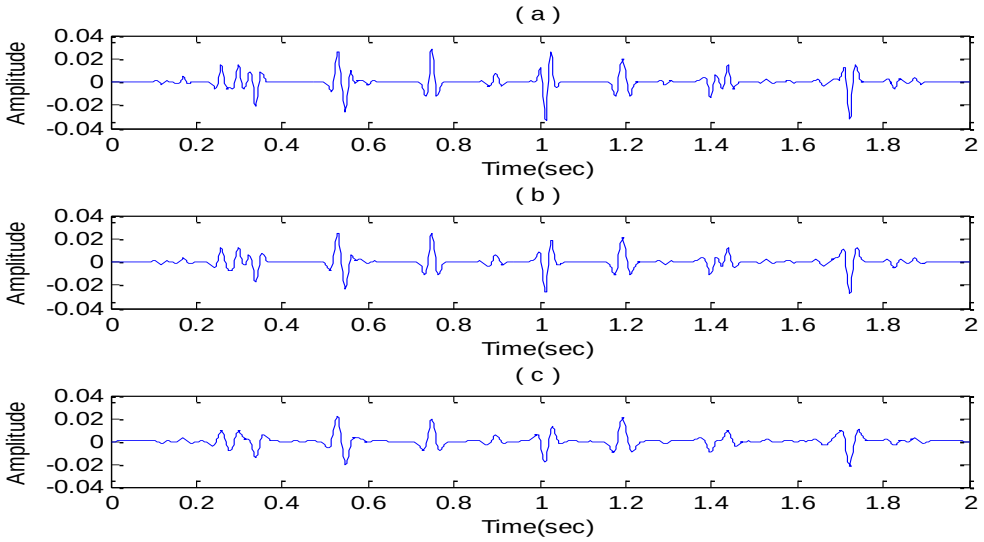

Figure 4.6: (a) Synthetic trace generated by 30Hz Ricker wavelet; (b) Synthetic trace generated by 25Hz Ricker wavelet; (c) Synthetic trace generated by 20Hz Ricker wavelet.

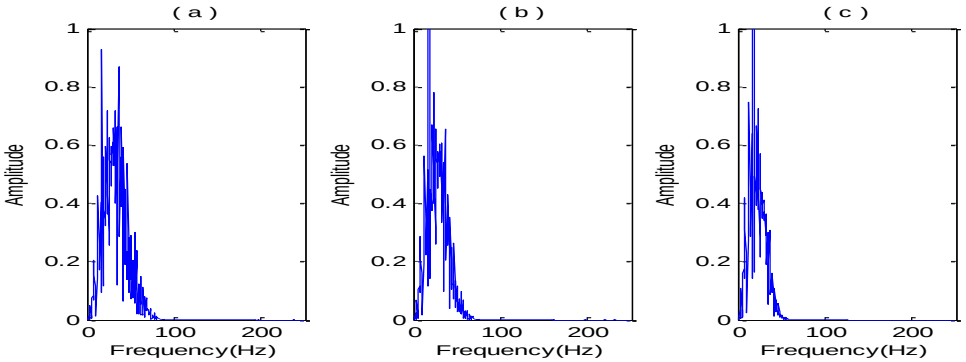

Figure 4.7: (a) Spectrum of the synthetic (30Hz); (b) Spectrum of the synthetic (25Hz); (c) Spectrum of the synthetic (20Hz).

Since matching pursuit decomposition using nonorthogonal bases is vulnerable to events interference, it is thus necessary to test this spectral prediction method with different data bandwidths. Three synthetic traces (Figure 4.6) are generated by 30Hz, 25Hz, and 20Hz Ricker wavelets, respectively. Interference effect becomes increasingly obvious as the wavelet band narrows. As expected, inversion results for

narrower bandwidths are of inferior quality. For the inverted reflectivity with 30Hz wavelet (Figure 4.8a), closely spaced spikes could still be resolved. Unfortunately, for the 25Hz wavelet case (Figure 4.8b), the spike pair around 1.2s starts to be recognized by the program as one single reflection rather than two separated events. Furthermore, with the wavelet bandwidth continuously narrowed, the spike pair has been completely suppressed such that only one isolated spike has been inverted. Therefore, this method could only resolve events separated enough apart, but doesn't work well for reflections that are too close.

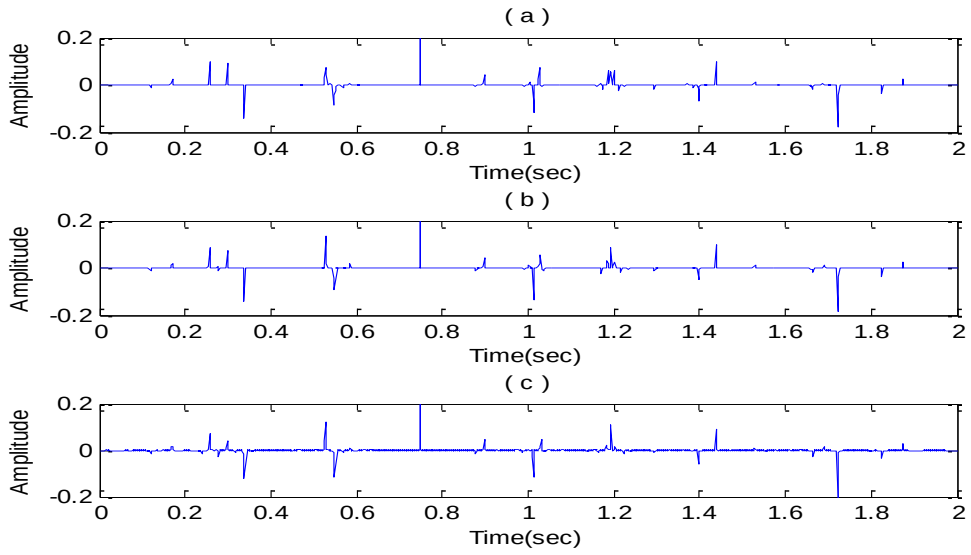

Figure 4.8: MPD method. (a) Inverted reflectivity (30Hz); (b) Inverted reflectivity (25Hz); (c) Inverted reflectivity (20Hz).

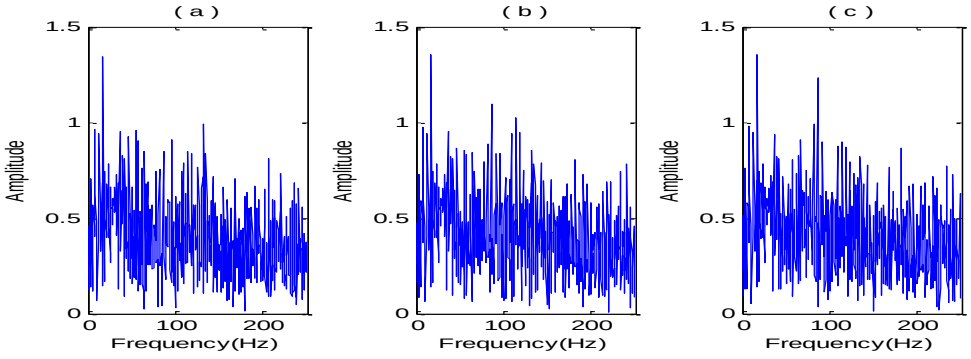

Figure 4.9: MPD method. (a) Spectrum of the inverted reflectivity (30Hz); (b) Spectrum of the inverted reflectivity (25Hz); (c) Spectrum of the inverted reflectivity (20Hz).

4.4.3 Well Log-derived Synthetics with High Complexity

The well log-derived synthetic seismogram (Figure 4.10b) is employed again to examine the method in this section, since the well log-derived reflectivity sequence (Figure 4.10a) has high complexity in which the interference effect is regarded as extremely serious. The inversion result is presented in Figure 4.10c.

Similarly, two very closely spaced events near 1.0s are inverted by the program as one single event. Worse still, an apparently erroneous spike with negative polarity has been produced around 0.2s, where the true reflectivity should be dominated by positive spikes. Consequently, unless major reflections are strong enough, inversion results may be unreliable when too much interference occurs.

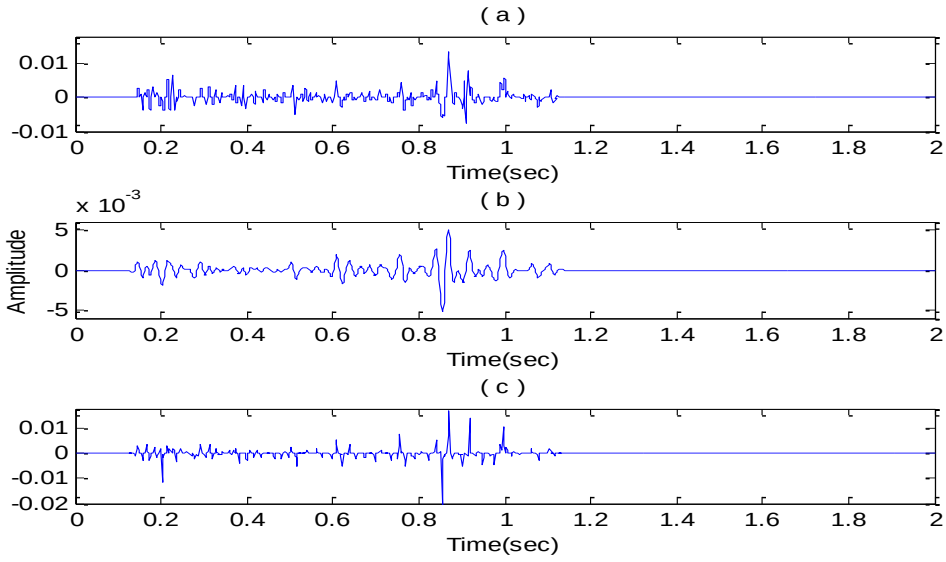

Figure 4.10: (a) Well log-derived reflectivity sequence; (b) Well log-derived synthetic seismogram (30Hz); (c) Inverted reflectivity for the synthetic seismogram (MPD).

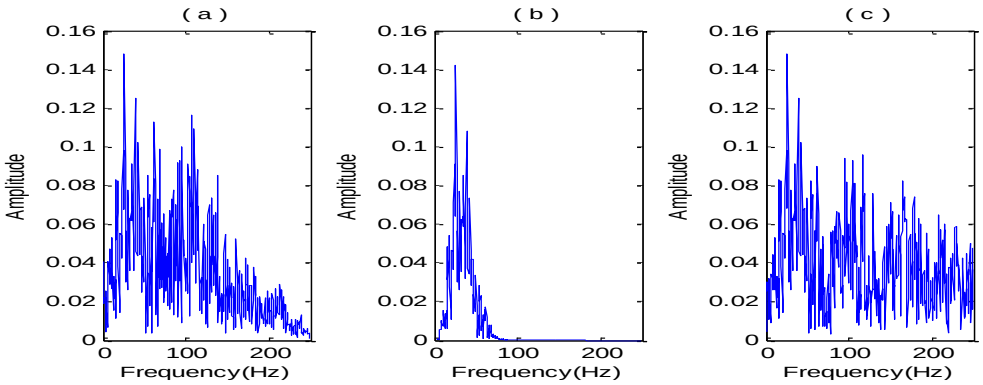

Figure 4.11: MPD method. (a) Spectrum of the well log-derived reflectivity; (b) Spectrum of the well log-derived synthetic seismogram; (c) Spectrum of the inverted reflectivity.

4.4.4 Wedge Model Tests

True comparisons are also made for this method on both the even and odd wedge models, where low frequency synthetics are generated by 30Hz Ricker wavelet and high frequency ones are generated by 60Hz Ricker wavelet. This time the spectrally extended sections (Figure 4.12b and Figure 4.14b) could not achieve the resolving capability of their comparatives (Figure 4.12c and Figure 4.14c). Examining the corresponding spiky outputs (Figure 4.13a and Figure 4.15a), when the spikes are still far enough apart, inverted spike pairs can be well resolved. For the even part, as layer thickness gets thinner, some tiny false spikes are produced between Trace 20 and Trace 35. This is because wavelet interference pattern of the waveforms at those thicknesses would mislead the matching pursuit program into considering the side lobes as primary events to invert. When the layer thickness approaches zero, the spike pairs will then become totally unresolved. Furthermore, for the odd pairs, those bed thicknesses are still inverted to be constant when they go below tuning thickness. Nevertheless, this method does increase the resolution to some degree. The even

wedge responses can be resolved at a thinner layer (Figure 4.12b), whereas the tuning thickness has been approached to a smaller thickness (Figure 4.14b) when compared with the original synthetics (Figure 4.12a and Figure 4.14a).

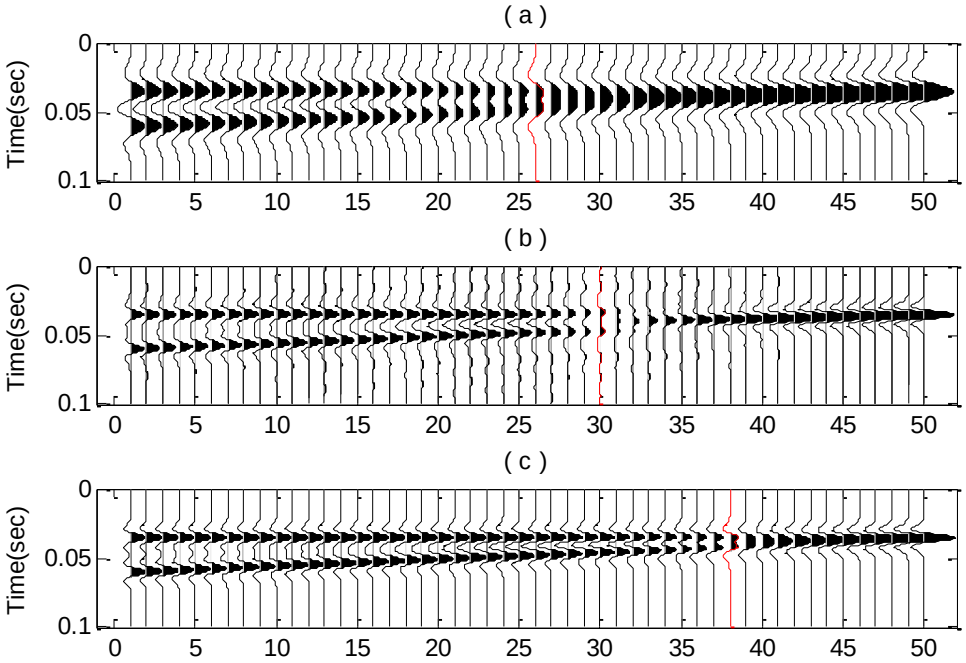

Figure 4.12: MPD method. (a) Seismic responses for even wedge model (30Hz); (b) Spectrally extended responses for the even wedge model (60Hz); (c) Seismic responses for even wedge model (60Hz).

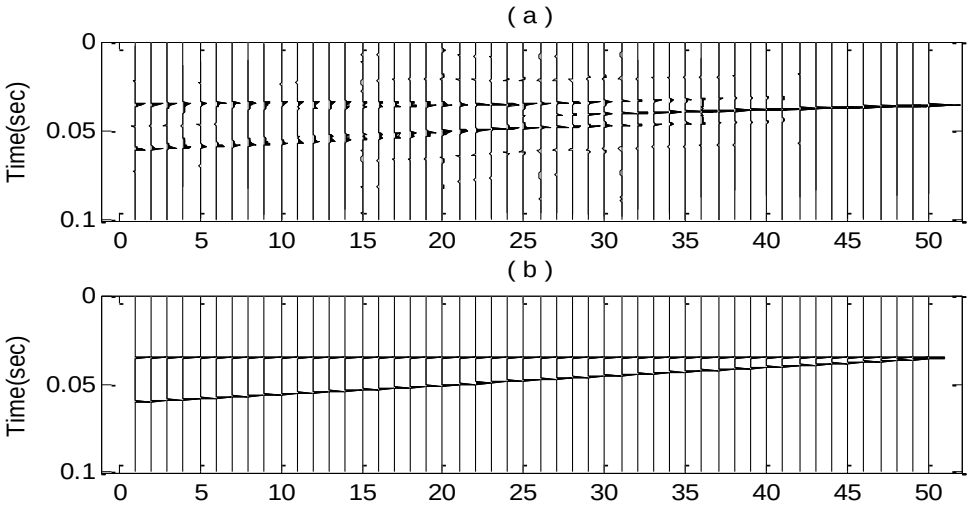

Figure 4.13: MPD method. (a) Inverted even wedge model; (b) True even spike pairs.

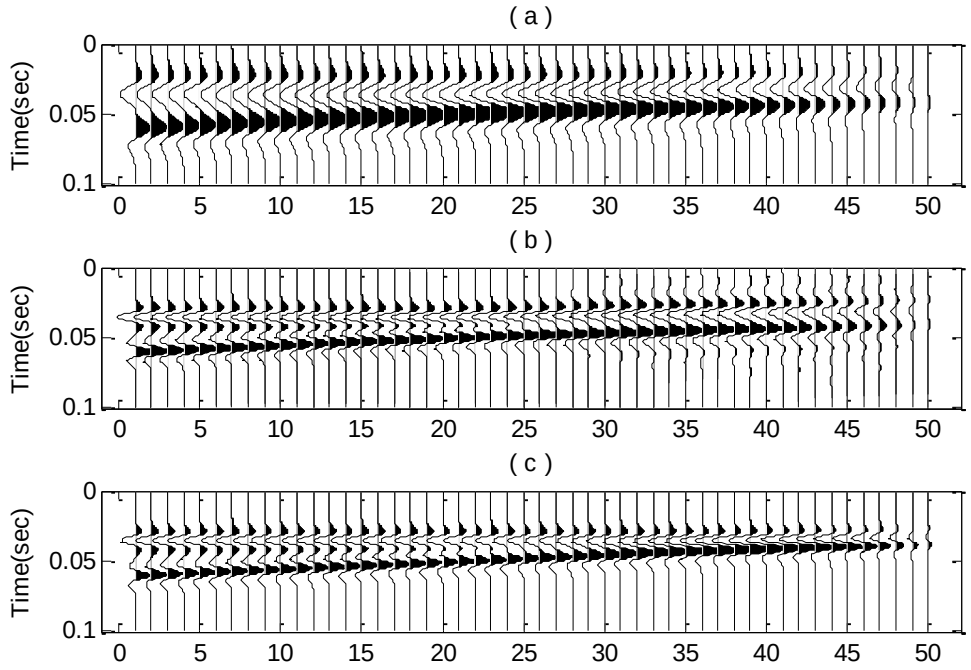

Figure 4.14: MPD method. (a) Seismic responses for odd wedge model (30Hz); (b) Spectrally extended responses for the odd wedge model (60Hz); (c) Seismic responses for odd wedge model (60Hz).

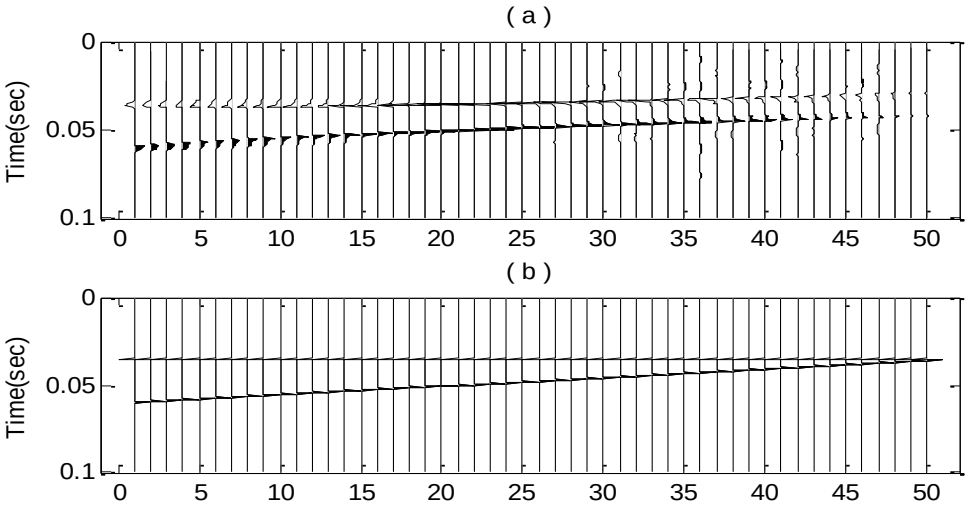

Figure 4.15: MPD method. (a) Inverted odd wedge model; (b) True odd spike pairs.

4.5 Real Data Examples

The AR algorithm based on matching pursuit will now be applied to that original migrated 2D seismic section (Figure 4.16). The resulting section for reflectivity from the AR algorithm is shown in Figure 4.18. The outputs have become much spikier than the original data, such that major layer interfaces are revealed clearer than before. The high resolution section produced by convolving a higher frequency Ricker wavelet is displayed in Figure 4.17. Although it is certain that some false events are inevitable to be produced in the inversion with this method, the results are still reasonable and the seismic resolution does have been improved. Observing the corresponding spectra (Figure 4.19) for the trace at the well location, the seismic spectral bandwidth has really been significantly extended by this approach.

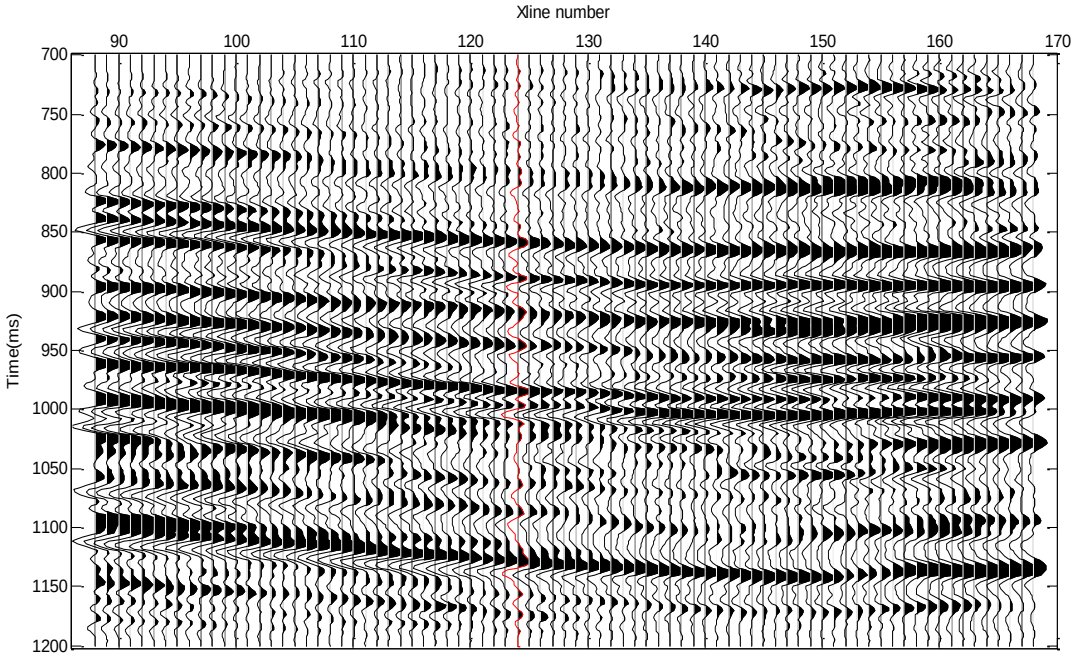

Figure 4.16: Original band-limited seismic section. The well location is near the trace denoted by red color.

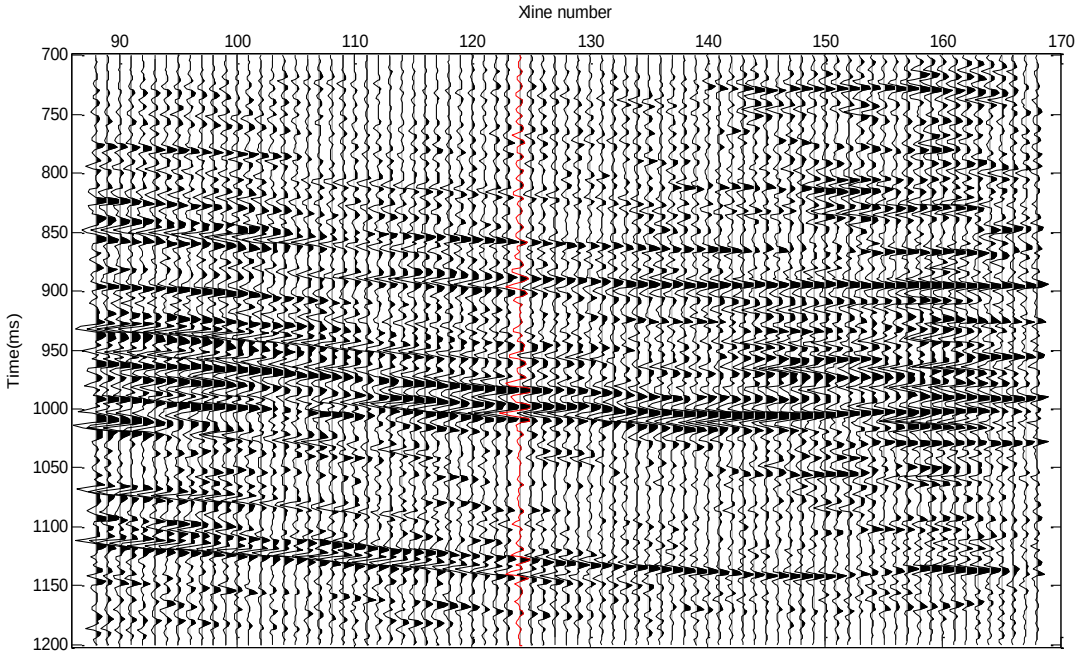

Figure 4.17: Resolution enhanced seismic section (bandwidth-extended) for MPD method.

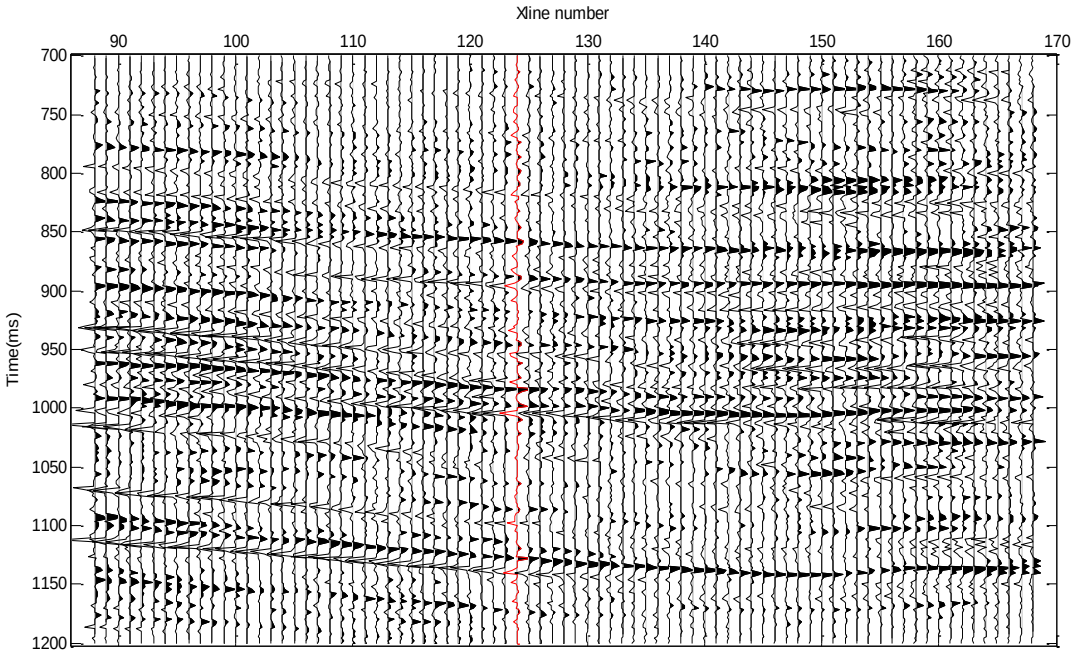

Figure 4.18: Inverted reflectivity section for MPD method.

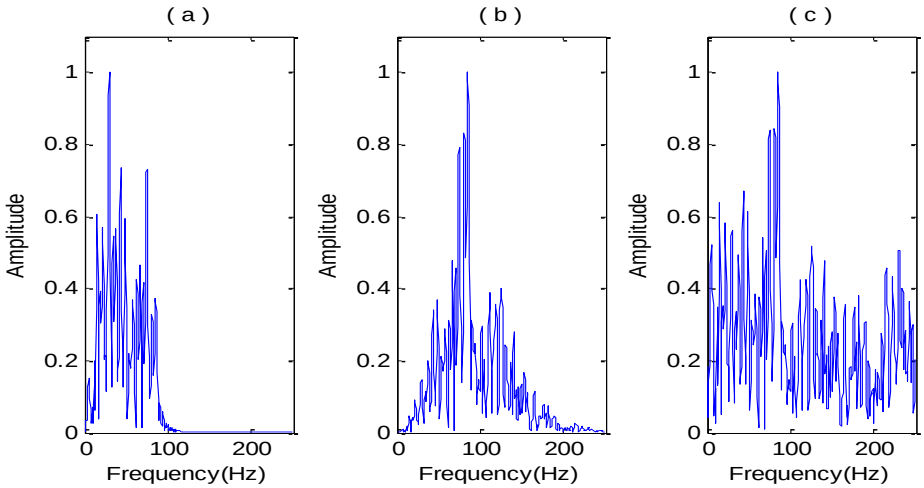

Figure 4.19: MPD method. (a) Spectrum of the original trace at well location; (b) Spectrum of the bandwidth-extended trace at well location; (c) Spectrum of the inverted reflectivity at well location.

4.6 Section Conclusion

Restricted to homogeneous blocky layers, seismograms can be reproduced by the collection of isolated delta functions convolving with embedded band-limited wavelets and therefore the reflectivity sequence could be considered broad-band. The fact that the corresponding reflectivity spectrum can be modeled as an autoregressive process provides the opportunity to predict the missing spectrum outside the available band. To avoid the instability problem encountered in the spectrum consisting of many sinusoids and additional noise, matching pursuit algorithm is employed as a more robust strategy to spectrally decompose the seismic data locally. This methodology has been successfully applied to a number of examples and it works acceptable on both synthetic and field data. The idea investigated in this section gives enlightenment for further research that modified versions of matching pursuit algorithm might have better performance and enormous potential in high resolution seismic interpretation.

Section II: Wiener Prediction on CWT Frequency Gathers

In Chapter 3, the seismic signal is spectrally transformed by Fourier analysis. Fourier transform reveals that any function can be represented as a superposition of a series of single sinusoids. However, when FT is employed, a window typically has to be fixed for analysis, so time and frequency resolution is thus defined by the window length. Therefore, the signal is decomposed by sinusoids regardless of how many local events are included in that window. In this way, isolated events far apart would be considered globally, which might make local information lost. In this section, a local spectral decomposition strategy, through the use of wavelet transform (WT), is utilized in capturing the seismic local information and global information simultaneously. We employ continuous wavelet transform (CWT) to perform a time-scale analysis for the seismic trace, which decomposes the band-limited signal into discrete sub-bands. Then the usable limited band information will be analyzed to model missing parts of the spectrum.

4.7 Continuous Wavelet Transform

4.7.1 Morlet Wavelets

In mathematics, a Morlet wavelet is defined as multiplying a complex exponential by a Gaussian window. A complex Morlet wavelet with the central frequency of 40Hz is displayed in Figure 4.20a. The real part (red solid) is a zero-phase wavelet, while the imaginary part (blue dash) has a 90 degree phase rotation to that real part.

The amplitude spectrum of the complex wavelet is a Gaussian curve centered at its dominant frequency (Figure 4.20b), which corresponds to the modulation occurring in

time domain. Mathematically, Morlet wavelets can be generally expressed as:

$$\psi(t) = \frac{1}{\sqrt{\sigma}} e^{-\frac{t^2}{2\sigma^2}} \cdot e^{i\omega t} \tag{4.8}$$

where $\omega = 2\pi f_c$ and f_c is the wavelet dominant frequency; σ is the wavelet scale and defined as the reciprocal of the central frequency: $\sigma = 1/f_c$. A large scale indicates the wavelet has longer time duration and vice versa. Higher central frequency means a broader bandwidth in frequency domain.

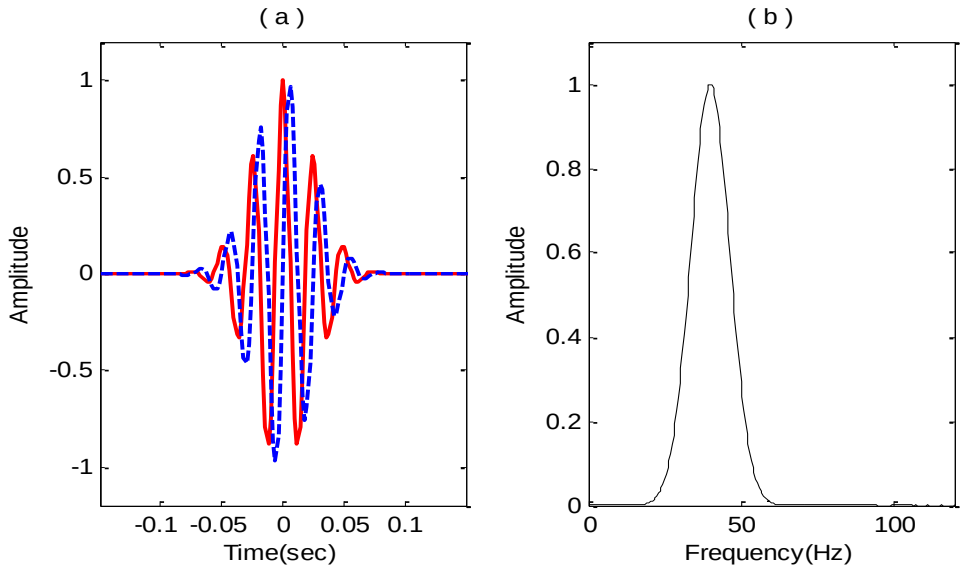

Figure 4.20: (a) Complex Morlet wavelet; (b) Amplitude spectrum of the Morlet wavelet.

4.7.2 Basic Properties for CWT

Continuous wavelet transform of a time series $s(t)$ is defined as convolution of $s(t)$ with a series of Morlet wavelets $\psi(t)$ with varying scales σ:

$$W(\tau,\sigma) = \int_{-\infty}^{\infty} s(t) \cdot \psi^*(t-\tau,\sigma)\, dt \tag{4.9}$$

where τ is a translated time for the wavelet of scale σ and $W(\tau,\sigma)$ is thus the cross-correlation coefficient between the signal and the Morlet wavelet of scale σ at the translated time τ. Consequently, at each time point, the signal is cross- correlated

with a series of Morlet wavelets with varying central frequencies. Those CWT coefficients thus reveal similarity degrees between the analyzing wavelets and the signal segment around that time point. Therefore, a 2D time-frequency analysis plane can be displayed for a seismic trace (Figure 4.21).

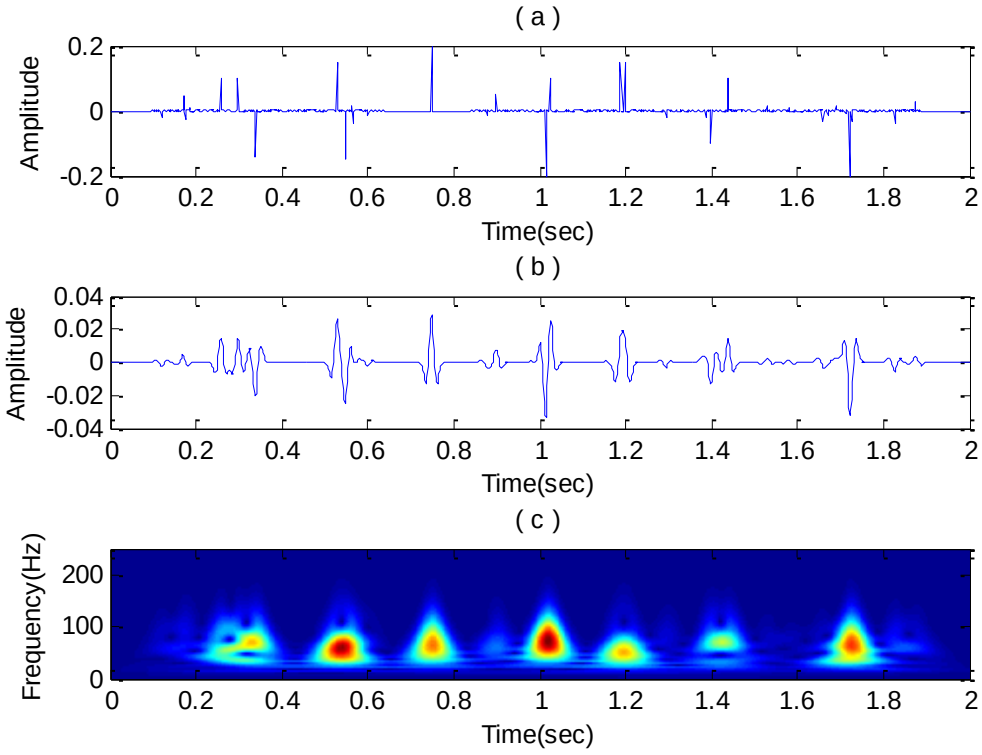

Figure 4.21: (a) Original reflectivity series; (b) Synthetic trace generated by 30Hz Ricker wavelet; (c) CWT frequency gather of the trace.

The dominant frequency of the synthetic trace is around 30Hz where those relatively independent spectra are mainly concentrated. On the high frequency end, we could observe some spiky elements which are corresponding to those closely spaced events, while a number of ribbons are extending in the direction of time axis between the primary spectra on the low frequency end. This implies that CWT has a better time resolution with higher frequencies (small scales) Morlet wavelets and a better

frequency resolution with lower frequencies (large scales) ones. In other words, time resolution is more important in the high frequency end and frequency resolution should be paid more attention in the low frequency spectrum.

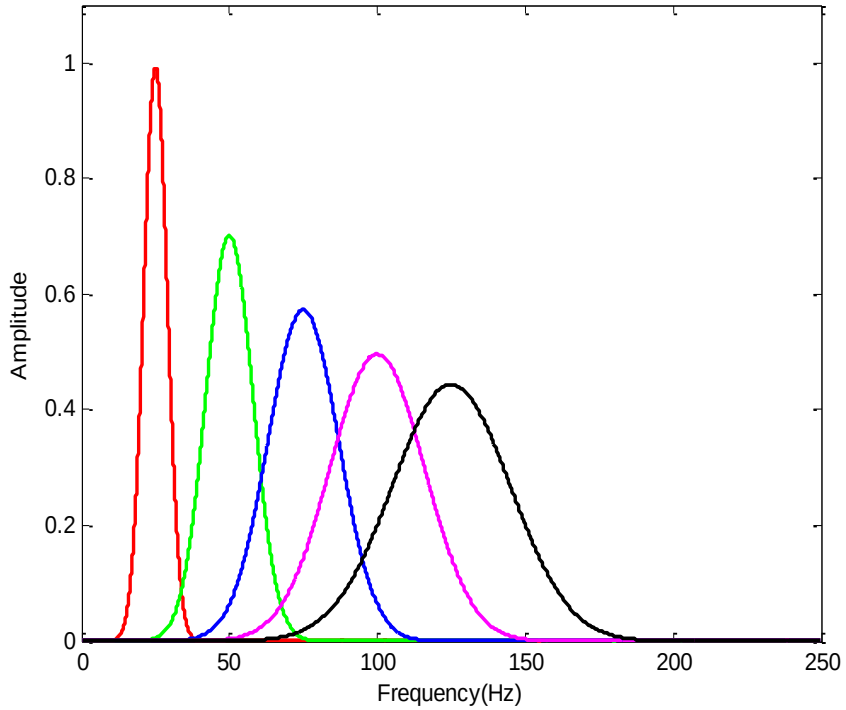

Figure 4.22: Amplitude spectra for Morlet wavelets of varying central frequencies: 25Hz, 50Hz, 75Hz, 100Hz, and 125Hz.

4.7.3 Band-pass Filters

From another point of view, Morlet wavelets used for CWT can be considered as a series of band-pass filters, since the real part of the complex Morlet wavelet is zero-phase. Figure 4.22 displays the amplitude spectra of five Morlet wavelets with different central frequencies. There is a chance for them to obtain a flat spectrum if weighted summed. Consequently, the original seismic trace can be decomposed by the analyzing wavelets into discrete sub-bands which will be further analyzed to compute both higher and lower frequency spectral components. Therefore, for this

methodology, only the real Morlet wavelets will be employed to perform spectral decomposition for the seismic data which is shown in Figure 4.23. A limited number of sub-bands decomposed from the original seismic trace (Figure 4.21b) are listed on the right column, and their corresponding analyzing wavelets are displayed on the left. These sub-bands are the available information for predicting both the higher and lower frequencies. CWT is in theory infinitely redundant, meaning that one could use unlimited Morlet wavelets to analyze the band-limited signal, which might stabilize the predictions to some degree. However, 100-200 scales per octave are already sufficient to guarantee a stable calculation.

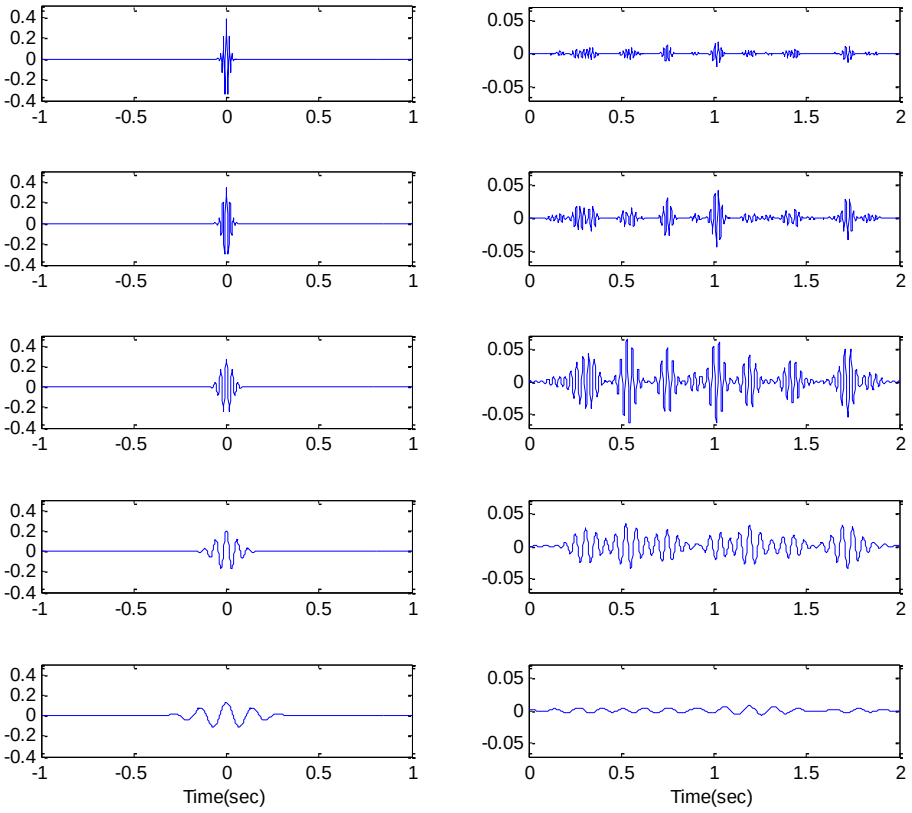

Figure 4.23: Sub-bands of the band-limited synthetic trace filtered by real Morlet wavelets.

4.8 Calculation for Predicted Spectral Components

The CWT transforms a one-dimensional signal into a 2D time-frequency analysis plane, which provides the opportunity to extend missing spectral information depending on spectra redundancy. Consequently, there are multiple wavelet transform coefficients at different frequencies (or scales) and times to make a prediction at another frequencies (or scales). Theoretically, utilizing CWT spectra at multiple time points would give better stability in the predictions.

4.8.1 Multichannel Wiener Predictive Operator

A sampled seismic trace is a typical example of single-channel digital series, while a number of adjacent traces on a seismic section could be regarded as multichannel series. Similarly, on the CWT time-frequency (time-scale) analysis plane, a spectra coefficients sequence at each time point is considered as a single-channel series and two or more such spectra sequences around that time point thus constitute the multichannel spectra series. Moreover, transition from single-channel to multichannel processing systems requires that the scalar-valued weighting coefficients occurring in the single-channel filter should be modified to be matrix-valued weighting coefficients. Treitel (1970) discussed the general case of k input channels and l output channels for multichannel Wiener filter. For the purpose of this thesis, we specify only one output channel and k input channels for computing coefficients of the multichannel operators. Those multichannel operators have a constant dimension of $q \times k$. So there should be $q \times k$ unknown coefficients to be solved in the prediction system. The design criterion for the multichannel predictive filters is also based on the least-squares principle so that those predicted CWT coefficients will be

overdetermined. Specifically, if the number of available sub-bands is p, there will be $p-q$ wavelet coefficients in the desired output channel so the number $p-q$ is supposed to be larger than $q \times k$ in order for least-squares solutions.

$$\begin{bmatrix} F_{11} & F_{12} & F_{13} & \bullet & \bullet & F_{1k} \\ F_{21} & F_{22} & F_{23} & \bullet & \bullet & F_{2k} \\ F_{31} & F_{32} & F_{33} & \bullet & \bullet & F_{3k} \\ \bullet & \bullet & \bullet & \bullet & & \bullet \\ \bullet & \bullet & \bullet & & \bullet & \bullet \\ \bullet & \bullet & \bullet & & & \bullet \\ F_{(p-q)\times 1} & F_{(p-q)\times 2} & F_{(p-q)\times 3} & \bullet & \bullet & F_{(p-q)\times k} \end{bmatrix} \begin{bmatrix} X_1 \\ X_2 \\ X_3 \\ \bullet \\ \bullet \\ \bullet \\ X_k \end{bmatrix} = \begin{bmatrix} d_1 \\ d_2 \\ d_3 \\ \bullet \\ \bullet \\ \bullet \\ d_{p-q} \end{bmatrix} \tag{4.10}$$

The equation system (Eq.4.10) provides an equation set of generalized form with $p-q$ equations whereby the $q \times k$ unknown coefficients of multichannel operators will be solved. X_s and F_s are column and row vectors both with a length of q.

4.8.2 Reconstruction of Spectrally Extended Data

Since analyzing wavelets used in CWT can be considered as a series of band-pass filters, it is possible to reconstruct both the original and spectrally extended time series by adding together real part of the wavelet transforms over all sub-bands (Figure 4.23). Theoretically, time sampling rate and a fractional constant accounting for varying wavelet scales are required to compute compatible spectrally extrapolated outputs. A factor calculated from the reconstruction of a delta function from its wavelet transform and the scale of the mother Morlet wavelet are also needed to remove the energy scaling occurring in the predictions. However, energy density

adjustment for discrete sub-bands could be made in a practical way so that extrapolated frequencies (or scales) could produce a better looking shape for the amplitude spectrum.

4.8.3 Limitation of Spectral Extrapolation by CWT

Although multiple spectra series are involved for better stability in the calculations, they also have their downside, as has already been demonstrated by a number of synthetic cases. For an isolated event, the multichannel operators just need to recognize the variation tendency of the spectra from a single event. In the case of many reflections around a time point, however, it would be difficult for those operators to pick up the superposition of so many variations occurring in the spectra. So this spectral extension method might not work well for data with high complexity. Since the extrapolated spectral components are computed with least-squares, different extrapolations will give different results in the time domain. In fact, the extrapolation is limited in how far out it can reach because deviated predictions may lead to large cumulative error in further calculations. Moreover, wavelet correction performed in this approach can only be carried out in a practical way, as Morlet wavelets will have differing degrees of Gaussian decay at different frequencies (or scales). Nevertheless, this method does have produced seismic sections that are resolution enhanced.

4.9 Wedge Model Tests

We have tested this spectral extension algorithm on wedge models to examine its performance. A 30Hz Ricker wavelet is used to model the low frequency seismic responses for both even and odd spike pairs. Observed from the low frequency

responses for the even wedge (Figure 4.24a), the spike pairs are fully resolved at Trace 26. Applying spectral extension, the top and bottom reflectors of the wedge can be resolved down to Trace 34 (Figure 4.24b), which is comparable to the resolving capability of higher frequency synthetics generated by a 42Hz wavelet (Figure 4.24c).

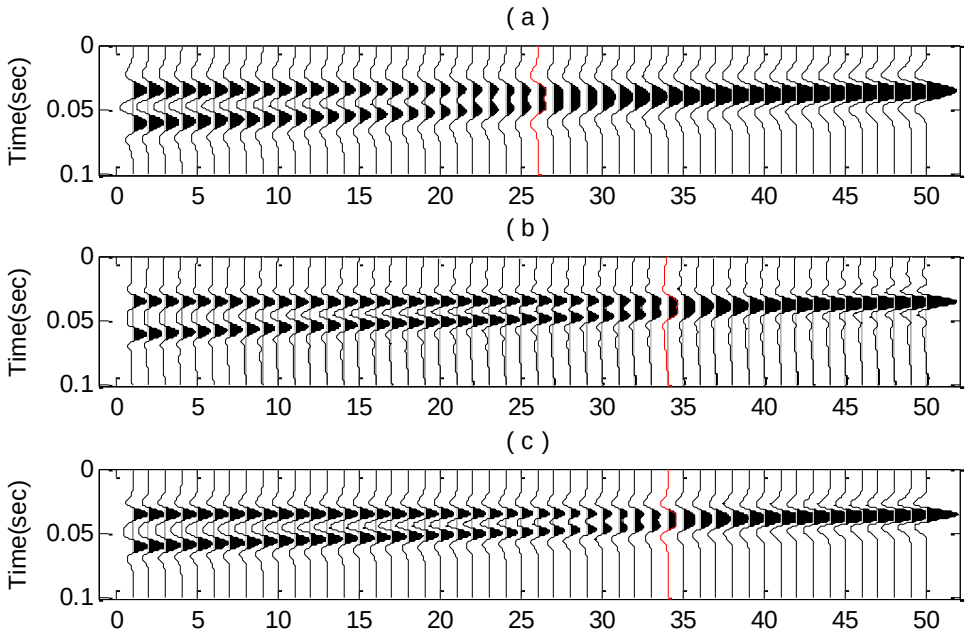

Figure 4.24: CWT method for even wedge model. (a) Low frequency seismic responses; (b) Spectral extension of the original seismic responses; (c) High frequency seismic responses.

For this thesis, Ricker's criterion is used to determine if the thin beds are resolved or not. However, it is not the only criterion widely employed in industry. A brief introduction for three kinds of criteria regarding resolution is thus given below:

1) Rayleigh criterion: Two closely spaced wavelets with same polarity can be resolved when the time separation is large or at least equal to half the apparent period of the wavelet.

2) Ricker criterion: Two closely spaced wavelets with same polarity can be resolved when the time separation is larger or at least equal to the distance between the two points with maximum gradient on the flanks of the wavelet main lobe.

3) Widess criterion: When the time separation for two closely spaced wavelets with opposite polarity is less than 1/4 of the wavelet apparent period (tuning thickness), the composite waveform could be approximated as the first derivative of the temporal wavelet. The time interval between the peak and trough of the waveform would be constant so the time thickness cannot be interpreted as the true layer thickness. Even so, an approximate positive correlation can be found between the amplitude of the waveform and the true layer thickness.

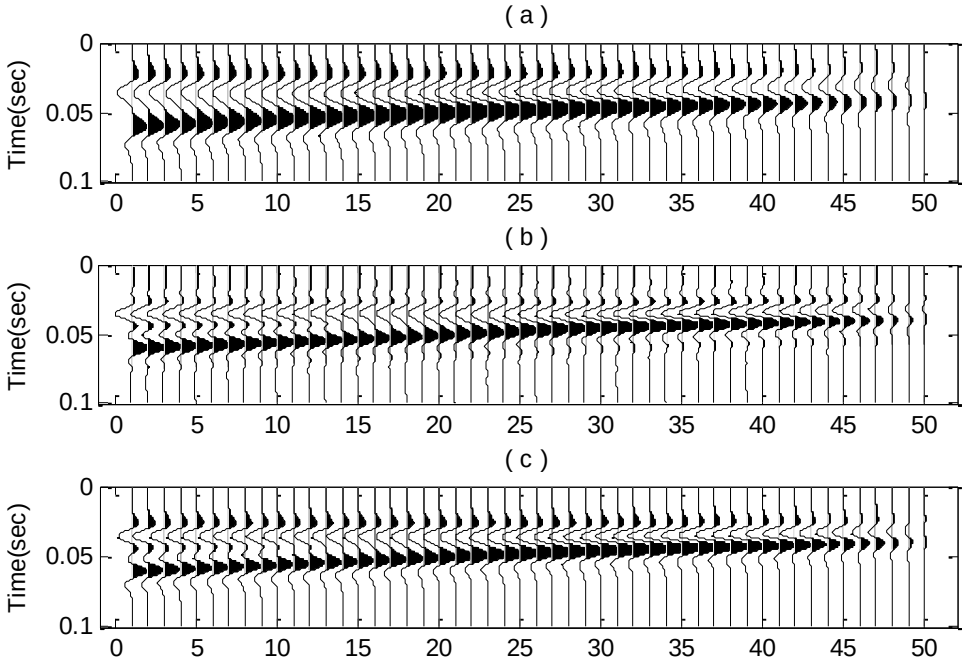

Figure 4.25: CWT method for odd wedge model. (a) Low frequency seismic responses; (b) Spectral extension of the original seismic responses; (c) High frequency seismic responses.

This spectral extension method is also run on low frequency responses (Figure 4.25a) for the odd wedge. The tuning thickness for the low frequency synthetics is about 13ms which is denoted by the black line with the time-amplitude curve (Figure 4.26).

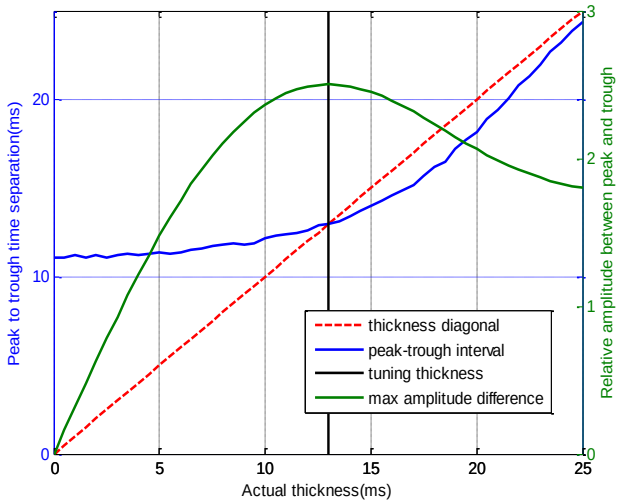

Figure 4.26: Time-amplitude curve for the low frequency synthetics (30Hz).

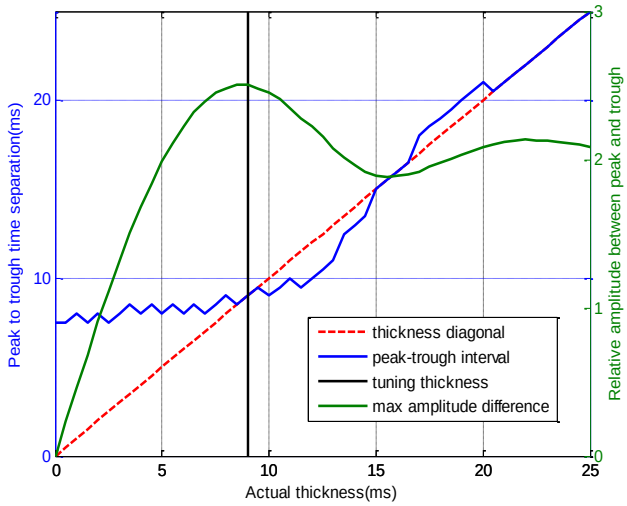

Figure 4.27: Time-amplitude curve for the spectrally extended synthetics.

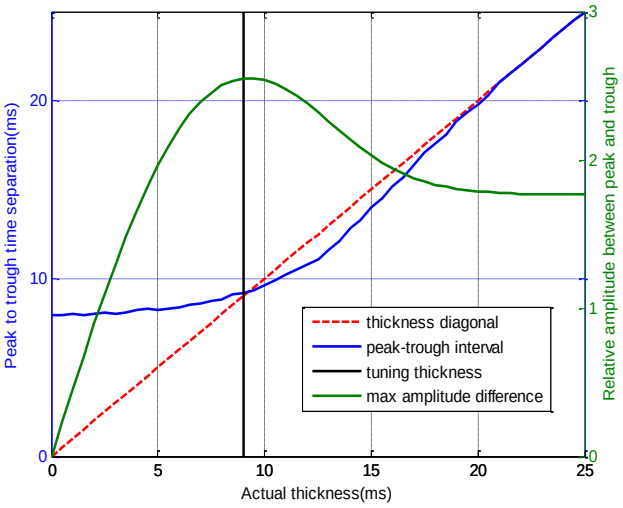

Figure 4.28: Time-amplitude curve for the high frequency synthetics (42Hz).

Through spectral extension, the maximum amplitude has been approached to a thinner bed (Figure 4.27). The spectrally broadened model responses (Figure 4.25b) thus have a tuning thickness about 9ms, which is comparable to the high frequency synthetics (Figure 4.25c). The validity of this spectral extension method has been successfully demonstrated on wedge models in which significant improvements in resolution have been achieved. It can extend the original bandwidth to a broader bandwidth that matches the targeted bandwidth and ultimately increases the thin bed detectability.

4.10 Real Data Examples

Applying this CWT method to that 2D seismic section from Blackfoot dataset, the comparison of the before-and-after bandwidth extensions is shown in Figure 4.29 and Figure 4.30. The usable input frequency content is approximately 20-75Hz (Figure 4.31a), while the output frequency content is about 10-90Hz (Figure 4.31b). With this broader spectrum, we can observe some thin layers that cannot be resolved in the

original section have been revealed. More details have come to light with the spectral extension. Frankly, the performance of this method on real data might not be that good. The spectrum it can extend is quite limited on the Blackfoot dataset. This is because the estimated wavelet used is determined statistically within a picked window, thus the same wavelet correction has to be performed for all time points on the trace. The wavelet is assumed to be constant with time and space in the target zone. However, the actual waveforms as well as signal-to-noise ratio would vary along the trace. Consequently, the wavelet overprint is normalized in a fuzzy way. Different parts on the trace might have different robustness in the calculations. So if some local calculations go wrong, they would affect the whole trace so the extrapolations have to be stopped. However, this spectral extension method with CWT does produce a real seismic section that looks better and the result is reasonable.

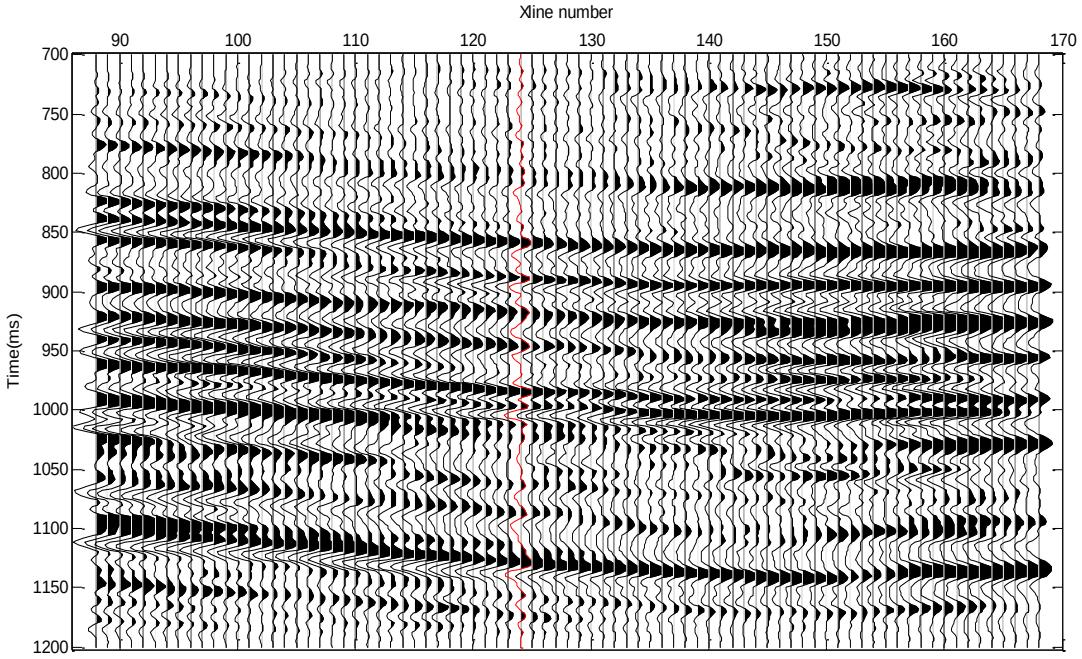

Figure 4.29: Original band-limited seismic section. The well location is near the trace denoted by red color.

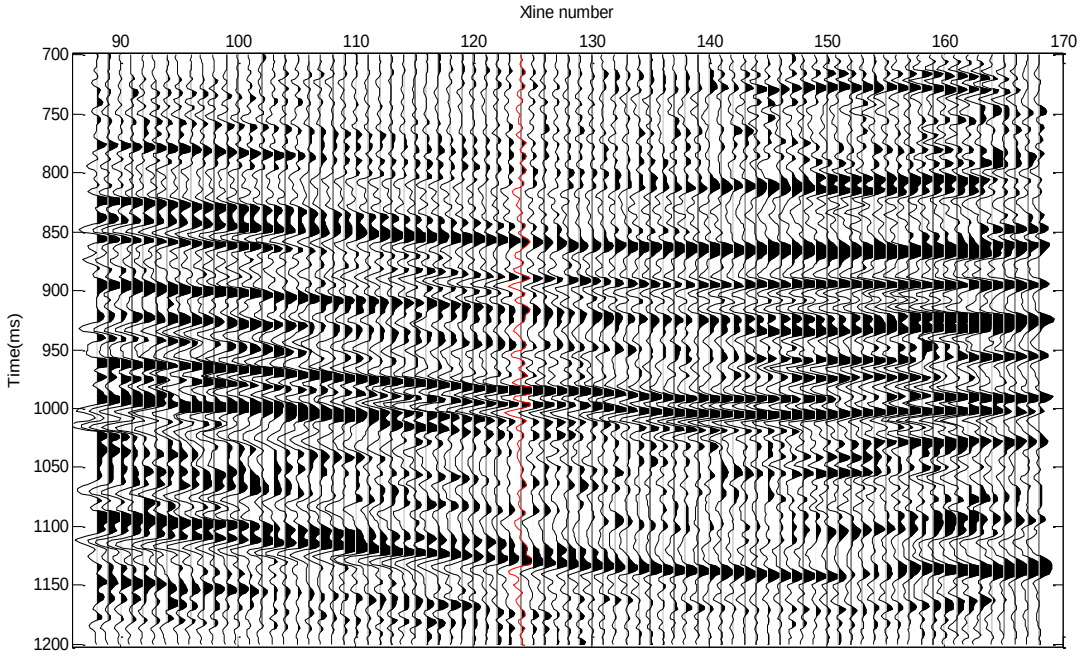

Figure 4.30: Resolution enhanced seismic section (bandwidth-extended) for CWT method.

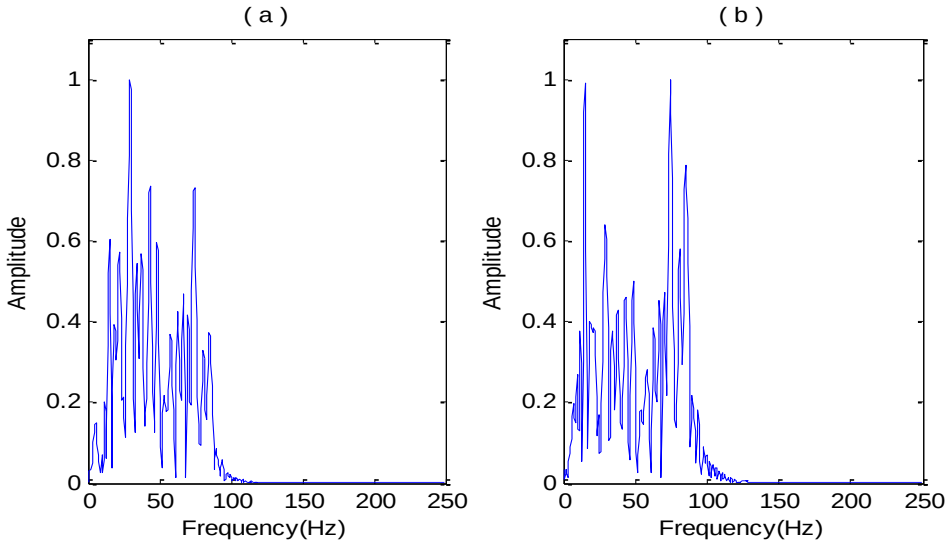

Figure 4.31: CWT method. (a) Spectrum of the original trace at well location;
(b) Spectrum of the bandwidth-extended trace at well location.

4.11 Section Conclusion

Spectral bandwidth extension using predicted high frequency sub-bands and low frequency sub-bands calculated with continuous wavelet transform has been demonstrated to have potential for seismic resolution enhancement. Although the very high and low frequencies have been filtered out in the original seismic, the missing spectrum can be extrapolated by multichannel predictive operators computed from the available fundamental frequencies and added back, which would effectively extend the seismic bandwidth and improve the overall resolution of the seismic data.

Wedge models with both even spike pairs and odd spike pairs have been examined to prove that this technique can extract the very thin beds originally concealed by the band-limited wavelet and could thus resolve other similar geological features.

This methodology is limited in how far out those multichannel operators can reach; the predicted sub-bands can only extend upward or downward within 0.5 to 2 octaves. The real data examples presented have further shown the benefits of this method. It can be expected that those subtle features which might not be resolved in the original seismic data have the potential to come to light.

Chapter 5

Sparse Spike Inversion for Reflectivity Sequence

In reflection seismology, artificial seismic sources such as dynamites or vibroseis are generally utilized to stimulate explosions near the surface. Precise devices arranged in certain acquisition systems receive the energy and record seismograms at the surface. The raw recorded data are subsequently processed through a series of procedures to finally produce seismic sections which could be regarded as representations for true subsurface geologic structures. However, underground conditions are typically complicated and noise contamination is also inevitable. Although much effort in the acquisition and processing stages has been devoted in order to reduce disturbance, the resulting images could never reflect the exactly true structures. Nevertheless, a post-processing seismogram could be thought of as convolution of a reflectivity sequence representing sparse structured subsurface layers with embedded wavelets. In fact, this convolutional model does work well and has prevailed in industry for many decades.

5.1 Forward Convolutional Model

The previous convolutional model is described by the equation of convolutional operation in an integral form (Eq.1.1 and Eq. 1.2). As a matter of fact, convolution can also be represented as a direct multiplication (Figure 5.1) between a wavelet matrix and a reflectivity vector which is essentially the same as integration.

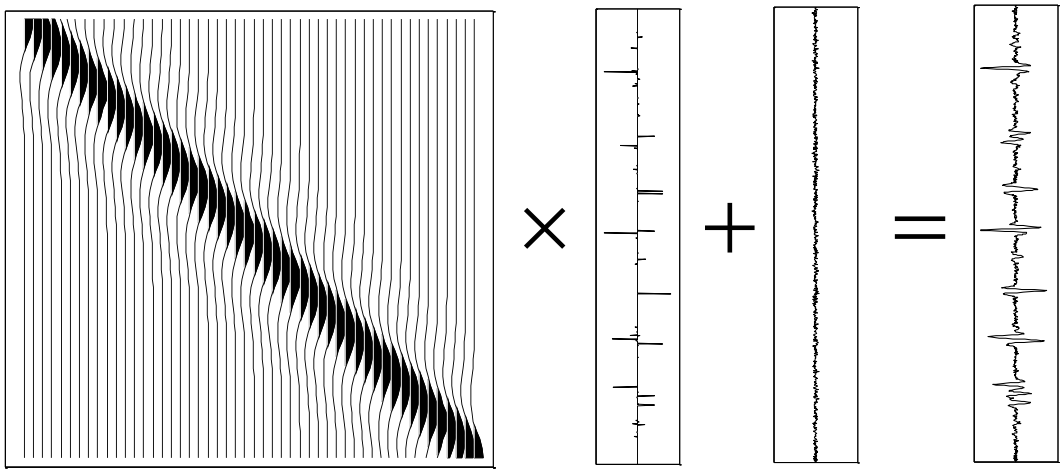

Figure 5.1: Matrix multiplication for convolutional model.

Mathematically, the forward problem can be represented with explicit linear equation:

$$Gm + n = d \tag{5.1}$$

For the convolutional model, G will be a $N \times N$ wavelet kernel matrix, where N is the vector length of the data. Each column of the G matrix only contains a single wavelet vector, and the wavelet is shifted with a sampling interval from column to column (Figure 5.1). m and d represent the reflectivity series and observed seismogram, respectively. Moreover, n is the random noise. What we typically will have are the recorded seismograms d and estimated wavelets G extracted from corresponding surface seismic data. From a purely mathematical perspective, the direct solution m could be calculated by inverting the wavelet kernel matrix and make it left multiply both sides of the equation $Gm = d$, which is shown in Eq. 5.2:

$$m = G^{-1}d \tag{5.2}$$

However, the matter is not that simple and we cannot take it for granted.

5.2 Ill-conditioned Inverse Matrix

The inverse of a square matrix G is denoted by G^{-1}, which can be calculated as:

$$G^{-1} = \frac{1}{\det(G)} Adj(G) \tag{5.3}$$

The numerator is the adjoint matrix of G and the denominator is the determinant of G. Unfortunately, the wavelet kernel matrix G has a determinant of nearly zero, so its inverse would be extremely large. To further character this inverse matrix, its eigenvalues are calculated and there is a significant difference among them (Figure 5.2). The order of magnitude of the first two eigenvalues is 18, while the majority of the rest have orders of magnitude less than 5. Such a big difference in eigenvalues will lead to serious instability problem in the solution. In the standpoint of numerical analysis, the ratio of the largest eigenvalue to the smallest eigenvalue of a matrix is defined as condition number, which is used to measure how sensitive a solution is to changes or errors in the data, that is, how much error in the solution results from an error in the data. Since the order of magnitude for the condition number of the inverse matrix has reached 21, the inverse problem with such a huge condition number is definitely considered as ill-conditioned, which means the solution for inverted reflectivity series will be extremely noise sensitive.

Physically, the shifted seismic wavelets comprising the kernel matrix G typically just have spectral components within a limited band. Frequencies outsides the bandwidth are almost zeros. But the reflectivity to be inverted should be broad-band requiring non-zero spectral components outside the limited band. Thus, if a solution exists, deconvolution operator has to attempt to boost the absent frequencies to some finite values, which is virtually impossible to achieve. This corresponds to another

serious problem in inversion which is non-uniqueness. Therefore, direct inversion of the wavelet kernel matrix can never be the correct way in obtaining a broad-band reflectivity sequence.

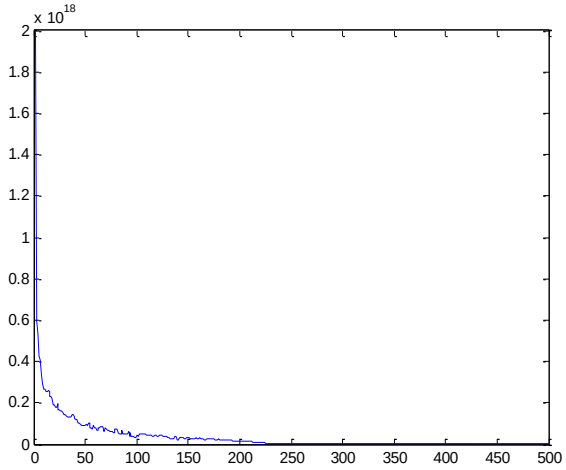

Figure 5.2: Eigenvalues of the inverse matrix G^{-1}.

5.3 Least-squares Approach for Deconvolution

The discrete convolutional process can be represented as:

$$d_k = \sum_j w_j m_{k-j}, \qquad k = 1, n_y \tag{5.4}$$

where m_k, $k = 1, n_m$ is the reflectivity series (model parameters vector), d_k, $k = 1, n_d$ is the observed seismogram (data vector), and w_k, $k = 1, n_w$ is the source wavelet. The basic goal for seismic deconvolution is just to recover the vector m_k in model space. Ideally, the desired solution should be the one which can generate the predicted data perfectly matching the observations, that is, data misfit is zero. However, the true reflectivity sequence could never be obtained in the real world due to noise disturbance and wavelet inaccuracy. So a practical solution is to find an estimated vector $\hat{m}_k$ that gives a minimal residual vector r_k:

$$r_k = d_k - \sum_j w_j \hat{m}_{k-j}, \qquad k = 1, n_y \tag{5.5}$$

Therefore, in a least-squares error sense, the objective is just to minimize the summation of the residuals for all time points:

$$J_m = \sum_k \frac{1}{2}\left(\frac{r_k}{\sigma_k}\right)^2 \tag{5.6}$$

Theoretically, data misfit for each time should be weighted by the reciprocal of the standard deviation of that observation. In other words, more emphasis should be put on the points where the data are more accurate. In this chapter, however, for simplicity we assume the standard error σ_n is constant for all observations.

Generally, maximization or minimization of a function is achieved by equating the gradient of the function with respect to related variables to zero. In seismic inversion for reflectivity series, independent variables are the reflection coefficients m_l for each time point. Derivation is presented in Eq.5.7:

$$\begin{aligned}
\frac{\partial J_m}{\partial m_l} &= \frac{\partial \sum_k \frac{1}{2}\left(\frac{r_k}{\sigma_n}\right)^2}{\partial m_l} \\
&= \frac{1}{2\sigma_n^2}\sum_k \frac{\partial\left(d_k - \sum_j w_j \hat{m}_{k-j}\right)^2}{\partial m_l} \\
&= \frac{1}{\sigma_n^2}\sum_k \left(d_k - \sum_j w_j \hat{m}_{k-j}\right)\cdot\left(-w_{k-l}\right)
\end{aligned} \tag{5.7}$$

and,

$$\sum_k \left(d_k - \sum_j w_j \hat{m}_{k-j}\right) w_{k-l} = 0 \tag{5.8}$$

Hence,

$$\sum_k \sum_j w_{k-l} w_j \hat{m}_{k-j} = \sum_k w_{k-l} d_k \tag{5.9}$$

Also, Eq. 5.9 can be written in a matrix form as the time index l slides:

$$Rm = g \tag{5.10}$$

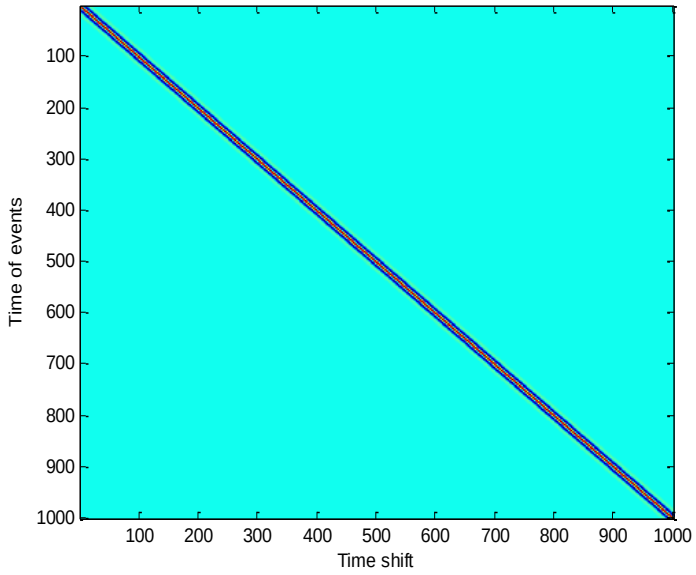

Figure 5.3: Autocorrelation coefficients matrix R.

The matrix R (Figure 5.3) is comprised of wavelet autocorrelation coefficients where the wavelet is sliding along the data vector from the first time point to the end. Each row of the autocorrelation matrix corresponds to the location of data points, while each column denotes time lags in autocorrelation. The vector g on the right side (Eq.5.10) is a column representing cross-correlation coefficients between the data and the wavelet. In accordance with the wavelet kernel matrix G in Eq.5.1, the determinant of the R matrix is also almost zero. Mathematically, the spectrum of autocorrelation should be the square of the original spectrum, so that spectral components outside the limited bandwidth are still zero. The inverse matrix of R will be ill-conditioned. There is a wide distribution among eigenvalues of the inverse matrix R^{-1}, thus the model parameters m directly inverted are quite unstable.

5.4 Least-squares Optimization with L1-Norm Regularization

The non-uniqueness issue in seismic deconvolution is partly brought by noise disturbance occurring in the data. The error (data misfit) between observation and predicted data generated by forward modeling can never be eliminated. For minimizing the error, the inversion program might try to reach a solution consisting of a large number of closely spaced odd spike pairs so as to arbitrary fit small waveforms in the data. However, a minimal error does not necessarily mean the best solution. In fact, true earth reflectivity function is assumed to be sparse structured when the seismogram is dominated by a few strong reflections where a minimum of structural variation is desired. A sparse solution can be found by minimizing a specific norm of the model, which in this case is accomplished by regularizing the objective function (Eq.5.6) with an l1-norm penalty term. In general, the l1-norm regularized objective function can be written in a form as:

$$\min\left[\|d-Gm\|_2+\lambda\|m\|_1\right] \tag{5.11}$$

where λ is the penalty factor that balances the two terms: l2-norm of the observation error $d-Gm$ and l1-norm of the solution m.

5.4.1 Huber Criterion

Huber's criterion is a useful method for robust regression. It defines a piecewise function (Huber, 1981):

$$\rho(u)=\begin{cases} u^2/2 & |u|\le a \\ a|u|-a^2/2 & |u|>a \end{cases} \tag{5.12}$$

and the influence function of ρ, which is the first-order derivative shown below:

$$\psi(u)=\begin{cases} u & |u|\le a \\ a\ sign & |u|>a \end{cases} \tag{5.13}$$

In this method, the regularization term is just derived using Huber's criterion, so the modified objective function will be:

$$J_m = \sum_k \frac{1}{2}\left(\frac{r_k}{\sigma_n}\right)^2 + \sum_i \rho\left(\frac{m_i}{\sigma_m}\right) \tag{5.14}$$

where σ_m is the standard deviation of reflection coefficients. Similarly, minimization of this objective function is achieved by equating the first derivation to zero. The derivation is presented below where small enough a is postulated:

$$\begin{aligned}
\frac{\partial J_m}{\partial m_l} &= \frac{\partial \sum_k \frac{1}{2\sigma_n^2}\left(d_k - \sum_j w_j \hat{m}_{k-j}\right)^2}{\partial m_l} + \frac{\partial \sum_i \left(a\left|\frac{m_i}{\sigma_m}\right| - \frac{a^2}{2}\right)}{\partial m_l} \\
&= \frac{1}{\sigma_n^2}\sum_k \left(d_k - \sum_j w_j \hat{m}_{k-j}\right)\cdot\left(-w_{k-l}\right) + \frac{a}{\sigma_m} sign\left(m_l\right) \\
&= \frac{1}{\sigma_n^2}\sum_k \left(\sum_j w_j \hat{m}_{k-j} - d_k\right) w_{k-l} + \frac{a}{\sigma_m}\cdot\frac{1}{|m_l|} m_l \\
&= 0
\end{aligned} \tag{5.15}$$

Hence,

$$\sum_k \sum_j \left(w_j \hat{m}_{k-j} - d_k\right) w_{k-l} + \frac{a\sigma_n^2}{\sigma_m}\cdot\frac{1}{|m_l|} m_l = 0 \tag{5.16}$$

Finally, the minimization of the modified objective function J_m leads to the following equation:

$$\sum_k \sum_j w_{k-l} w_j \hat{m}_{k-j} + \frac{a\sigma_n^2}{\sigma_m}\cdot\frac{1}{|m_l|} m_l = \sum_k \sum_j w_{k-l} d_k \tag{5.17}$$

Eq.5.17 demonstrates the calculations for the case where the time shift is l. Because time is sliding from the beginning to the end of the whole trace, a matrix form for this system of normal equations can be obtained:

$$(R + \mu Q)m = g \tag{5.18}$$

where R is still the wavelet autocorrelation coefficients matrix as in Figure 5.3, μ can be thought as the penalty factor λ in Eq.5.11, and Q is a diagonal matrix in which those diagonal elements are reciprocals of absolute values of the reflection coefficients.

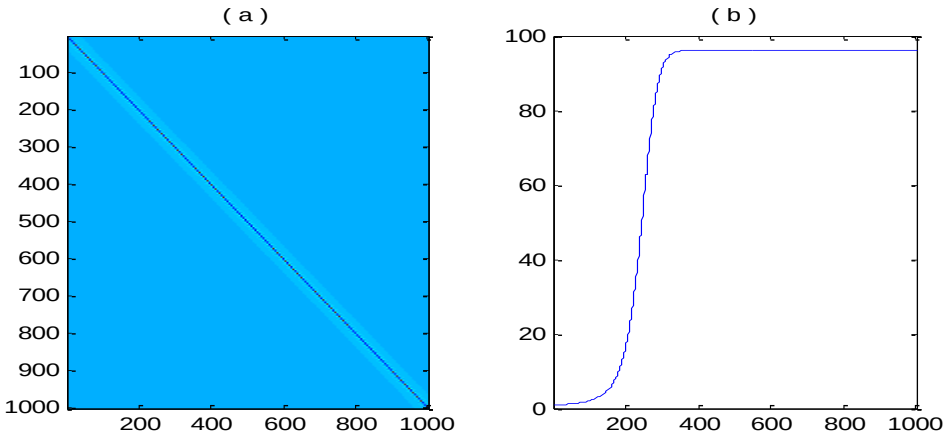

Figure 5.4: (a) Inverse of the regularized matrix; (b) Eigenvalues of the inverse matrix.

The introduction of Huber's criterion as a regularization term is equivalent to adding a small perturbation to the diagonal of the R matrix (Figure 5.3), which could stabilizes the inverse problem. This is very similar to prewhitening, which is adding a constant to the zero lag of the autocorrelation function. From the physical aspect, prewhitening is accomplished by adding purely random noise to the wavelet, which means spectral components outside the original limited bandwidth would be raised up to some positive level. Ideally, all lags of the wavelet autocorrelation should be invariant, except the zero lag where there is a constant added in. Figure 5.4a displays the inverse of the modified kernel matrix in which the elements have become finite and reasonable. Also, the condition number of this inverse matrix is less than 100 because there is only a small distribution range for those eigenvalues (Figure 5.4b).

Moreover, as seen from Eq.5.12, as long as the parameter a is small compared with

the independent model parameter, the modified objective function would behave as l1-norm regularization (Eq.5.11), which guarantees that the inverted reflectivity is constrained to be sparse. The fact that an l1-norm favors a sparse structure in the solution can be demonstrated by the example where two vectors with same l2-norm might have different l1-norms, and the one with smaller l1-norm will have a sparser structure than that with larger l1-norm. As a matter of fact, the objective function utilized in this method is neither invented nor imagined, but is derived from genuine mathematical laws.

5.4.2 Bayes' Theorem

Bayes' theorem, named after Thomas Bayes (1701-1761) who first suggested using the theorem to update beliefs, plays an important role in mathematical operation of conditional probabilities. It biases the degree of belief in an event based on given evidence. Mathematically, Bayes' theorem reveals the relationship between the probabilities of two events A and B, and also the conditional probabilities of A given B and B given A:

$$P(A \mid B) = \frac{P(B \mid A)P(A)}{P(B)} \tag{5.19}$$

Specifically, in seismic reflectivity inversion, the model parameter m and observation data d can thus be considered as two related events, A and B. Using Huber criterion, the reflectivity series is assumed to be exponentially distributed, which provides a prior distribution with a long tail (Figure 5.5). Therefore, the probability density is given by:

$$P(m) = c_2 \exp\left[-c_1 \sum_{i=1}^{nm} |m_i| \right] \tag{5.20}$$

where c_1 is the decay parameter and c_2 is a normalization constant.

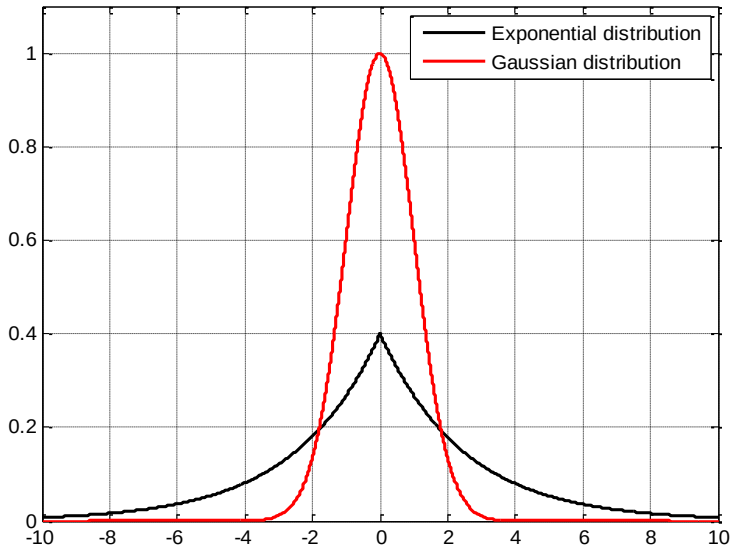

Figure 5.5: Exponential distribution (black curve) and Gaussian distribution (red curve).

Furthermore, assuming noise in the data is uncorrelated and Gaussian distributed with zero mean, the conditional probability density of the data given the prior reflectivity sequence is represented by:

$$P(d \mid m) = c_3 \exp\left[-\frac{1}{2\sigma_n^2} \sum_{k=1}^{n_d} \left(d_k - \sum_j w_j m_{k-j} \right)^2 \right] \tag{5.21}$$

where σ_n is the noise standard deviation and c_3 is a normalization constant.

According to Eq.5.19, the following equation will be true:

$$P(m \mid d) = \frac{1}{P(d)} \cdot P(d \mid m) P(m) \tag{5.22}$$

The event B is typically postulated to remain unchanged in the formula. In this case, the probability of the given observation seismic data d is invariant. Therefore, the posterior distribution $P(m \mid d)$ of the model parameters m is directly proportionate

to $P(d \mid m)P(m)$:

$$
\begin{aligned}
P\left(d \mid m\right)P(m) &= c_3 \exp\left[-\frac{1}{2\sigma_n^2} \sum_{k=1}^{n_d} \left(d_k - \sum_j w_j m_{k-j} \right)^2 \right] \times c_2 \exp\left[-c_1 \sum_{i=1}^{n_m} |m_i| \right] \\
&= c_2 c_3 \exp\left\{ -\left[\frac{1}{2\sigma_n^2} \sum_{k=1}^{n_d} \left(d_k - \sum_j w_j m_{k-j} \right)^2 + c_1 \sum_{i=1}^{n_m} |m_i| \right] \right\} \\
&= c_2 c_3 \exp\left\{ -\left[\sum_k \frac{1}{2} \left(\frac{r_k}{\sigma_n} \right)^2 + \sum_i c_1 |m_i| \right] \right\} \\
&= c_2 c_3 \exp\left\{ -\left[\sum_k \frac{1}{2} \left(\frac{r_k}{\sigma_n} \right)^2 + \sum_i \rho\left(\frac{m_i}{\sigma_m} \right) + n_m \cdot \frac{a^2}{2} \right] \right\} \\
&= c_2 c_3 \exp\left[-\left(J_m + n_m \cdot \frac{a^2}{2} \right) \right]
\end{aligned}
\tag{5.23}
$$

Obviously, to maximize the posterior distribution density of the reflectivity sequence m is just to minimize the modified objective function J_m (Eq.5.14). Consequently, a sparse reflectivity series will be obtained by solving the system of normal equations in Eq.5.18.

5.4.3 Iteratively Reweighting Strategy for Sparse Recovery

An Iteratively Reweighted Least Squares (IRLS) algorithm will be applied to solve Eq. 5.18. It starts with an initial reflectivity series m^0 to generate the initial diagonal matrix Q, in which all diagonal elements are weighted equally. Also, the hyperparameter μ is selected to provide a prior distribution for the sparse recovery. The source autocorrelation matrix R is calculated with an estimated wavelet. Therefore, the solution m^1 at the first iteration can be obtained by left multiplying the g column vector by the inverted well-conditioned kernel matrix. The resulting

reflectivity sequence will be used to calculate a new Q for the next iteration. Accordingly, the diagonal elements are reweighted by the current reflectivity in which larger absolute values will provide less weight and vice versa. This process is repeated until the error between the inverted reflectivity sequences in two consecutive iterations falls below some tolerance criterion. Typically, 15 to 20 iterations would guarantee the convergence of solution. Moreover, the penalty factor selection is critical because unsuitable hyperparameter may produce outputs that are unreasonable.

5.4.4 Penalty Factor Selection

Theoretically, under the assumption of Huber criterion, both the parameter a (Eq. 5.12) and the standard deviation of model parameters σ_m are required to compute the penalty factor μ. The parameter σ_m could be chosen based on the theory of probability and statistics. However, in this thesis, the trade-off factor will be determined in a practical way. Figure 5.6b shows the synthetic seismogram generated by 30Hz Ricker wavelet with a signal-to-noise ratio of 5. The optimal hyperparameter could never be found; however the inversion results can be investigated by scanning a series of varying μ values whereby we can plot the data misfits versus l1-norms of those solutions (Figure 5.7). When μ is relatively large, the l1-norm regularization term in Eq.5.11 would be weighted more than the error term. Consequently, the l1-norm of the solution has to be forced to diminish for minimizing the objective function. Furthermore, a too large μ might make the sparse deconvolution behave like a damped least-squares problem under zero-order quadratic regularization. In this case the error between observations and predicted data is obvious. With the penalty

factor getting smaller, amplitude of observation error drops rapidly until some minimum error has been achieved.

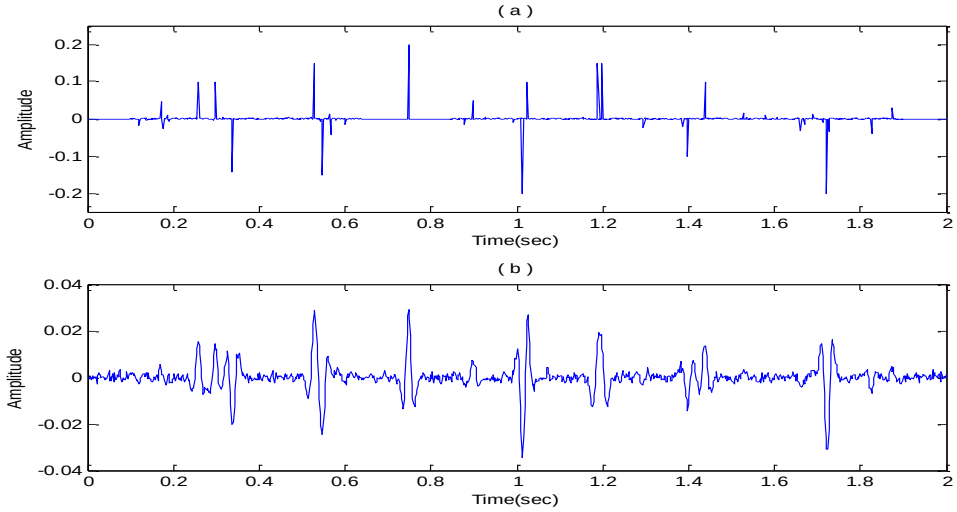

Figure 5.6: (a) Original reflectivity series; (b) Synthetic trace with SNR of 5:1.

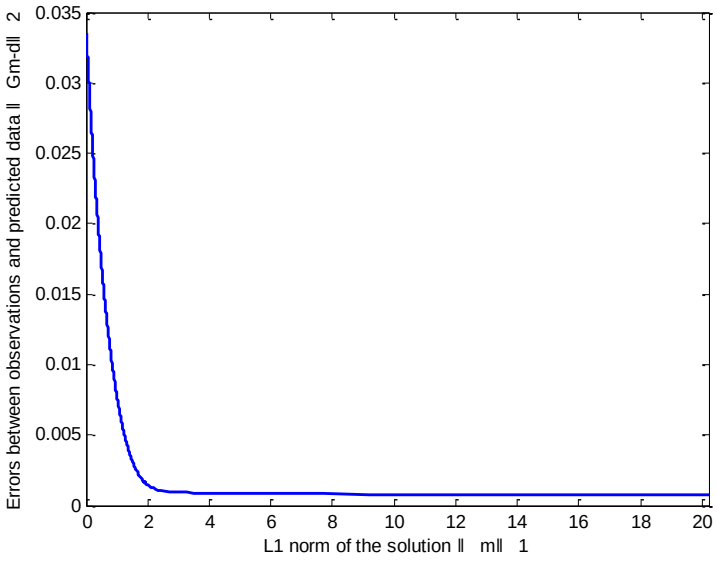

Figure 5.7: Scanning for the optimal regularization factor.

Beyond this point, the curve changes slowly and could actually be considered stable, which implies that increasing the l1-norms of the solutions can no longer reduce the data misfits. Furthermore, as long as μ is small enough, the inverted reflectivity

could be of arbitrary complexity in order to make the error term to vanish. However, since the inverted model structure is desired to be as sparse as possible, we regard the penalty factor at the point where the curve (Figure 5.7) starts to take off as optimal.

A panel displaying different inversion results with varying μ values is given in Figure 5.8. Corresponding to the scanning curve in Figure 5.7, relatively large penalty factors would produce inversion models with higher sparsity while small values lead to denser ones.

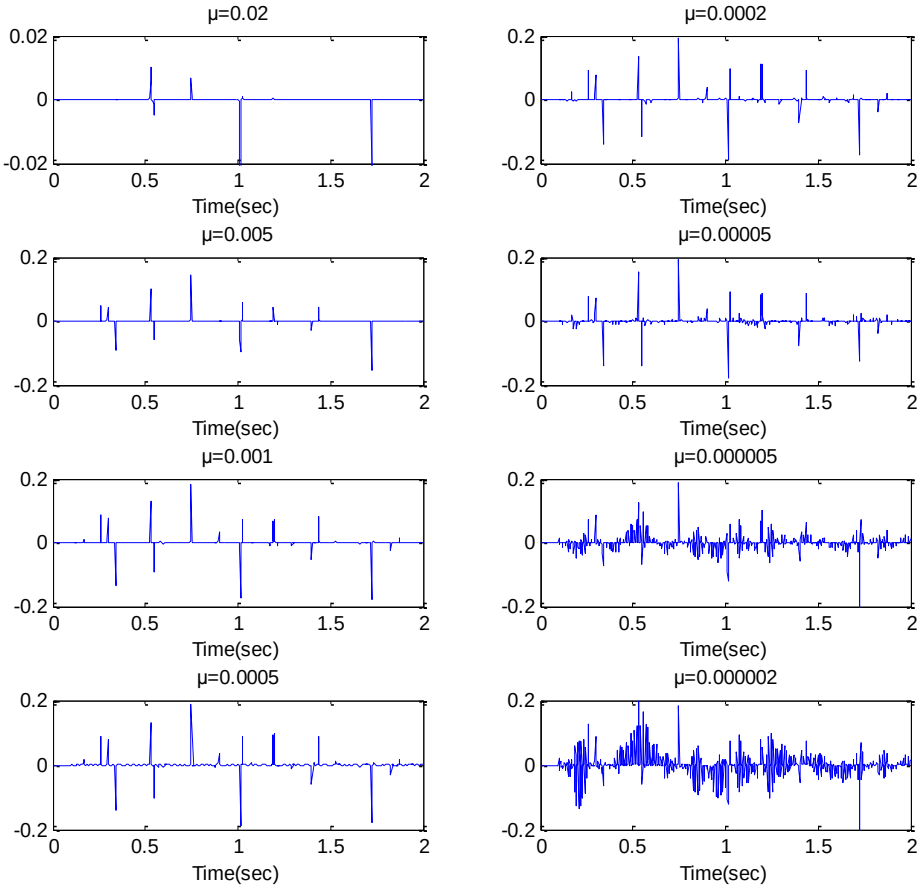

Figure 5.8: Sparse spike deconvolution results with varying penalty factors.

5.5 Synthetic Data Examples

5.5.1 Synthetics with Varying Signal-to-Noise Ratio (SNR)

The synthetic seismogram with varying signal-to-noise ratio (Figure 5.9) is again employed to test the method performance. The corresponding spectra are presented in Figure 5.10. An identical trade-off parameter will be used to invert all four traces. The inverted reflectivity sequence for the clean synthetic is almost the same as the original reference (Figure 5.11a), since the data are exact. When noise level increases, additional spikes may be falsely inverted while some of true reflections might be reduced (Figure 5.11b-d). However, those primary events have been successfully inverted.

As a matter of fact, there is a trade-off between the major reflections and random noise. Sometimes it is necessary to consciously preserve those primary events at the sacrifice of bringing about some noise by selecting a relatively small penalty factor. Fortunately, missing spectral components for each band-limited synthetic are restored very well (Figure 5.12) and the inverted noise has not caused great damage to those inversion results for interpretation.

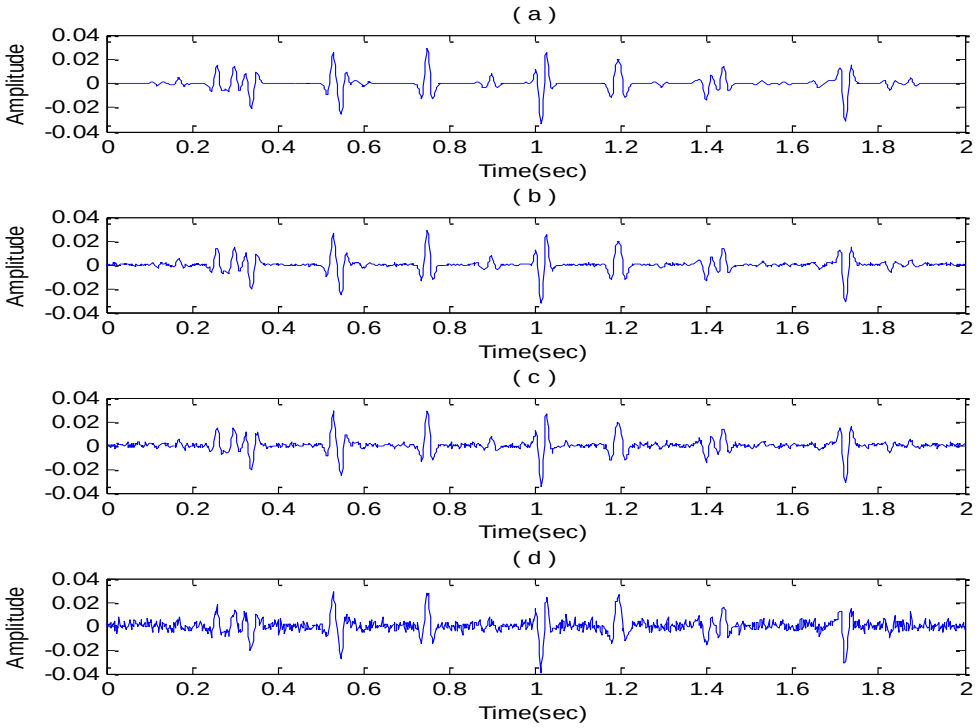

Figure 5.9: Synthetic traces with varying signal-to-noise ratio: (a) no noise; (b) SNR of 10:1; (c) SNR of 5:1; (d) SNR of 2:1.

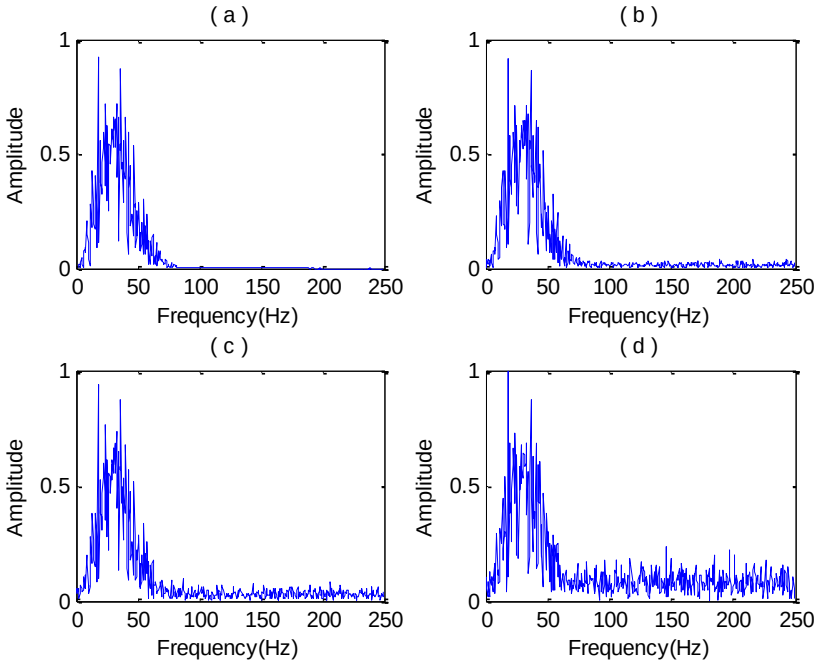

Figure 5.10: Spectra of synthetic traces with varying signal-to-noise ratio: (a) no noise; (b) SNR of 10:1; (c) SNR of 5:1; (d) SNR of 2:1.

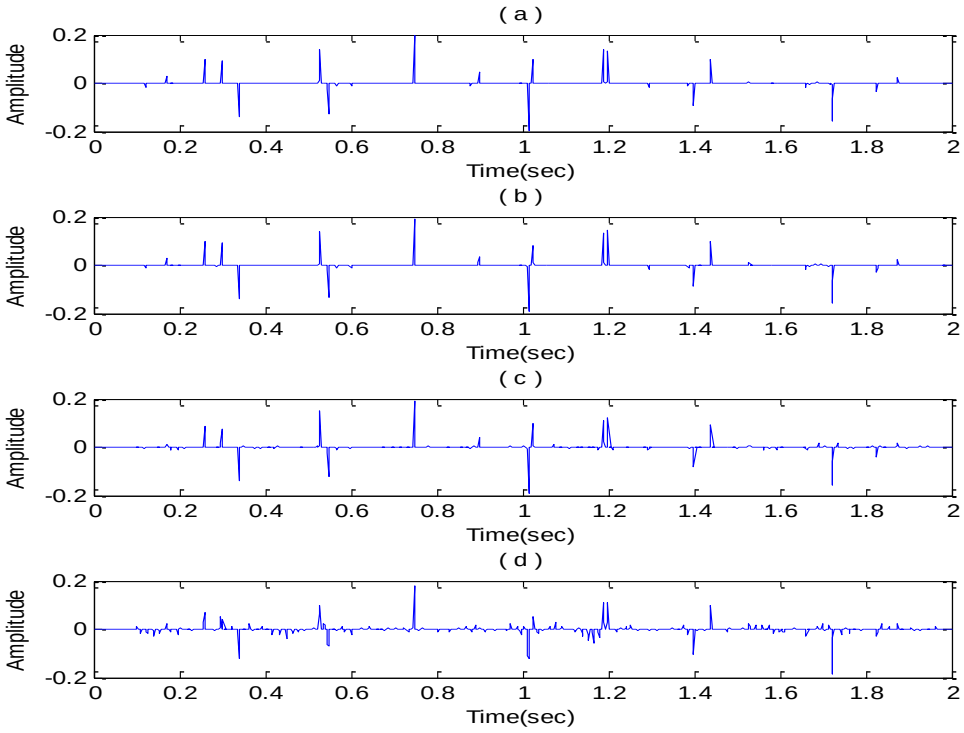

Figure 5.11: Inverted reflectivity for varying signal-to-noise ratio (SSD method): (a) no noise; (b) SNR of 10:1; (c) SNR of 5:1; (d) SNR of 2:1.

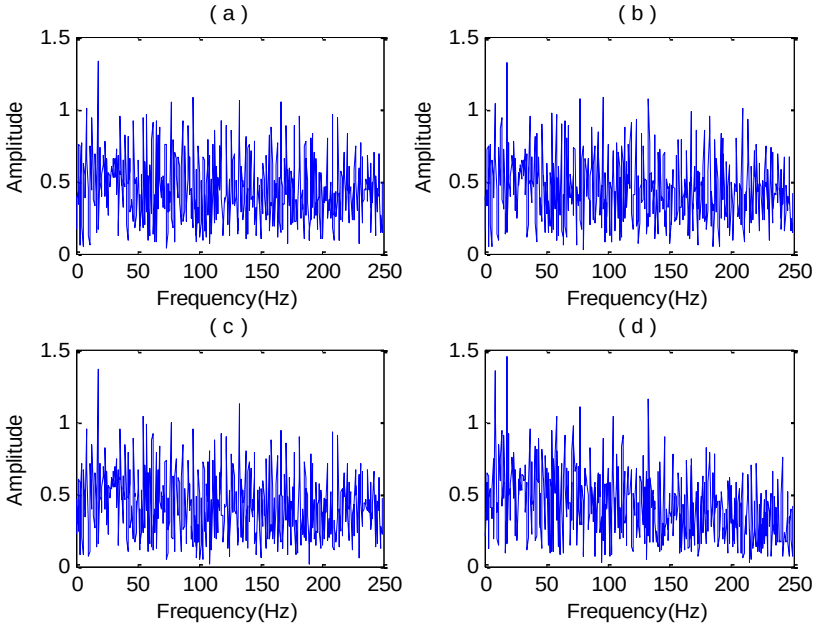

Figure 5.12: Spectra of inverted reflectivity for varying signal-to-noise ratio (SSD method): (a) no noise; (b) SNR of 10:1; (c) SNR of 5:1; (d) SNR of 2:1.

5.5.2 Well Log-derived Synthetics with High Complexity

The inversion result (Figure 5.13c) is acceptable for the well log-derived synthetic seismogram (Figure 5.13b) where the interference effect is extremely serious. Most of the composite events between 0.8s to 1.0s are recovered to be close to the original reference (Figure 5.13a). However, the polarities of events around 0.2s are incorrectly inverted due to the inherent limitation of this method.

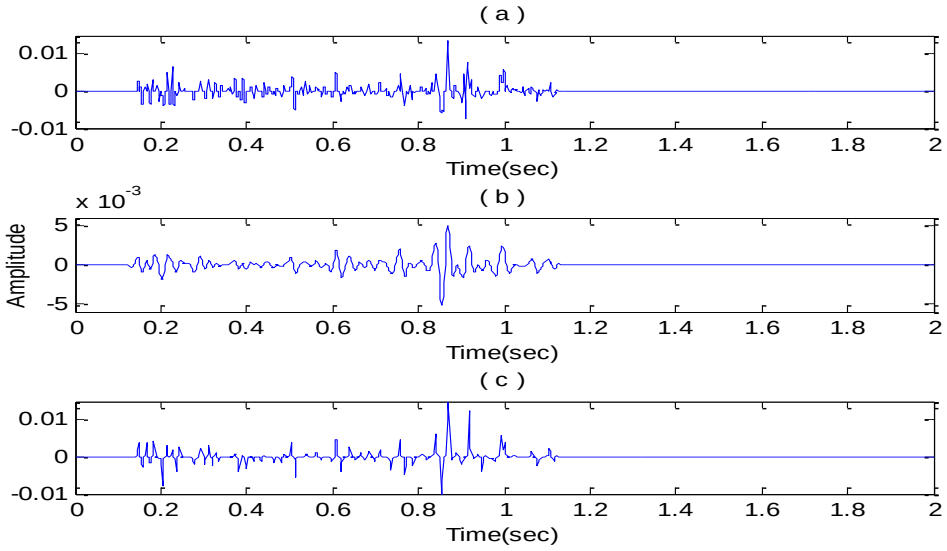

Figure 5.13: (a) Well log-derived reflectivity sequence; (b) Well log-derived synthetic seismogram (30Hz); (c) Inverted reflectivity for the synthetic seismogram (SSD).

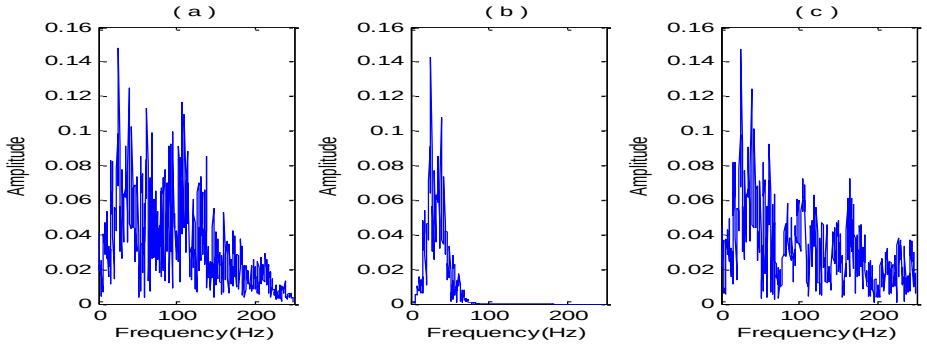

Figure 5.14: SSD method. (a) Spectrum of the well log-derived reflectivity; (b) Spectrum of the well log-derived synthetic seismogram; (c) Spectrum of the inverted reflectivity.

5.5.3 Wedge Model Tests

The wedge models with both even and odd spike pairs are shown in Figure 5.16b and Figure 5.18b. Inspecting the inversion results, inverted spike pairs are satisfactory when the two wavelets are far enough apart. However for the even part (Figure 5.16a), when it comes to the very thin layers, the seismic responses are inverted to be waveforms that are much smoother than the true spikes. For the odd pairs (Figure 5.18a), when the time interval goes below tuning thickness, as the time thickness between peak and trough stays constant and waveform amplitude diminishes, those thin beds can no longer be correctly inverted. Nevertheless, the spectrally extended sections (Figure 5.15b and Figure 5.17b) produced by sparse spike deconvolution both have shown comparable resolving capability to their corresponding high frequency synthetics (Figure 5.15c and Figure 5.17c).

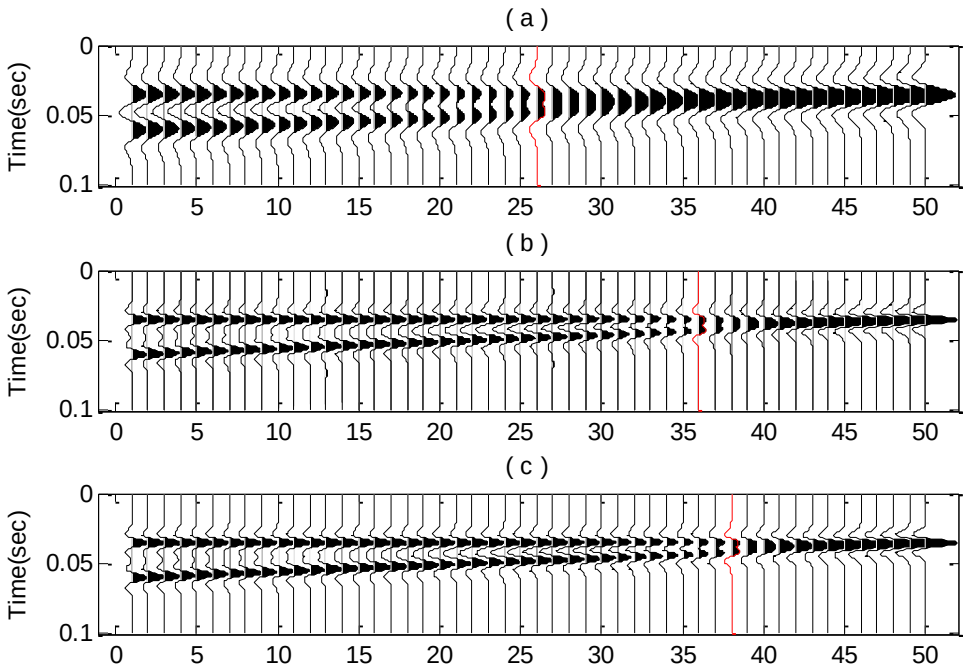

Figure 5.15: SSD method. (a) Seismic responses for even wedge model (30Hz); (b) Spectrally extended responses for the even wedge model (60Hz); (c) Seismic responses for even wedge model (60Hz).

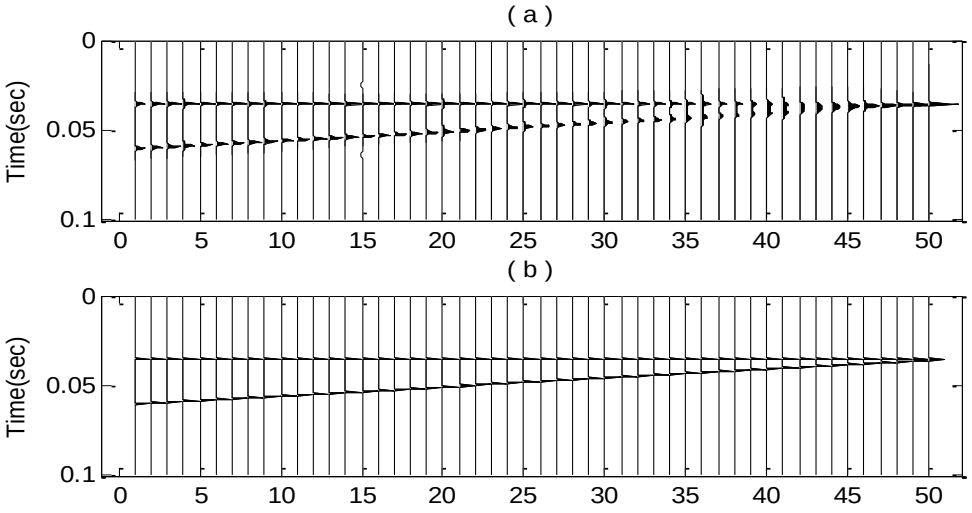

Figure 5.16: SSD method. (a) Inverted even wedge model; (b) True even spike pairs.

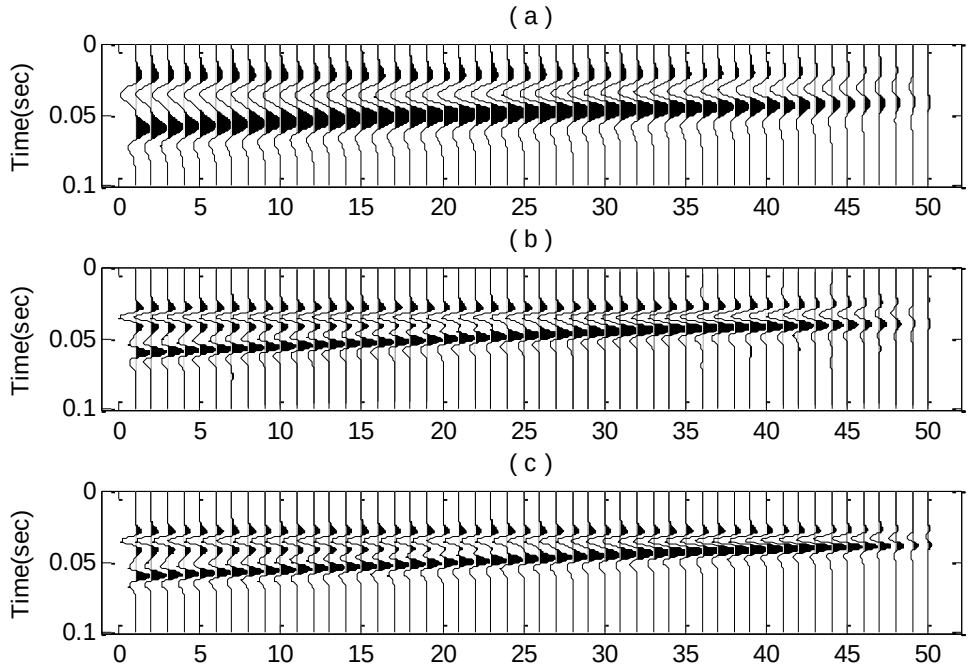

Figure 5.17: SSD method. (a) Seismic responses for odd wedge model (30Hz); (b) Spectrally extended responses for the odd wedge model (60Hz); (c) Seismic responses for odd wedge model (60Hz).

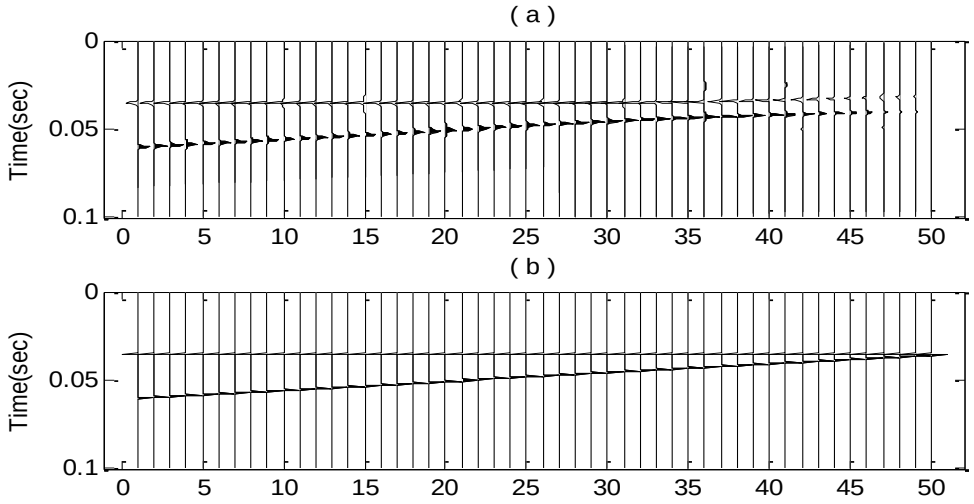

Figure 5.18: SSD method. (a) Inverted odd wedge model; (b) True odd spike pairs.

5.6 Real Data Examples

The same 2D portion of the migrated Blackfoot seismic volume shown in Figure 5.19 is used to test the performance of the reweighted deconvolution procedure when dealing with field data. The corresponding inversion results for inverted spikes (Figure 5.21) and the high resolution section (Figure 5.20) have demonstrated much better resolution than the original section. In particular, we are interested in the coherent events around 0.81s and 1.10s, which may represent two thin layers. They have been clearly resolved using this deconvolution strategy. The regularization parameter used in this real example is determined by examining the trace around that control well; therefore, the same penalty factor will be utilized for all the traces in this target zone. In fact, we can show that different regularizations will give different inversion results; however the one displayed here is reasonable enough.

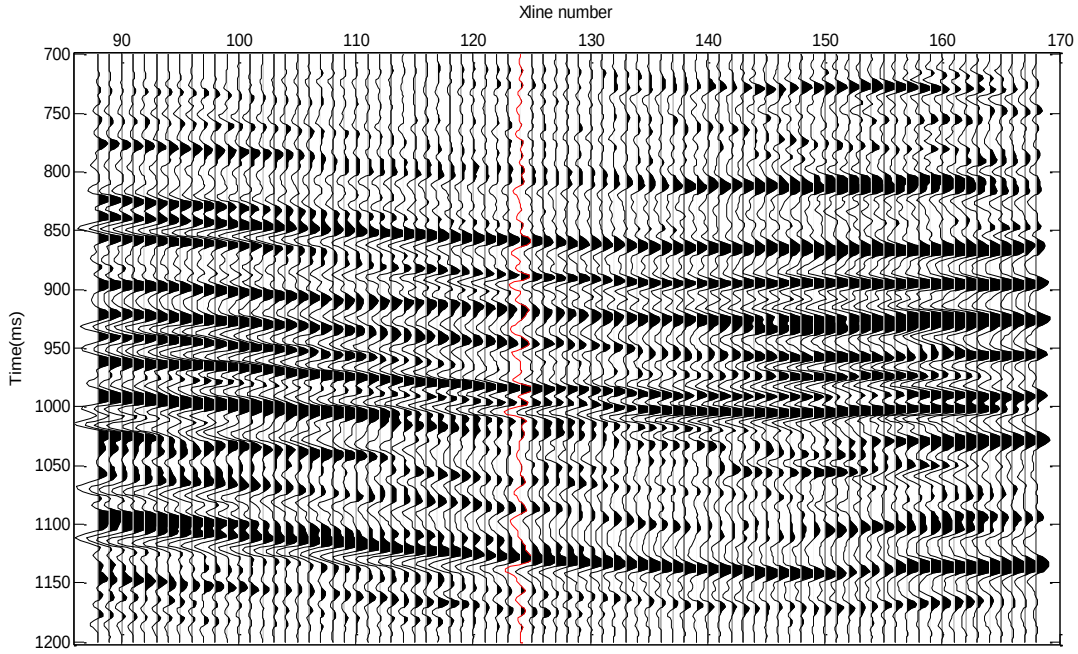

Figure 5.19: Original band-limited seismic section. The well location is near the trace denoted by red color.

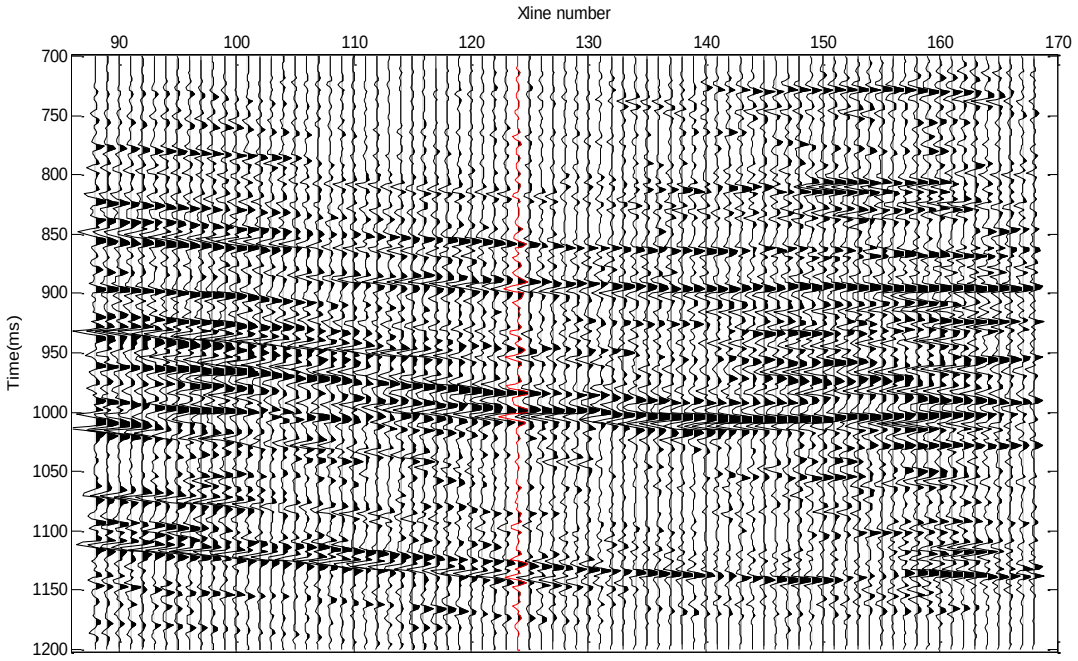

Figure 5.20: Resolution-enhanced seismic section (bandwidth-extended) for SSD method.

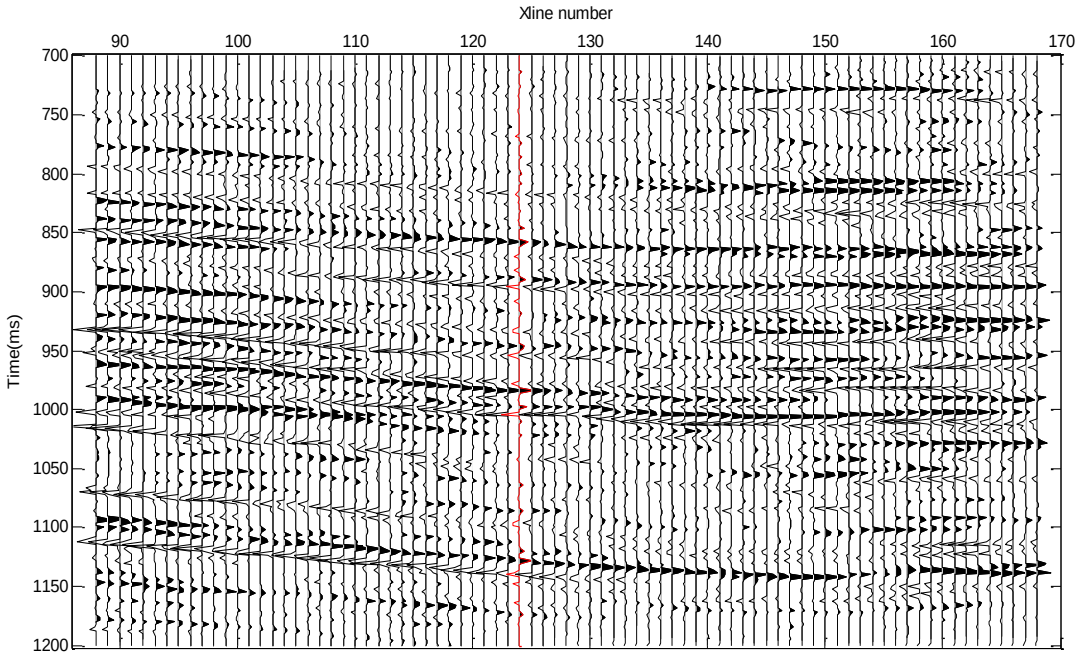

Figure 5.21: Inverted reflectivity section for SSD method.

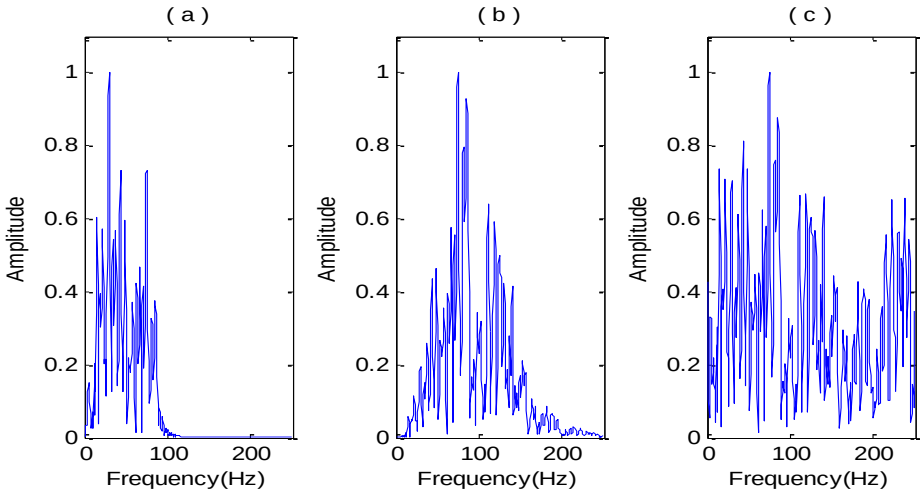

Figure 5.22: SSD method. (a) Spectrum of the original trace at well location; (b) Spectrum of the bandwidth-extended trace at well location; (c) Spectrum of the inverted reflectivity at well location.

5.7 Chapter Conclusion

The sparse spike deconvolution we discuss in this chapter is a conventional method of inverting for high resolution reflectivity in which a reweighted strategy is employed. The regularization term in the objective function derived using Huber's criterion is continuously adapted in order to retrieve the broad-band reflectivity sequence. Incorporating the penalty term with l1-norm of the solution characterizing a prior distribution of long tails constrains those inversion results to be sparse structured.

Selection of the penalty factor is a crucial step in solving for reasonable outputs. It is a trade-off between sacrificing primary events and producing false reflections caused by noise. However, acceptable inverted reflectivity sequences preserving those primary reflections could be obtained by choosing a relatively small penalty factor, even though a certain number of false spikes are generated. This is especially desirable when the seismic data is dominated by a few strong reflections.

As evidenced by the results from the 2D seismic section, this sparse inversion method works pretty well in the real world, and the seismic resolution has been successfully increased.

Chapter 6

Comparison and Discussion

In previous chapters, various methods of extending seismic spectral bandwidth are investigated with both synthetic and real data examples. All of them have been demonstrated to be valid for enhancing seismic resolution. However, realizing the necessity for comparisons between all methods, a comprehensive evaluation will be carried out in this chapter. For convenience, the method introduced in Chapter 3 is labeled as “DFT” because the seismic trace is transformed into frequency domain in a global way. For the method in Section I of Chapter 4, it should be labeled as “MPD” because the signal is spectrally decomposed by matching pursuit algorithm locally instead of globally. In Section II, a continuous wavelet transform is employed to decompose the band-limited signal into discrete sub-bands for analyzing, so this methodology is labeled as “CWT”. The conventional sparse spike deconvolution method discussed in the last chapter is referred to as “SSD”.

The apparent difference between the CWT method and the others is that it could only extend the data spectrum upward or downward within 0.5 to 2 octaves, while the other three methods can extrapolate the missing spectral information from zero frequency all the way to the Nyquist frequency. However, recovering a full spectral band does not necessarily mean resolving everything. Some high frequencies are actually incorrectly restored when interference effect is serious, which has been demonstrated

by those thinning beds in the wedge model tests. Therefore, those final spectrally extended wedge model responses for various methods have been plotted with the same bandwidth for both the even spike pairs (Figure 6.1) and odd spike pairs (Figure 6.3), from which we can make a reasonable comparison.

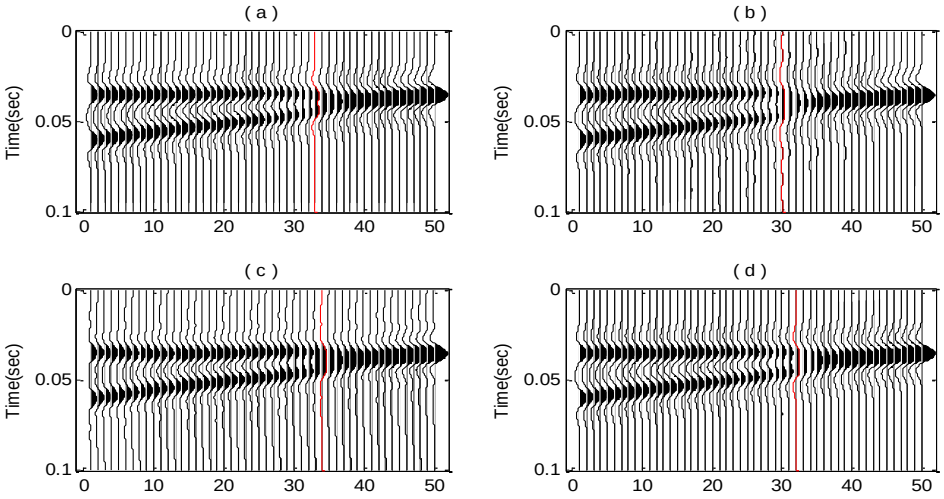

Figure 6.1: Resolution enhanced wedge model responses from even spike pairs. (a) DFT method; (b) MPD method; (c) CWT method; (d) SSD method.

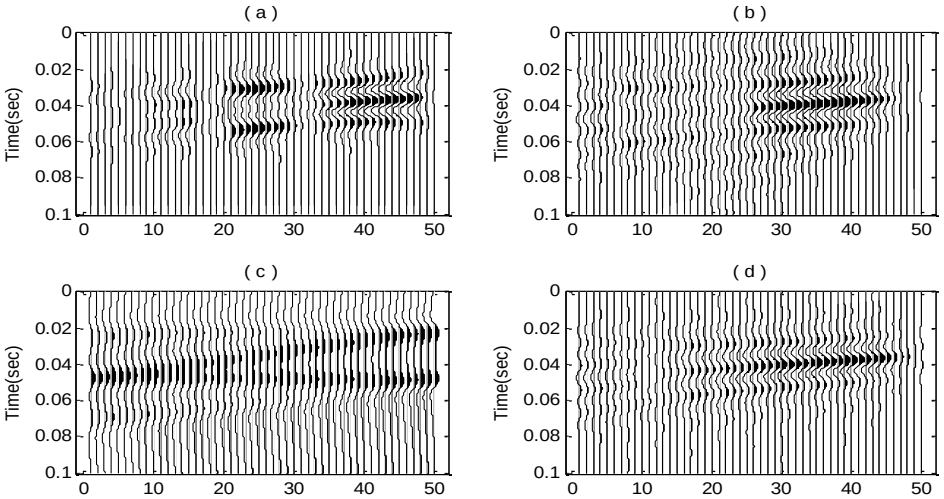

Figure 6.2: Residuals between predictions and high frequency synthetics for the even part. (a) DFT method; (b) MPD method; (c) CWT method; (d) SSD method.

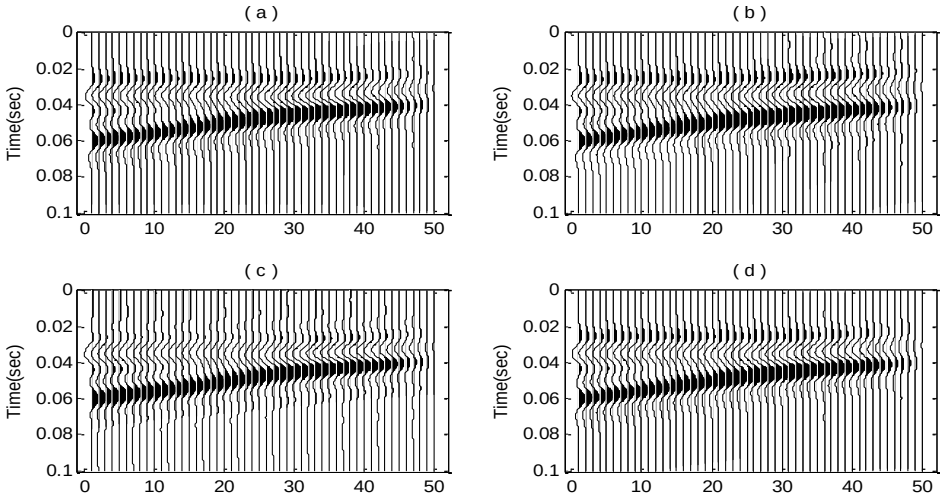

Figure 6.3: Resolution enhanced wedge model responses from odd spike pairs. (a) DFT method; (b) MPD method; (c) CWT method; (d) SSD method.

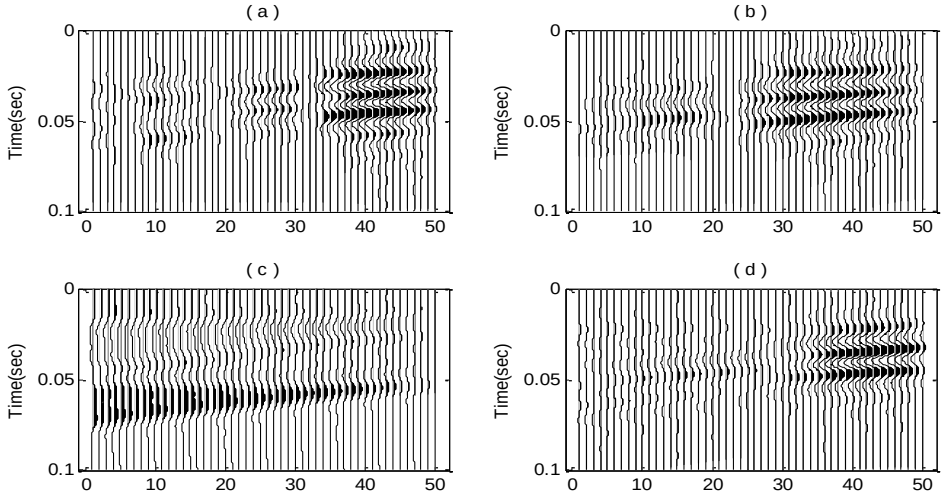

Figure 6.4: Residuals between predictions and high frequency synthetics for the odd part. (a) DFT method; (b) MPD method; (c) CWT method; (d) SSD method.

Although band-pass filtered with the same bandwidth, the four groups of wedge model responses produced by various methods have actually shown somewhat different resolving capabilities. For the even part, DFT method can distinguish the top and bottom reflectors at Trace 33, while MPD method resolves the thin beds down to Trace 30. The CWT method and SSD method resolve thin beds to Trace 34 and Trace

32, respectively. For the odd part, the CWT method produces seismic responses with a smaller tuning thickness than the other three. The MPD method, however, exhibits the largest tuning thickness among them. Furthermore, we also calculate the differences between those resolution-enhanced seismic responses predicted by the various methods and their corresponding true high frequency synthetics. Dividing the Root-mean-square values of the errors by that of the high frequency synthetics, we find the average percentages for these four methods are 3.12% (DFT), 16.54% (MPD), 33.58% (CWT) and 4.54% (SSD), respectively. Note that all the sections have been normalized and the calculations are compared in a relative sense. As observed from reviewing those sections for errors (Figure 6.2 and Figure 6.4), the DFT, MPD, and SSD methods all have shown relatively accurate predictions when the two events are enough apart. When it comes to the thinner part of the wedges, predictions by these three methods may deviate from the truth due to the interference effect. In contrast, the CWT method has shown relative stability for all thicknesses, even where interference becomes significantly serious. The reason why predictions from the MPD method deviate more than those from the others is because it may perform inferior when too much interference occurs. The largest error calculated from the CWT method is caused by the practical wavelet correction inherent in this method, in that its wavelet is no longer Ricker wavelet shaped; its resolution has been actually increased though. So why does the same bandwidth generate results with differing predictions and resolving capabilities? This is because even though the wedge model synthetics are purely clean with exact wavelet, various methodologies extend the original spectra in diverse physical perspectives which lead to those differences.

The DFT method analyzes the whole seismic trace using conventional Fourier transform which provides global spectral information. Errors in the extension partly arise from incorrect cross-correlation coefficients between the sinusoidal bases and the band-limited spectrum due to non-orthogonality. Observed from those inverted spike pairs with very small thickness, those thin beds are gradually considered as single events instead of separated ones, as the layer thickness approaches zero. As long as those primary reflections are dominant in the data, the DFT method could be regarded relatively robust against noise disturbance. Moreover, narrowing the usable data bandwidth may weaken the resolving capability of this method and even bring some detrimental impact in the final results.

The MPD method utilizes matching pursuit algorithm to do spectral decomposition for the seismic data. The atom dictionary used in this part is composed of zero-phase wavelets which are obviously non-orthogonal bases. Compared with the sine waves as atoms over the limited spectral band in the previous method, the issue regarding non-orthogonality becomes more serious for the zero-phase wavelets employed in the MPD method. Reflection interference would directly affect the local decomposition by those correlated wavelet bases. Consequently, narrowing the wavelet bandwidth will also make interfering events increasingly difficult to be resolved. For composite events, some side lobes of the wavelet might be mistakenly regarded as main lobes, due to blindness of the matching pursuit strategy which will definitely distort the true reflectivity. Also, this may be further compounded by random noise. Consequently, the major reflections have to be strong enough so as to be revealed by the program.

A distinct characteristic for CWT method is that multichannel operators are used to compute the missing spectral information. Choosing a suitable operator length is important because multiple spectra series may bring better stability in the extrapolations. As those operators are designed in a least-squares error sense, the predictions should be non-unique, so the calculations on the far ends might deviate from true values. The advantage of this method using multichannel spectra for better stability is simultaneously also a disadvantage, because involving multiple time points may increase the chance of bringing in incorrect values. Furthermore, if there are too many events around a local time point, it will be difficult for the predictive operators to recognize the superposition of so much variations occurring in the spectra. Consequently, the spectral extension is limited in how far out it can reach. However, a positive aspect for this method is that it can manipulate the reflection interference internally and capture the true essence of underlying physical processes, which is the most amazing part for this methodology if it does work.

The SSD method solves for the broad-band reflectivity sequence based on inverse theory, which is achieved by minimizing a regularized objective function. The regularization factor can be adjusted to produce results with varying degree of sparsity. Furthermore, thin beds with very small thicknesses might be inverted to be smoother waveforms than the true spikes, so as to optimize the objective function. This should be the inherent limitation for this method to resolve very thin layers. There is a chance for the SSD method to enhance high frequencies beyond the original bandwidth without amplifying noise. On the other hand, however, some useful information may

also be lost due to the noise suppression.

In accordance with most seismic inverse problems, the accuracy of wavelet estimation plays an important role for all these methods. A biased wavelet for inversion would cause false events or hide true information and even cause the algorithm to totally fail. As observed in Figure 6.1 and Figure 6.3, the CWT method has performed somewhat better than the others, while MPD method has shown the lowest resolving capability. Take note that the wedge model tests in this thesis are carried out by exact data without noise. If robustness of these methods against noise is required to be investigated, this could be accomplished by watching the observation errors between the spectral extension results and the known high frequency synthetics. However, we shouldn't draw any rapid conclusions about which methods will definitely work superior to the others. Even applying the same methodology, it may produce outputs with different degrees of satisfaction in different situations. In fact, any one of these various methods has a chance to surpass the others. Unless the data are exactly accurate, it will be unpredictable as to what is happening in the calculations for noisy data in the real world. Anyway, all the synthetic and real data examples presented in this paper have demonstrated those supposedly valid methods of extending spectral bandwidth are truly effective in seismic resolution enhancement.

For each methodology discussed in this thesis, only one algorithm has been realized to accomplish the target. However, there are many other different ways to achieve the same goal. For instance, in the DFT method, basis pursuit could be used to solve for

those sinusoids coefficients in a global optimization. Even for the matching pursuit algorithm, there will be diverse modified versions to match the signal in better ways, which may be a great topic for future research. As for Chapter 5, more deconvolution techniques may be grouped under the category of sparse spike methods. The reflectivity sequence can also be retrieved based on the principle of maximum likelihood. Moreover, the objective function could be optimized by linear programming in order to produce reflectivity series with sparse structures. Through further studies and efforts, spectral bandwidth extension methods will definitely have a bright future as practical tools for high resolution seismic explorations.

REFERENCES

Arya, V. K., and Aggarwal, J., 1982, Deconvolution of seismic data: Benchmark papers in electrical engineering and computer science: volume 24 Hutchinson Ross Publ. Co.

Backus, G. E., and J. F. Gilbert, 1967, Numerical application of formalism for geophysical inverse problems: Geophysics, J. Roy. Astron. Soc. 13, 247-276.

Barnes, A., 1991, Instantaneous frequency and amplitude at the envelope peak of a constant-phase wavelet: Geophysics, 56, 1058-1060.

Barnes, A. E., 2007, A tutorial on complex seismic trace analysis: Geophysics, 72, no.6, W33-43.

Bergland, G. D., 1969, A guided tour of the fast Fourier transform: IEEE Spectrum, 6, 41-52.

Bosman, C., and Reiter, E., 1993, Seismic data compression using wavelet transforms: 63rd Ann. Internat., Soc. Expl. Geophys., Expanded Abstracts.

Bracewell, R., 1986, The Fourier Transform and its Applications: McGraw-Hill Publ. Co., New York City.

Bradford, J. H., and Y. Wu, 2007, Instantaneous spectral analysis: Time-frequency mapping via wavelet matching with application to contaminated-site characterization by 3d GPR. The Leading Edge, 1018 – 1023.

Campbell, G. A., and R. M. Foster, 1948, Fourier Integrals for Practical Applications: Van Nostrand Company, Princeton, N. J..

Castagna, J. P., 2004, Spectral decomposition and high resolution reflectivity inversion: Presented at the Oklahoma Section Meeting, SEG.

Castagna, J. P., S. J. Sun, 2003, Instantaneous spectral analysis: Detection of low-frequency shadows associated with hydrocarbons: The Leading Edge, 120-127.

Chakraborty, A., D. Okaya, 1995, Frequency-time decomposition of seismic data using wavelet-based methods: Geophysics, 60, no.6, 1906-1916.

Chen, M. Y., 2012, Resolution study on wavelets both in temporal and spectral domain: Master thesis, University of Houston.

Chen, S. S., D. L. Donoho, M. A. Saunders, 2001, Atomic decomposition by basis pursuit: Society for Industrial and Applied Mathematics Review, 43, no.1, 129-159.

Chopra, S., J. P. Castagna, and O. Portniaguine, 2006a, Seismic resolution and thin-bed reflectivity inversion: Canadian Society of Exploration Geophysicists Recorder, 31, 19-25.

Chopra, S. and K. J. Marfurt, 2007, Seismic Attributes for Prospect Identification and Reservoir Characterization: Society of Exploration Geophysicists, Tulsa, O.K..

Chung, H., and D. C. Lawton, 1995, Frequency characteristics of seismic reflections from thin beds: Canadian Journal of Exploration Geophysics, 31, 32-37.

Claerbout, J. F., 1976, Fundamentals of Geophysical Data Processing: McGraw-Hill Inc., New York City.

Cohen, L., 1994, Time-Frequency Analysis: Prentice Hall PTR, New Jersey.

Davies, E. B., and Mercado, E. J., 1968, Multichannel deconvolution filtering of field recorded seismic data: Geophysics, 33, 711-722.

Debeye, H. W. J., and P. van Riel, 1990, LP-norm deconvolution: Geophysical Prospecting, 38, 381-404.

Jenkins, G. M., and D. G. Watts, 1969, Spectral Analysis and Its Applications: Holden-Day, San Francisco.

Kallweit, R. S., and L. C. Wood, 1982, The limits of resolution of zero-phase wavelets: Gephysics, 47, 1035-1046.

Kormylo, J., and J. M. Mendel, 1980, Maximum-likelihood seismic deconvolution: 50th Annual International Meeting, SEG Session: G.77.

Lackoff, M., and LeBlanc, L., 1975, Frequency-domain seismic deconvolution filtering: J. Acoust. Soc. Am., 57, 151-159.

Levinson, N., 1947, The Wiener RMS error criterion in filter design and prediction: J. of Math. Phys., v. 25, p. 261-278.

Levy, S., and Fullagar, P. K., 1981, Reconstruction of a sparse spike train from a portion of its spectrum and application to high resolution deconvolution: Geophysics, 46, 1235-1243.

Lighthill, M. J., 1958, An Introduction to Fourier Analysis and Generalized Functions: Cambridge University Press, Cambridge, England.

Liu, J. L., 2006, Spectral decomposition and its application in mapping stratigraphy and hydrocarbons: Ph.D Dissertation, University of Houston.

Mallat, S., and Z. Zhang, 1993, Matching pursuit with time-frequency dictionaries: IEEE Trans. Signal Prec., 41, 3397-3415.

Menke, W., Geophysical Data Analysis: Discrete Inverse Theory (Revised Edition): International Geophysics Series, 45, Academic Press, 1989.

Nawab, S., and Quatieri, T., 1988, Short-time Fourier transform, in Lim, J., and Oppenheim, A., Eds., Advanced Topics in Signal Processing: Prentice Hall Signal Processing Series, 289-337.

Nguyen, T., and J. Castagna, 2010, High resolution seismic reflectivity inversion: Journal of Seismic Exploration, 19, 303-320.

Nussbaumer, H. J., 1982, Fast Fourier and Convolution Algorithm: Springer - Verlag, Berlin.

O' Brien, M. S., A. N. Sinclair, and S. M. Kramer, 1994, Recovery of a sparse spike time series by L1 norm deconvolution: IEEE Transactions on Signal Processing, 42, no. 12, 3353-3365.

Okaya, D. A., 1995, Spectral properties of the earth's contribution to seismic resolution: Geophysics, 60, 241-251.

Oldenburg, D. W., Levy, S., Whittall, K. P., 1981, Wavelet estimation and deconvolution: Geophysics, 46, 1528-1542.

Oldenburg, D. W., T. Scheuer, and S. Levy, 1983, Recovery of acoustic impedance from reflection seismograms: Geophysics, 48, 1318-1337.

Oppenheim, A. V., and R. W. Schafer, 1989, Discrete-time Signal Processing: Prentice-Hall, Englewood Cliffs, New Jersey.

Peterson, R. A., Fillipone, W. R., and Coker, F. B., 1955, The synthetics of seismograms from well log data: Geophysics, 20, 516-538.

Portniaguine, O., and J. P. Castagna, 2004, Inverse spectral decomposition: 74th Annual International Meeting, SEG, Expanded Abstracts, 1786-1789.

Puryear, C. I. and J. P. Castagna, 2008, Layer-thickness determination and stratigraphic interpretation using spectral inversion: Theory and application: Geophysics, 73, no.2, R37-R48.

Riel, P. V., and A. J. Berkhout, 1985, Resolution in seismic trace inversion by parameter estimation: Geophysics, 50, 1440-1455.

Rioul, O., and Vetterli, M., 1991, Wavelets and signal processing: IEEE Signal Proc. Magazine, no. 11, 14-38.

Robinson, E. A., and S. Treitel, 1964, Principle of digital filtering: Geophysics, 29, 395-404.

Sacchi, M. D., 1997, Reweighting strategies in seismic deconvolution: Geophys. J. Int. 129, 651-656.

Sacchi, M. D. and Ulrych, T. J., 1995, Improving resolution of Radon operators using a model reweighted least squares procedure, J. Seism. Expl., 4, 315-328.

Scheuer, T. E., 1981, The recovery of subsurface reflectivity and impedance structure from reflection seismograms: M.Sc thesis, Univ. British Columbia, Vancouver.

Shanks, J. L., 1967, Recursion filters for digital processing: Geophysics, 32, 33-51.

Smith, M., G. Perry, J. Stein, A. Bertrand and G. Yu, 2008, Extending seismic bandwidth using the continuous wavelet transform: The Leading Edge, 26, 97-102.

Southwood, D. J. and M. G. Kivelson, 1997, Frequency doubling in ultralow frequency wave signals: Geophysics, 102, no.A12, 27.151-27.158.

Strang, G., 1988, Linear Algebra and its Applications (third edition): Thomson Learning, Inc., Belmont, C.A..

Taner, M. T., F. Koehler, and R. E. Sheriff, 1979, Complex seismic trace analysis: Geophysics, 44, no.6, 1041-1063.

Taylor, H. L., S. C. Banks, and J. F. McCoy, 1979, Deconvolution with l1 norm: Geophysics, 44, 39-52.

Tirado, S., 2004, Sand thickness estimation using spectral decomposition: M.S. thesis, University of Oklahoma.

Treitel, S., 1970, Principles of digital multichannel filtering: Geophysics, 35, no. 5, 785 – 811.

Treitel, S., and L. R. Lines, 1982, Linear inverse theory and deconvolution: Geophysics, 47, no. 8, 1153-1159.

Treitel, S., and Robinson, E. A., 1964, The stability of digital filters: IEEE Trans. on Geosci. Electronics, GE-2, 6-18.

Ulrych, T. J., D. R. Velis, and M. D. Sacchi, 1995, Wavelet estimation revisited: The Leading Edge, 14, 1139-1143.

Wang, Y., 2007, Seismic time-frequency spectral decomposition by matching pursuit: Geophysics, 72, no. 1, V13-V20.

Widess, M. B. 1973, How thin is a thin bed: Geophysics, 38(6), 1176-1180.

Yilmaz, Ô. Z., 2001, Seismic Data Analysis: Society of Exploration Geophysicists, Tulsa, O.K..

Zhang, R., 2008, Seismic reflection inversion by basis pursuit: Ph.D dissertation, University of Houston.

Zhang, R., J. P. Castagna, 2011, Seismic sparse-layer reflectivity inversion using basis pursuit decomposition: Geophysics, 76, no.6, R147-R158.